Late Cretaceous-early Paleogene extensional ancestry of the Harcuvar and Buckskin-Rawhide metamorphic core complexes, western Arizona

Martin Sherman Wong[1], John Singleton[2], Nikki M. Seymour[2], Phillip B. Gans[3], and Alexander J. Wrobel[1]

[1]Colgate University
[2]Colorado State University
[3]University of California, Santa Barbara

December 7, 2022

Abstract

Metamorphic core complexes in the western North American Cordillera are commonly interpreted as the result of a single phase of large-magnitude extension during the middle to late Cenozoic. We present evidence that mylonitic shear zones inthe Harcuvar and Buckskin-Rawhide core complexes in west-central Arizona also accommodated an earlier phase of extension during the Late Cretaceous to early Paleocene. Microstructural data indicate substantial top-NE mylonitization occurred at amphibolite-facies, and ^{40}Ar/^{39}Ar thermochronology documents post-tectonic footwall cooling to <500°C by the Paleocene to mid-Eocene. Amphibolite-facies mylonites are spatially associated with voluminous and variably deformed footwall leucogranites that were emplaced from ca. 74-64 Ma, and a late kinematic ca. 63 Ma dike indicates this phase of mylonitization had waned by the early Paleogene. Reconstruction of the footwall architecture indicates that this latest Cretaceous – early Paleocene deformation occurred within a NE-dipping extensional shear zone. The leucogranites were likely the result of crustal melting due to orogenic thickening, implying a model whereby crustal heating triggered gravitational collapse of overthickened crust. Other tectonic processes, such as the Laramide underplating of Orocopia Schist or mantle delamination, may have also contributed to this episode of orogenic extension. Miocene large-magnitude extension was superimposed on this older shear zone and had similar kinematics, suggesting that the location and geometry of Miocene extension was strongly influenced by tectonic inheritance. We speculate that other Cordilleran core complexes also experienced a more complex and polyphase extensional history than previously recognized, but in many cases the evidence may be obscured by later Miocene overprinting.

Late Cretaceous-early Paleogene extensional ancestry of the Harcuvar and Buckskin-Rawhide metamorphic core complexes, western Arizona

Martin S. Wong[1], John S. Singleton[2], Nikki M. Seymour[2*], Phillip B. Gans[3], and Alexander J. Wrobel[1†]

[1]Department of Earth and Environmental Geosciences, Colgate University, 13 Oak Drive, Hamilton, New York, 13346 USA.

[2] Department of Geosciences, Colorado State University, 1482 Campus Delivery, Fort Collins, Colorado 80523, USA.

[3]Department of Earth Science, University of California, Santa Barbara, California, 93105, USA.

Key Points:

- Miocene tectonic exhumation at these core complexes was predated by a latest Cretaceous to early Paleocene extensional event.
- This earlier extension was driven by crustal heating and anatexis that triggered gravitational collapse of overthickened crust.
- Recognition of this earlier extension has important implications for models of core complex formation and western North America.

Corresponding author: Martin S. Wong (mswong@colgate.edu)

*Current address: Department of Geology, Occidental College, 1600 Campus Road, Los Angeles, California, 90041, USA

†Current address: Department of Earth Science, University of California, Santa Barbara, California, 93015 USA

Abstract

Metamorphic core complexes in the western North American Cordillera are commonly interpreted as the result of a single phase of large-magnitude extension during the middle to late Cenozoic. We present evidence that mylonitic shear zones in the Harcuvar and Buckskin-Rawhide core complexes in west-central Arizona also accommodated an earlier phase of extension during the Late Cretaceous to early Paleocene. Microstructural data indicate substantial top-NE mylonitization occurred at amphibolite-facies, and $^{40}Ar/^{39}Ar$ thermochronology documents post-tectonic footwall cooling to <500°C by the Paleocene to mid-Eocene. Amphibolite-facies mylonites are spatially associated with voluminous and variably deformed footwall leucogranites that were emplaced from ca. 74-64 Ma, and a late kinematic ca. 63 Ma dike indicates this phase of mylonitization had waned by the early Paleocene. Reconstruction of the footwall architecture indicates that this latest Cretaceous – early Paleocene deformation occurred within a NE-dipping extensional shear zone. The leucogranites were likely the result of crustal melting due to orogenic thickening, implying a model whereby crustal heating triggered gravitational collapse of overthickened crust. Other tectonic processes, such as the Laramide underplating of Orocopia Schist or mantle delamination, may have also contributed to this episode of orogenic extension. Miocene large-magnitude extension was superimposed on this older shear zone and had similar kinematics, suggesting that the location and geometry of Miocene extension was strongly influenced by tectonic inheritance. We speculate that other Cordilleran core complexes also experienced a more complex and polyphase extensional history than previously recognized, but in many cases the evidence may be obscured by later Miocene overprinting.

1 Introduction

Metamorphic core complexes in the western North American Cordillera represent sites of large-magnitude extension where mylonitic mid-crustal rocks are juxtaposed against brittlely-deformed upper crustal rocks along a gently-dipping normal (detachment) fault. Core complexes are typically interpreted as a fundamentally distinct mode of crustal extension (e.g. Wernicke, 1985; Davis and Reynolds, 1989; Buck, 1991) due to the high magnitudes and rates of slip, the inferred slip of the detachment fault at low angles, and the exhumation of mylonitic mid-crustal rocks, among other factors. Studies of core complexes have provided important insight into key aspects of continental extension such as the initial geometry of detachment faults (e.g., John and Foster, 1993; Wong and Gans, 2008), the magnitude and rate of detachment fault slip (e.g., Foster and John, 1999; Prior et al., 2016), the mechanics of low-angle normal faults (e.g., Axen, 1992; Selverstone et al., 2012), the structural relationship between detachment faults and mylonites (e.g., Lister and Davis, 1989; Singleton and Mosher, 2012), the rheology of the middle crust (e.g. Hacker et al., 1992; Behr and Platt, 2011), and the role of lower crustal flow in extension (e.g., Gans, 1987; Block and Royden, 1990; McKenzie et al., 2000).

Most models for Cordilleran core complexes interpret them as the product of a single phase of middle to late-Cenozoic extension, where footwall mylonites represent the mid-crustal roots of coeval detachment fault systems (e.g., Wernicke, 1981; Davis et al., 1986; Lister and Davis, 1989; Spencer and Reynolds, 1991). Although it is indisputable that many core complexes in the central and southern Basin and Range experienced a phase of mylonitization during mid-Cenozoic exhumation (e.g., Reynolds et al., 1986; Foster and John, 1999; Wells et al., 2000; Wong and Gans, 2008; Singleton and Mosher, 2012; Zuza et al., 2019; Gottardi et al. 2020), some workers have argued that core complex mylonitization locally predates mid-Cenozoic exhumation and instead records Late Cretaceous extension (John and Musaka, 1990; Applegate and Hodges, 1995; Wong and Gans, 2009; Beyene, 2011) or other crustal flow of unknown tectonic significance (Ducea et al., 2020). If significant footwall mylonitization in some core complexes predated mid-Cenozoic extension, this would raise significant questions about the role of ductile deformation in the formation of core complexes, the tectonic significance of this older deformation, and the potential role of reactivation of these older fabrics in controlling the nature and geometry of mid-Cenozoic extensional shear zones and detachment faults. However, overprinting during Cenozoic deformation at many core complexes has often made it difficult to assess the presence and tectonic significance of older footwall mylonitization.

Here we argue that the Harcuvar and Buckskin-Rawhide core complexes in west-central Arizona (Figure 1) record clear evidence of extensive Late Cretaceous to early Paleogene mylonitization that is a distinctly older event than the large-magnitude Miocene extensional event for which Cordilleran core complexes are most well known. Moreover, we believe this early mylonitization records a substantial Late Cretaceous extensional event that immediately post-dated crustal thickening and partial crustal melting. These conclusions are based on

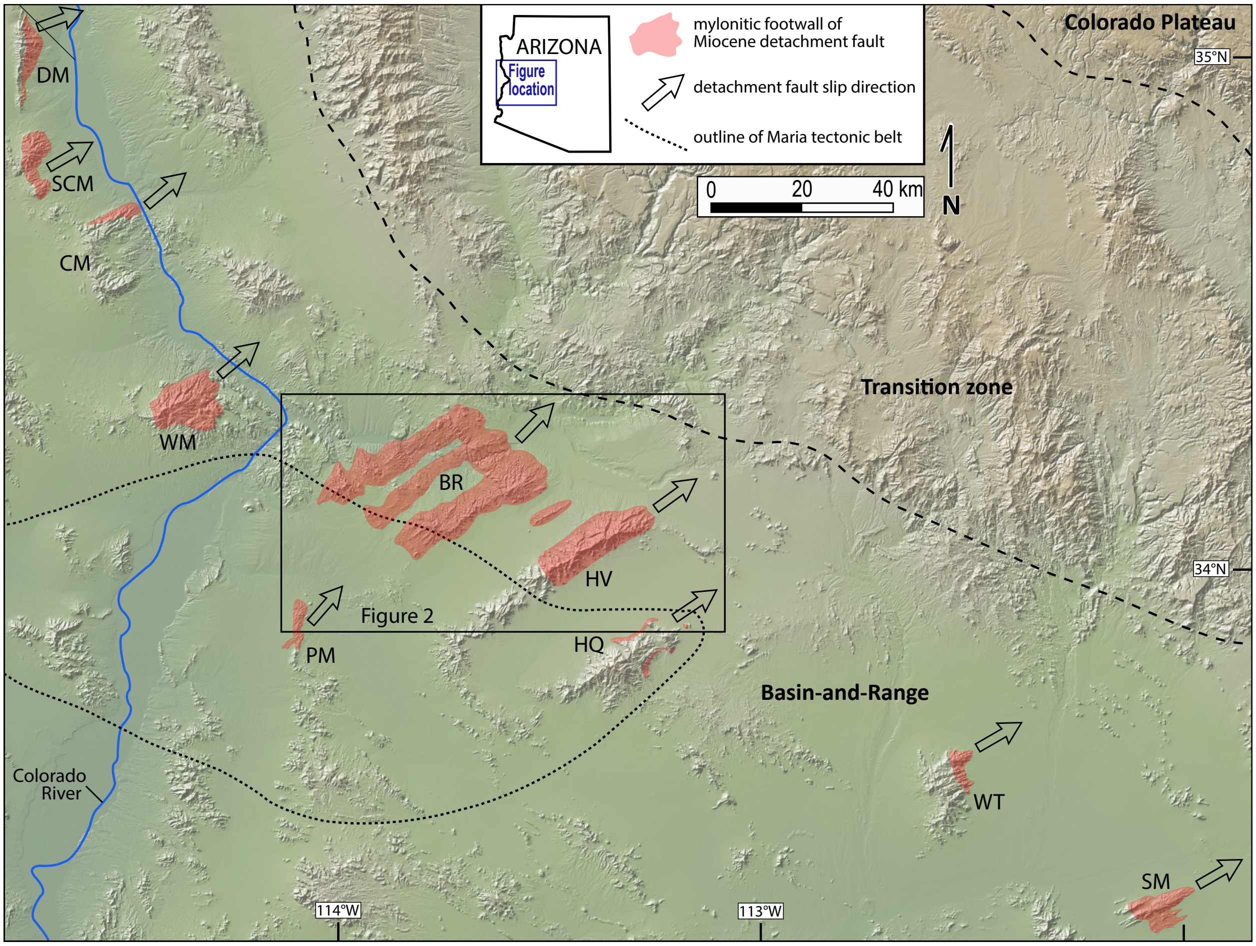

Figure 1. Shaded relief map from Singleton et al. (2018) showing the locations of metamorphic core complexes in southeastern California and western and central Arizona. Mylonitic footwall locations are shown in red and the major detachment fault slip directions are shown by the arrows. The dotted line encompasses the Mesozoic Maria fold-and-thrust belt (after Spencer and Reynolds, 1990). Location names for the mylonite distribution and detachment slip direction: SM—South Mountains, WT—White Tank Mountains, HQ—Harquahala Mountains, HV—Harcuvar Mountains, BR—Buckskin-Rawhide Mountains , PM—Plomosa Mountains, WM—Whipple Mountains, CM—Chemehuevi Mountains, SCM—Sacramento Mountains, DM—Dead Mountains.

geologic mapping, microstructural and electron backscatter diffraction (EBSD) analyses, Ti-in-quartz thermometry, and $^{40}Ar/^{39}Ar$ and U-Pb geochronology. These results demonstrate a composite extensional origin for this belt of core complexes and indicate that single-phase models of core complex formation should be reexamined. Evidence for widespread Late

Cretaceous extension in Cordilleran core complexes also has important implications for understanding the geodynamic evolution of western North America.

2 Geologic background

The Harcuvar and Buckskin-Rawhide Mountains, along with the adjacent Whipple and Harquahala Mountains, form a belt of core complexes within the lower Colorado River extensional corridor (CREC) in eastern California and western Arizona (Figure 2). These core complexes are also located within or adjacent to the Maria fold-and-thrust belt, a zone of Cretaceous basement-involved crustal shortening that was dominantly S- to SW-vergent (e.g., Spencer and Reynolds, 1990). In several ranges across this region (e.g., the Harcuvar, Harquahala, Granite Wash, and Dome Rock Mountains) major Cretaceous thrust faults are cut by Late Cretaceous (ca. 86–70 Ma) granitoids, which in turn are heterogeneously strained (e.g. Rehrig and Reynolds, 1980; Richard, 1988; Laubach et al., 1989; Reynolds and Spencer, 1993; Boettcher et al., 2002). Cawood et al. (2022) interpreted that ductile thrusting in the southernmost part of the Maria fold-and-thrust belt occurred somewhat later at ca. 68–65 Ma. These results place important constraints on the timing of Cretaceous crustal shortening in the region. The total magnitude of crustal shortening across the belt is largely unconstrained, although Chapman et al. (2020) recently applied geochemical proxies to estimate that Late Cretaceous crustal thicknesses may have reached up to 57 ± 12 km in western and southern Arizona. At the end of Cretaceous shortening, accretionary wedge sediments were underplated beneath the Maria fold-and-thrust belt during low-angle subduction of the Farallon plate as the Pelona-Orocopia-Rand Schist (Haxel et al., 2014; Strickland et al. 2018), with schist emplacement occuring by ca. 70 Ma (Jacobson et al., 2017; Seymour et al., 2018).

While most research on the Maria fold-and-thrust belt has focused on contractional structures, growing evidence suggests that Late Cretaceous to early Paleogene NE-directed extension may have also occurred regionally, following the cessation of contraction. Laramide-age mylonitization associated with NE-directed extension has been recognized in several ranges in the CREC and adjacent areas, including the Dome Rock Mountains (Boettcher and Mosher, 1998), Little Maria Mountains (Ballard and Ballard, 1990), Big Maria Mountains (Flansburg et al., 2021), Iron Mountains (Wells et al., 2002), New York Mountains (Wells et al., 2005), and Granite Mountains (Salem, 2009). How widespread this event was and whether it also impacted

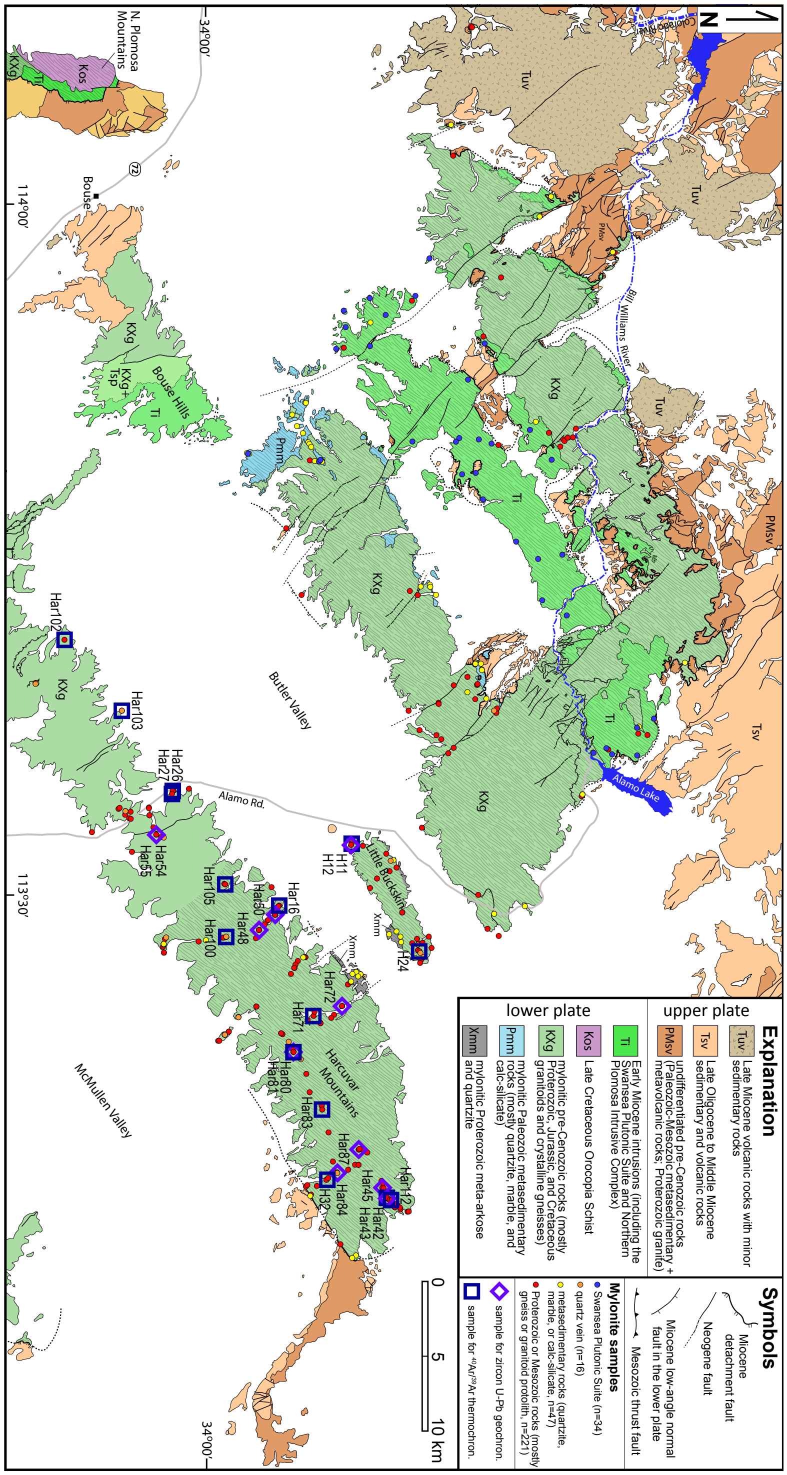

Figure 2. Simplified geologic map of the Buckskin-Rawhide and Harcuvar metamorphic core complexes (after Bryant, 1995; Spencer and Reynolds, 1989). The map also shows the location of samples for petrographic observations (small dots), U-Pb geochronology (diamonds) and $^{40}Ar/^{39}Ar$ thermochronology (squares).

core complexes within the CREC remains unclear, although John (1987) and John and Musaka (1990) suggest that most mylonitization in the footwall of the Chemehuevi detachment fault records top-to-the-NE-directed shearing during the Late Cretaceous (ca. 90–68 Ma).

The Harcuvar and Buckskin-Rawhide Mountains are dominated by variably mylonitized footwall rocks that include Proterozoic and Mesozoic crystalline gneisses, Late Cretaceous granitoids of the Tank Pass Plutonic Suite, Early Miocene granitoids of the Swansea Plutonic Suite, and minor pre-Cenozoic metasedimentary rocks (Bryant, 1995). The footwalls of these two core complexes are bound by one or more regional low-angle detachment faults that experienced tens of kilometers of top NE-directed extensional slip (e.g., Spencer and Reynolds, 1991; Singleton et al., 2014). The total slip across the detachment fault system in the Harcuvar Mountains is estimated to be ~45–50 km based on the correlation of distinct Jurassic clasts in an upper plate megabreccia to their likely footwall source and other lines of evidence (Reynolds and Spencer, 1985; Spencer and Reynolds, 1991; Prior et al., 2016). Extension may have begun in the late Oligocene based on the timing of some basin-fill deposits (e.g. Lucchitta and Suneson, 1993; 1996), but the main phase of detachment fault slip initiated at ca. 21 Ma and continued until ca. 12 Ma (e.g., Carter et al., 2004; Singleton et al., 2014; Prior et al., 2016, 2018).

Footwall fabrics in the Harcuvar and Buckskin-Rawhide Mountains are exposed for up to 35 km in the extension direction (Fig. 2) and are dominated by LS- or L>S-mylonitic tectonites with NE-SW-trending stretching lineations that trend parallel to the detachment fault slip direction. It is clear that significant lower-plate mylonitization occurred during mid-Cenozoic extension based on the presence of mylonitic fabrics in Early Miocene granitoids both locally (Bryant and Wooden, 2008; Singleton and Mosher, 2012) and within nearby core complexes such as the Whipple, Chemehuevi, and northern Plomosa Mountains (e.g., Anderson, 1988; LaForge et al., 2016; Gans and Gentry, 2016; Strickland et al., 2018). The similarity in the geometry and top-to-the-NE kinematics of mylonitic fabrics to the detachment faults further supports models that view these mylonites as the mid-crustal roots of mid-Cenozoic brittle detachment faulting (e.g., Richard et al., 1990; Spencer and Reynolds, 1991; Behr and Platt, 2011; Singleton and Mosher, 2012). This model has often led to the presumption that most or all lower-plate mylonitization of these core complexes is Miocene in age. However, other workers have argued that mylonites with similar fabric geometries and kinematics in the footwall of the Chemehuevi (John, 1987; John and Musaka, 1990), and Riverside (Lyle, 1982) detachment faults are instead Mesozoic in age, which raises the possibility that at least some of the footwall fabrics in the Harcuvar and Buckskin-Rawhide ranges formed prior to mid-Cenozoic extension. Given this uncertainty, assessing the age and significance of footwall fabrics in the Harcuvar and Buckskin-Rawhide ranges is critical to understand the tectonic development of these core complexes.

3 Results

3.1 Footwall fabrics

Footwall rocks in the northeastern ~30–35 km of the Harcuvar and Buckskin-Rawhide Mountains are dominantly well foliated and lineated mylonites (L-S tectonites; Figure 3), although parts of the Early Miocene Swansea Plutonic Suite are characterized by L>S mylonitic fabrics suggestive of constrictional strain (Singleton and Mosher, 2012). Northeast of the mylonitic front, footwall rocks of all ages and lithologies are are variably mylonitic, but locally Late Cretaceous granitoids of the Tank Pass Plutonic Suite are weakly strained, and steeply-dipping gneissic fabrics are exposed beneath metasedimentary mylonites in the southwestern Buckskin Mountains (Singleton et al., 2018). Footwall foliations are generally subhorizontal but dip gently northwest or southeast on the flanks of the ranges, broadly mimicking the corrugations in the bounding detachment fault. These corrugations define fold axes that plunge gently NE or SW, subparallel to the brittle slip direction (Singleton, 2015; Singleton et al., 2019). Lineations in mylonites are typically defined by quartz ribbons, streaks of mica, and/or aligned feldspar porphyroclasts with recrystallized tails. In most areas mylonitic lineations plunge gently NE-SW with a mean trend and plunge of 234°/ 03° in the Harcuvar Mountains, 038°/03° in the Little Buckskin Mountains, 225°/03° in the Ives Peak corrugation in the southern Buckskin Mountains, and 221°/13° in the Clara Peak and Planet Peak corrugations of the Buckskin-Rawhide Mountains (Figure 4).

3.2 Microstructural analysis and deformation conditions

We documented microstructures in >300 oriented petrographic thin sections from across the Buckskin-Rawhide, Little Buckskin, and Harcuvar Mountains (Fig. 2) to evaluate deformation conditions associated with footwall mylonitization (see Supplementary Table S1). Thin sections were cut perpendicular to the mylonitic foliation and parallel to the stretching lineation, and microstructural observations include mineralogy, kinematic indicators, and quartz

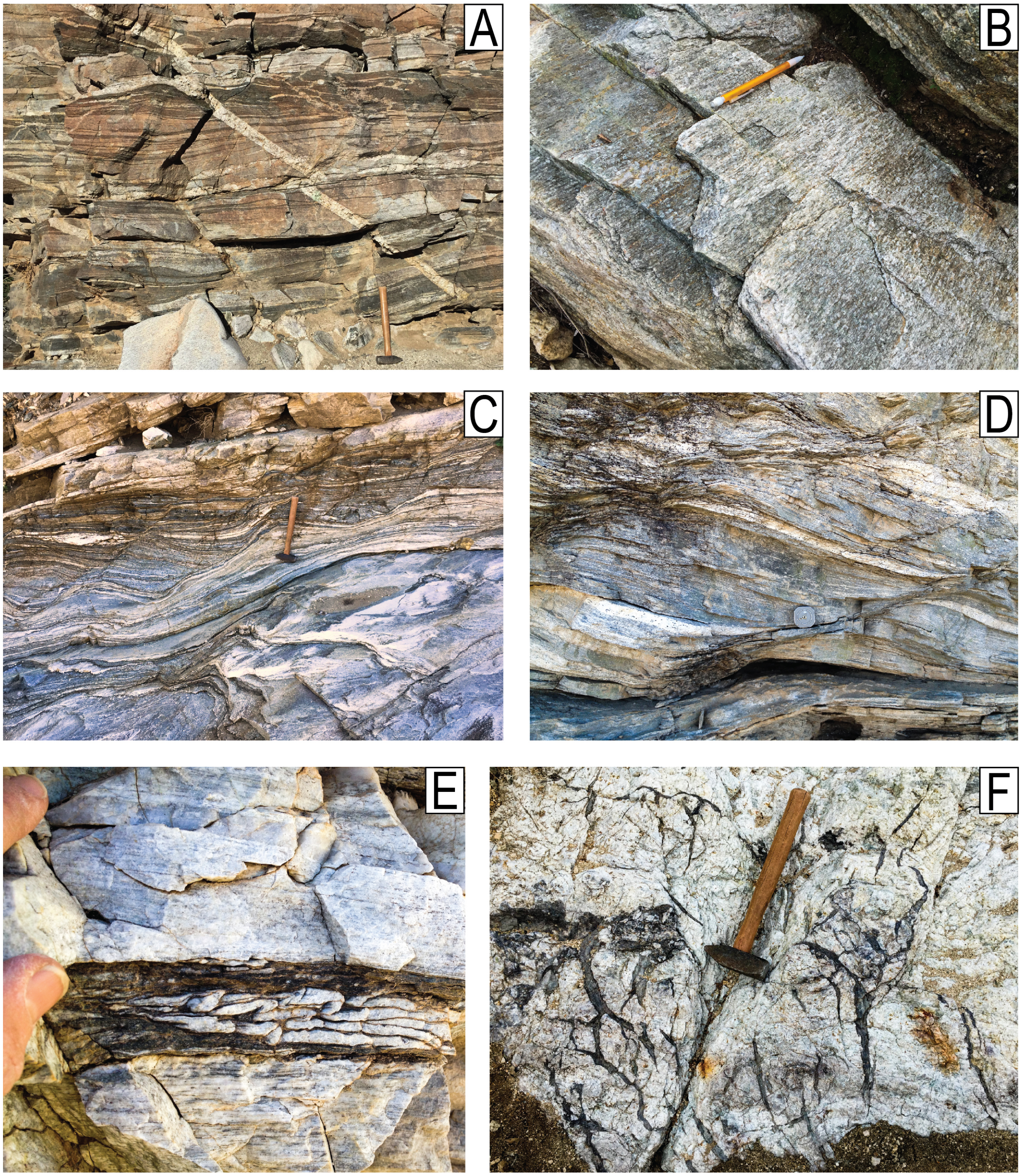

Figure 3. Field photographs from the footwall rocks in the Harcuvar-Buckskin Mountains. A) Gneissic fabric near the mylonitic front east of Cunningham Pass cut by a pegmatite dike, which is displaced by discrete biotite-rich shear zone. B) Leucogranite mylonite along the northwest flank of the Harcuvar Mountains near Burnt Well. Pencil parallels NE-SW trending stretching lineation. C) Top-NE (top-left) shear bands in mylonitic gneiss along the SE flank of the Harcuvar Mountains near Bullard Peak. D) Top-NE (top-left) shear bands in mylonitic gneiss from Miller Wash, eastern Harcuvar Mountains. E) Leucogranite ultramylonite with cm-scale NE-vergent folds (top-right) in the Little Buckskin Mountains. E) Pseudotachylyte (dark material) in leucogranite along a subdetachment fault near Burnt Well in the central Harcuvar Mountains. This fault separates greenschist-facies mylonites in Proterozoic metasedimentary rocks (above) from amphibolite-facies mylonites in Late Cretaceous leucogranite (below).

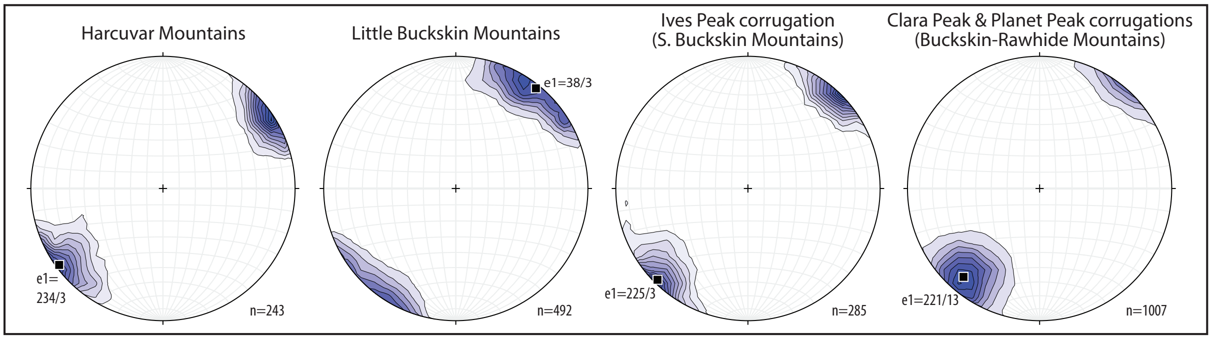

Figure 4. Contoured stereonet plots of mylonitic footwall lineations across different regions within the study area. The shallowly NE-SW plunging lineation direction is highly consistent across the study area.

and feldspar deformation/recrystallization mechanisms. We also estimated dynamically recrystallized quartz grain size for 141 thin sections of pre-Miocene rocks, which we compare to quartz grain sizes of Swansea Plutonic Suite mylonites previously analyzed by Singleton and Mosher (2012). Grain sizes were estimated by tracing ≥50 (average ~86) well-defined recrystallized grains from photomicrographs of relatively pure quartz domains and converting grain areas to an equivalent spherical diameter. For samples with variable grain sizes (typically associated with larger grains produced by grain boundary migration recrystallization) we strived to capture the full range of grain sizes, but mean grain size estimates in these samples have large standard deviations and are used primarily for relative comparison purposes (see Supplementary Figure S1).

Microstructures in footwall mylonites record a wide range of textures and interpreted deformation conditions. In nearly all quartzofeldspathic samples, quartz has undergone dynamic recrystallization and crystal-plastic flow, whereas feldspar records variable degrees of dynamic recrystallization and brittle fracturing. We organized samples into 4 categories based on characteristic quartz and feldspar microstructures that have been correlated with general deformation conditions (e.g., Passchier and Trouw, 2005), with category 1 representing the lowest temperature/highest stress conditions and category 4 representing the highest temperature/lowest stress conditions. Mylonites in all deformation categories are characterized by thinly-spaced foliation, penetrative stretching lineations, and grain-size reduction primarily via dynamic recrystallization.

Category 1 mylonites are characterized by quartz ribbons with incomplete recrystallization and <25 μm recrystallized grain sizes, commonly associated with small

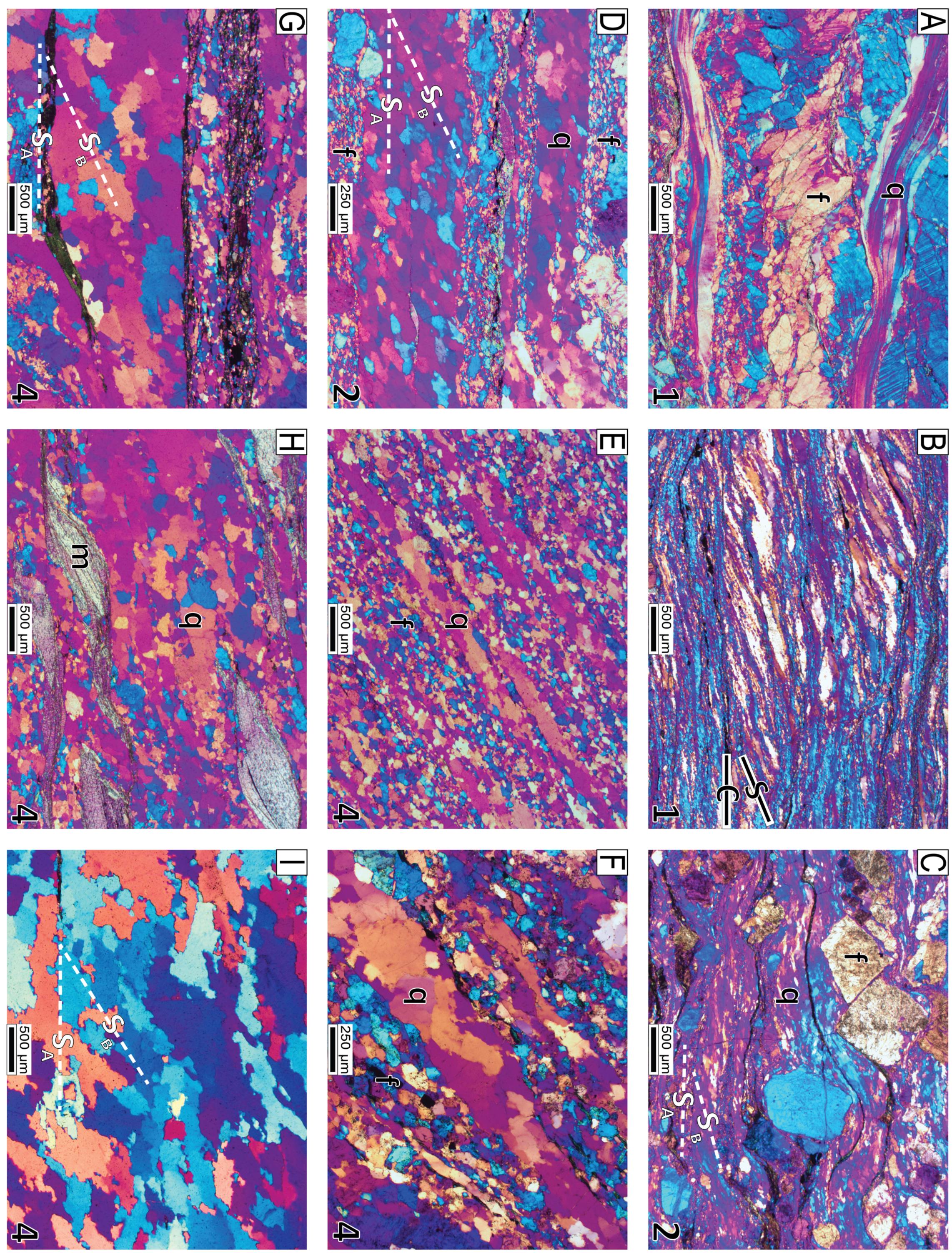

Figure 5. Photomicrographs of mylonites from the Buckskin-Rawhide and Harcuvar metamorphic core complexes. All photomicrographs are from X:Z thins sections in cross polarized light with the gypsum plate inserted, and the northeast side of the macroscopic lineation is on the right. Deformation conditions categories (1-4) are listed in the lower right (see text for details). A) Leucogranite from near the mylonitic front in the central Harcuvar Mountains (H3). Feldspar porphyroclasts (f) record brittle fracturing and cataclasis, whereas quartz ribbons (q) record dislocation creep with very minor BLG. B) Quartzite mylonite from the northwestern flank of the Harcuvar

Mountains near Burnt Well (15-JB3). Quartz records SGR+BLG; S-C fabric records top-NE shear; deformation category 1. C) Swansea Plutonic Suite in the central Buckskin Mountains (5-9). Feldspar (f) records brittle fracturing and minor BLG, whereas quartz records SGR and a grain shape foliation (S_B) that is oblique to the macroscopic foliation (S_A; top-NE shear). D) Leucogranite from the central Buckskin Mountains (4-636); feldspar is deformed by fracturing and BLG (f), whereas quartz is recrystallized primarily via SGR (q) with an oblique grain shape fabric (top-NE shear). E) Leucogranite from the eastern Buckskin Mountains (H20); nearly complete recrystallization of feldspar (f) primarily via SGR and quartz (q) via GBM. F) Leucogranite from the Little Buckskin Mountains (LB-154); feldspar records SGR; quartz records GBM. G) Leucogranite from the Little Buckskin Mountains (LB-190) with quartz GBM and an oblique grain shape fabric (top-NE shear). H) Leucogranite from the Little Buckskin Mountains with quartz GBM (q) and muscovite fish (m; top-NE shear). I) quartz vein from the Little Buckskin Mountains (LB-69); quartz records GBM and a grain shape fabric (S_B) that is oblique to the macroscopic foliation (S_A; top-NE shear).

subgrains and grain boundaries with irregular bulges or sutures (Figure 5), suggesting a combination of subgrain rotation and bulging recrystallization. Feldspar in these samples is dominated by brittle fracturing or cataclasis with minor dynamic recrystallization of <10 μm grains rimming porphyroclasts. Chloritization is common, and fresh biotite is rare. All non-quartzofeldspathic lithologies, predominately calcite-rich metasedimentary mylonites, also fall within this category due to their fine grain size. Category 1 metasedimentary mylonites are common <100 m below the bounding detachment system and were locally sheared through the brittle-plastic transition (Singleton et al., 2018).

In category 2 mylonites, quartz exhibits straight grain boundaries and relatively uniform grain sizes of ~30–70 μm that are similar to subgrains (Fig. 5), suggesting subgrain rotation recrystallization. Dynamic recrystallization of feldspar is more common than in category 1 samples, although porphyroclasts are still typically fractured. Feldspar subgrains and subgrain rotation recrystallization are rare, and overall chloritization is less abundant than in category 1 samples.

Category 4 mylonites are characterized by average quartz grain sizes between 80 and 250 μm with variable size distributions and irregular (amoeboid-like) grain boundaries (Fig. 5), suggesting a dominance of fast grain boundary migration recrystallization. Feldspar in these samples has undergone pervasive dynamic recrystallization into polygonal grains with undulatory extinction and subgrains, suggesting subgrain rotation recrystallization. Feldspar in category 4 granitoid ultramylonites is locally completely recrystallized, and chlorite is rare to absent. Category 3 mylonites have mixed features from category 2 and category 4 mylonites and may either represent an intermediate between these two categories or a lower-temperature overprint of category 4 mylonites.

3.3 Kinematics

The majority of the mylonite samples record a clear microstructural sense of shear. Dynamically recrystallized quartz grain shape fabrics oblique to foliation and C' shear bands are the most abundant shear sense indicators, and S-C fabrics, mica fish, and asymmetric porphyroclasts are also common (Fig. 5). These kinematic indicators consistently indicate a top-NE sense of shear across the study area. Of the 250 oriented thin sections evaluated for shear sense, ~86% record top-NE shear, 13% have symmetric structures or an unclear sense of shear, and 1% record top-SW shear. These microstructural kinematics are consistent with dozens of field observations supporting a dominance of top-NE shear (Fig. 3), which applies to all footwall lithologies and mylonite categories. The clearest top-SW kinematic indicators are from discrete shear zones located near the mylonitic front, which matches observations near the mylonitic front in other Arizona core complexes (e.g., Reynolds and Lister, 1990; Singleton et al., 2019), where antithetic shears have been interpreted to accommodate arching of the footwall during late-stage mylonitization (Reynolds and Lister, 1990).

3.4 Quartz crystallographic preferred orientation analyses

Crystallographic orientation patterns were determined with electron backscatter diffraction (EBSD) at Colgate University using a JEOL JSM6360LV scanning electron microscope with an Oxford Nordlys EBSD detector and processed using the HKL Channel 5 software and the MTEX Matlab toolbox (Bachmann et al., 2010). Step size was variable based on sample grain size but ranged from 5–30 µm. Crystallographic axes in pole figures were reduced to show one point per grain using a misorientation of 10° as a grain boundary threshold.

EBSD analyses of dynamically recrystallized quartz in category 3-4 mylonites reveal a strong CPO with *c*-axis fabrics typically defining a clear Y-axis strain maxima or patterns intermediate between Y-axis maxima and single girdle patterns (Figure 6). These patterns are consistent with inferred deformation temperatures above 500°C (Law, 2014). Based on these patterns, prism <*c*> slip did not play a significant role as a slip system during deformation. *C*-axis and *a*-axis fabric asymmetries, where present, are consistent with the top-NE sense of shear inferred from petrographic observations. Category 1-2 mylonites also have a strongly developed

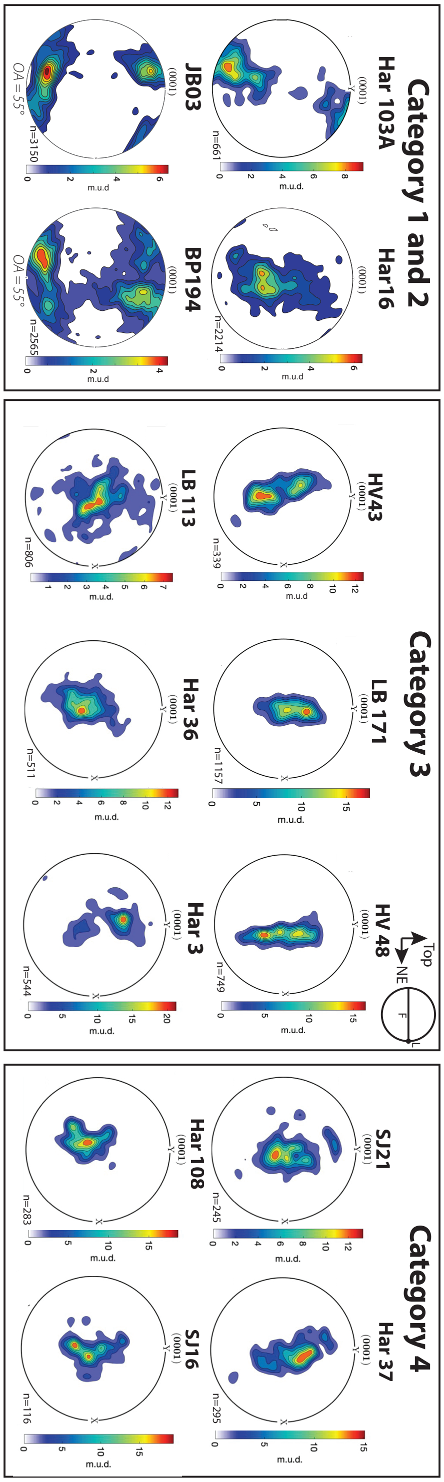

Figure 6. Crystallographic preferred orientation plots of quartz c-axes for representative mylonitic samples within different deformation categories. Sample orientations are shown perpendicular to foliation (F) and parallel to lineation (L) with top as up and NE to the right. Category 1-2 samples typically show cross girdle or single girdle c-axes patterns, while category 3-4 samples have c-axis fabrics typically defining a clear Y-axis strain maxima or patterns intermediate between Y-axis maxima and single girdle patterns. Sense of shear based on pattern asymmetry is top-NE where present.

CPO with distinctive *c*-axes patterns that typically form a cross-girdle or less commonly a single girdle pattern, which is consistent with dynamic recrystallization via BLG and SGR mechanisms at lower temperatures (Stipp et al., 2002b; Faleiros et al., 2010). Two of the category 1-2 mylonites yield *c*-axis cross-girdles with opening angles (OA) of ~55° (Fig. 6), which implies deformation temperatures of 425 ± 50°C (Faleiros et al., 2016).

3.5 Lithologic and spatial patterns of deformation conditions

When viewed across the entire study area, mylonite samples from the Buckskin-Rawhide and Harcuvar core complexes are evenly distributed across the 4 deformation conditions categories, with category 4 samples (~28%) being slightly more common than the other categories (Figure 7). However, the deformation conditions of mylonitization are strongly correlated with lithology. Category 1 samples are dominantly (~80%) metasedimentary mylonites derived from Proterozoic to Paleozoic quartzite and marble, while category 2 samples are typically (~71%) Early Miocene Swansea Plutonic Suite mylonites. The vast majority of category 3 and 4 samples (~85%) are leucogranite mylonites that are derived from Late Cretaceous plutons.

The deformation categories of mylonitization also show strong spatial patterns. Category 1 mylonites are most common in metasedimentary rocks found along the flanks of the footwall corrugations just beneath the detachment fault (Figure 8, Singleton et al., 2018). Some category 1 mylonites are also located near the mylonitic front at the southwestern part of the footwall. Category 2 mylonites are most common in the central part of the Buckskin-Rawhide footwall, where Swansea Plutonic Suite mylonites are prevalent. Category 3 and 4 mylonites are typically located in the interior parts of the Harcuvar, Little Buckskin Mountains, and southern Buckskin Mountains footwall, which also correspond to where Late Cretaceous leucogranite is most common.

To determine how mylonitization conditions vary geometrically and structurally with respect to the detachment fault system, we evaluated structures and samples from several transects that cross the flanks of the footwall corrugations (Figure 9). These transects include the northwest flank of the Ives Peak corrugation near Lincoln Ranch (previously mapped by Singleton et al., 2014), the southeastern flank of the Little Buckskin Mountains corrugation (previously mapped by Singleton, 2011), and the northwest and southeast flanks of the Harcuvar

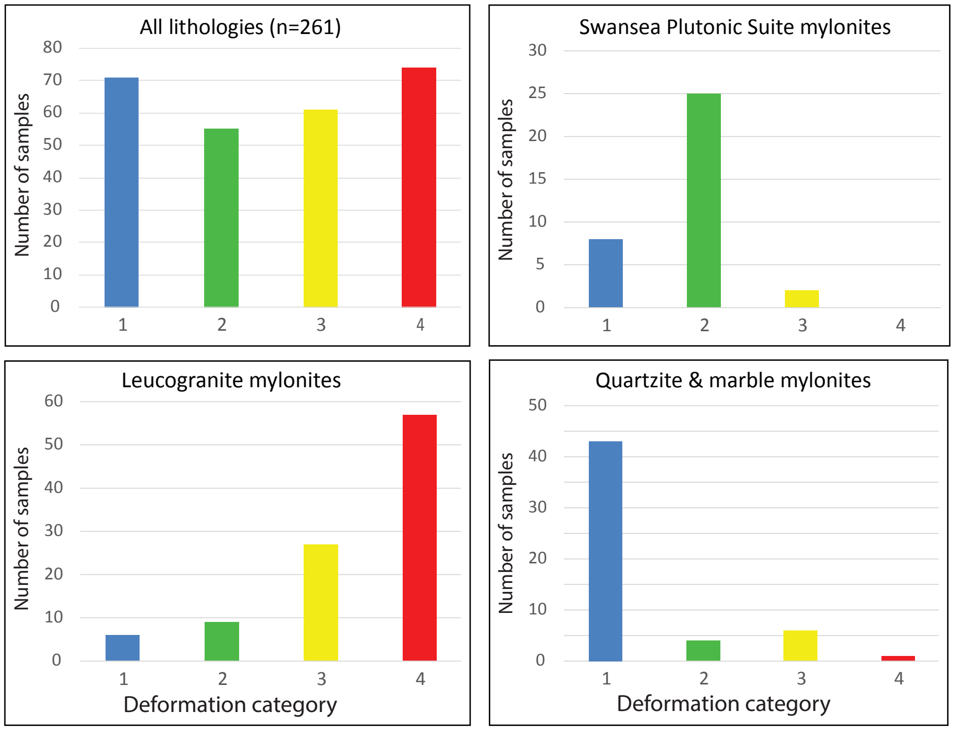

Figure 7. Histograms of the deformation categories (1-4) for mylonites within the study area, organized by lithology. While mylonites within the study area as a whole are equally spread across the deformation categories, there is a strong lithologic influence. Cretaceous leucogranite mylonites dominate the 3-4 deformation categories, Miocene Swansea plutonic suite mylonites are predominantly category 2, and metasedimentary mylonites are predominantly category 1.

Mountains corrugation (new mapping in this study). In each of these areas, category 1 mylonites are present just beneath the detachment system, while category 3-4 mylonites are present several hundred meters below the detachment system.

Along the northwest flank of the Ives Peak corrugation, a 50–100 m-thick section of marble, calc-silicate, and quartzite parallel the gently-NW-dipping detachment fault (Fig. 9). These metasedimentary rocks consistently record top-NE sense of shear and category 1 deformation conditions, and the marble maintains coherent mylonitic fabrics up to ~0.4 m below the Buckskin detachment fault principal slip plane (Singleton et al., 2018). The metasedimentary mylonite zone overlies crystalline mylonites along a sheared contact. The crystalline mylonites consist primarily of orthogneiss with abundant Late Cretaceous leucogranite layers that also record top-NE-directed shear and with category 3-4 deformation characteristics. The contact corresponds to an abrupt change in quartz deformation from bulging and subgrain rotation recrystallization and ~14–25 µm mean grain sizes in the metasedimentary mylonites to grain

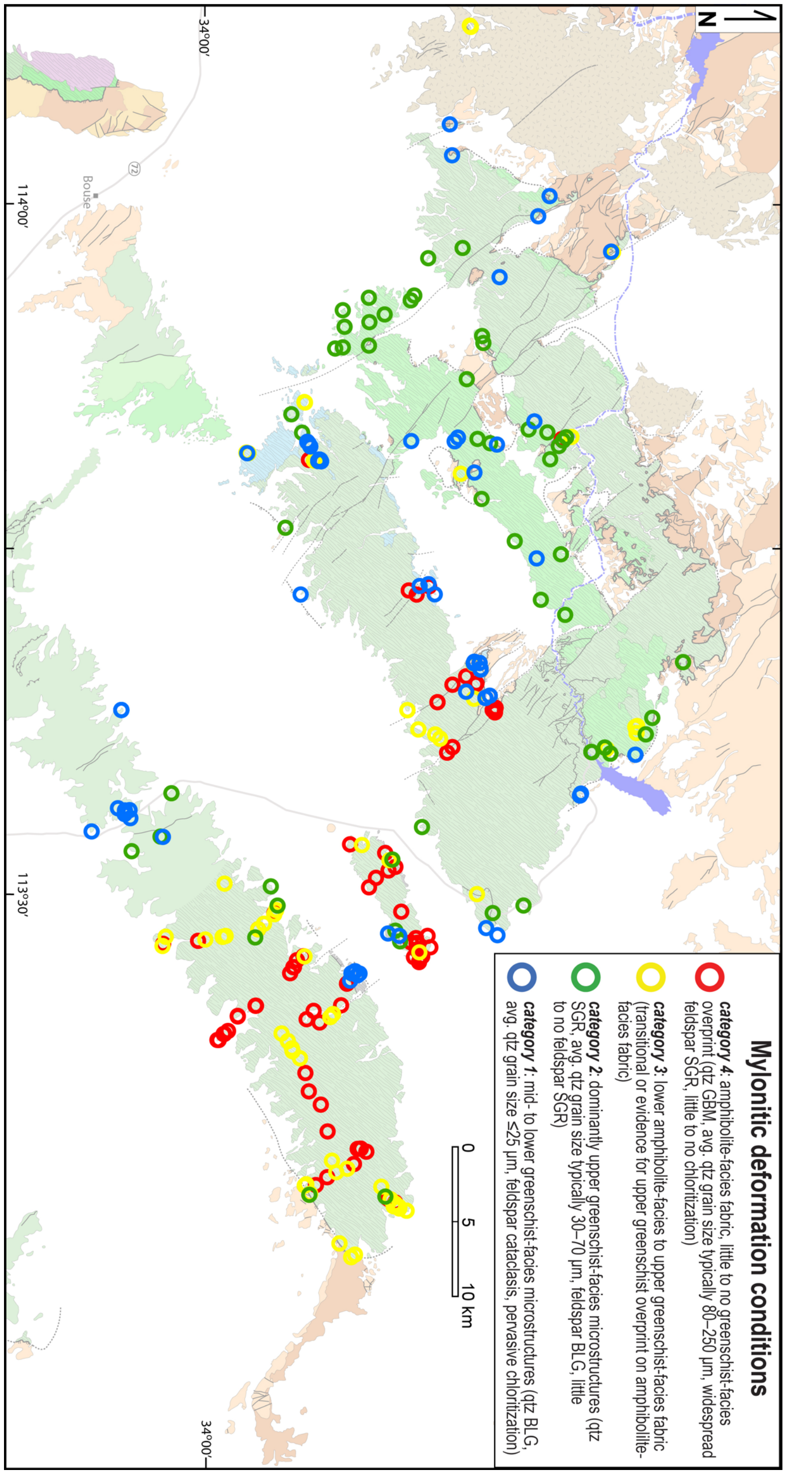

Figure 8. Map showing the spatial distribution of deformation categories across the study area. Category 1 mylonites are most common in metasedimentary rocks found along the flanks of the footwall corrugations just beneath the detachment fault and near the mylonitic front at the southwestern part of the footwall. Category 2 mylonites are common in the central part of the Buckskin-Rawhide footwall, where Swansea Plutonic Suite mylonites are prevalent. Category 3 and 4 mylonites are typically located in the interior parts of the Harcuvar, Little Buckskin Mountains, and southern Buckskin Mountains footwall where Late Cretaceous leucogranite is most common. See Fig. 2 for an explanation of geologic units.

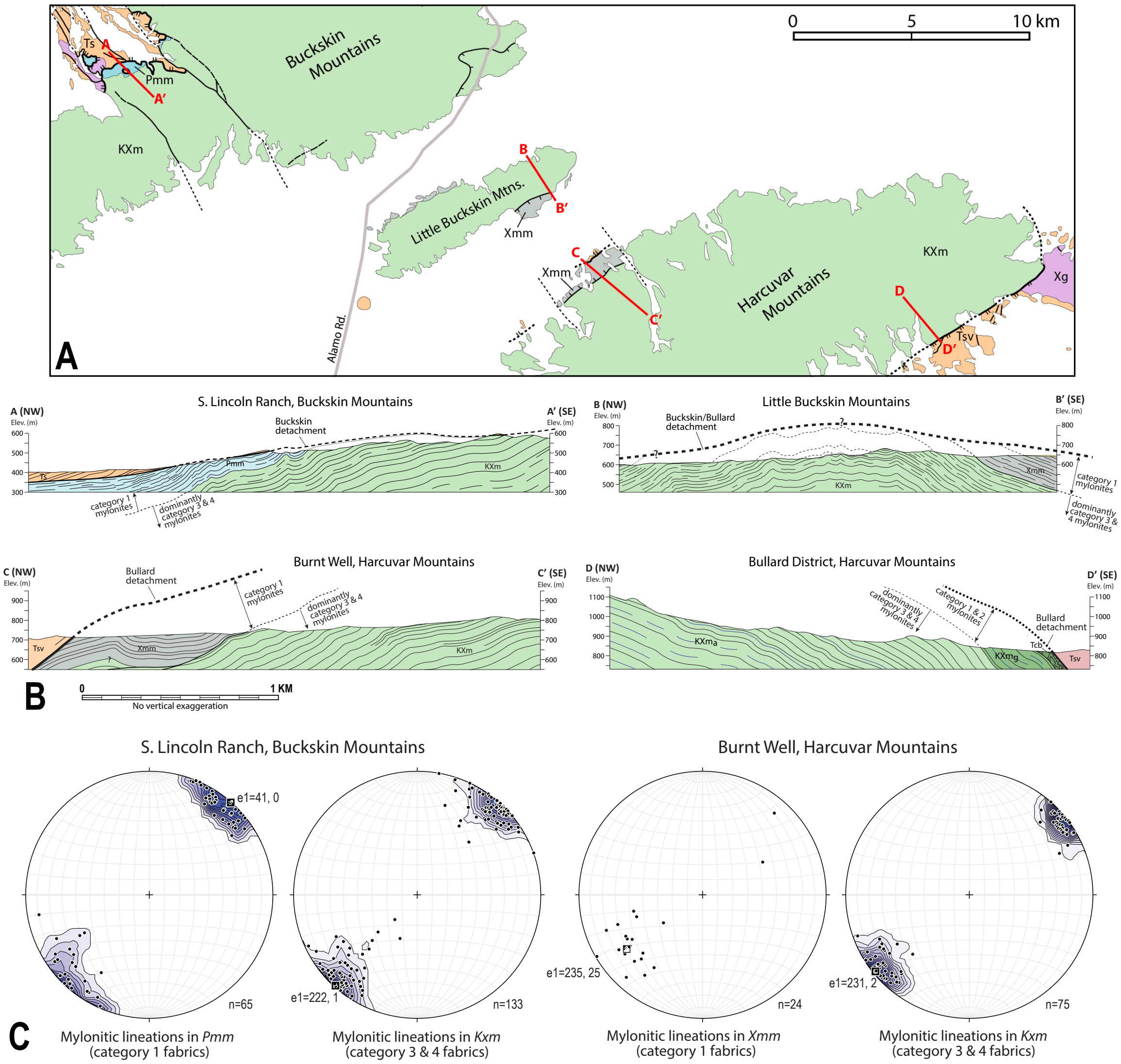

Figure 9. Geologic map (A) and detailed cross sections (B) in the South Lincoln Ranch, Buckskin Mountains (A-A'), Little Buckskin Mountains (B-B'), the Burnt Well locality (C-C') and the Bullard district (D-D') in the Harcuvar Mountains. The cross sections highlight that category 1-2 mylonites are typically located within several hundred meters below the detachment fault and commonly within metasedimentary units. Category 3-4 mylonites are located below this zone and are commonly developed in Cretaceous leucogranites and other crystalline basement rocks. Stereonet plots of lineations (C) highlight that lineation directions are indistinguishable within these different categories of mylonites.

boundary migration and subgrain rotation recrystallization and~60–100 µm mean grain sizes in the crystalline mylonites.

Along the southeast flank of the Little Buckskin Mountains corrugation and northwest flank of the Harcuvar Mountains corrugation near Burnt Well, similar spatial patterns in mylonitization occur (Fig. 9). In these areas, pervasively chloritized mylonites derived from

Mesoproterozoic meta-arkose and quartzite are present at the top of the footwall. These category 1-2 mylonites consistently record top-NE shear subparallel to the slip direction of the bounding detachment fault. This zone of metasedimentary mylonites is up to ~250 m thick and is juxtaposed against crystalline mylonite along a brittle fault that parallels the overlying detachment fault. Along the northwest flank of the Harcuvar Mountains this brittle footwall fault preserves pseudotachylyte veins (Fig. 3), demonstrating that the fault slipped seismically. Crystalline mylonites below this fault are dominantly Late Cretaceous leucogranite that consistently record category 3-4 deformation. Quartz in the metasedimentary mylonites has undergone subgrain rotation and bulging recrystallization with mean grain sizes of 10–50 μm, whereas quartz in the structurally lower leucogranites primarily records grain boundary migration recrystallization and mean grain sizes of 75–300 μm. As with the Ives Peak corrugation, this transition is abrupt and corresponds to the lithologic change from metasedimentary to crystalline lithology. Similar patterns are also observed along the southeast flank of the Harcuvar Mountains corrugation near the Bullard mineral district, where SE-dipping mylonites primarily derived from leucogranite parallel the detachment fault (Fig. 9). Near the top of the lower plate these mylonites are chloritically altered and record quartz subgrain rotation recrystallization with ~30–50 μm mean grain sizes. Chlorite alteration decreases and quartz grain size increases towards deeper structural levels in the footwall, and ≥200–250 m below the detachment fault fabrics are dominated by quartz grain boundary migration recrystallization (mean grain size >100 μm) and feldspar subgrain rotation recrystallization.

Based on these transects, it is clear that category 1-2 mylonites are concentrated within a ≤250 meter-thick carapace at the top of the footwall, whereas category 3-4 mylonites dominate at deeper structural levels. We did not observe a structural base of the category 3-4 mylonites, and based on cross sections, these mylonitic fabrics are likely >1 km thick (Fig. 9). Despite the notable differences in mylonitic deformation conditions preserved in the footwall, fabric orientations within these different zones are remarkably consistent. Where a clear boundary is present between the different category fabrics near Lincoln Ranch and Burnt Well, there is no statistical difference in lineation trend between the different category fabrics (Fig. 9), and a top-NE sense of shear is consistent throughout.

3.6 Ti-in-quartz thermometry

While deformation mechanisms and CPO patterns can provide important constraints on deformation temperatures, these estimates can be influenced by strain rate and other factors (e.g., Law, 2014). TitaniQ thermobarometry, which relies on the temperature-dependent substitution of Ti^{4+} for Si^{4+} in the quartz unit cell, can provide more direct constraints on deformation conditions (Wark and Watson, 2006; Thomas et al., 2010). This approach has been applied to estimate the *P–T* conditions of deformation in quartz-rich rocks (e.g., Kohn and Northrup, 2009; Behr and Platt, 2011; Grujic et al., 2011; Kidder et al., 2013, 2018; Nachlas et al., 2014; Bestmann and Pennacchioni, 2015; Cross et al., 2015), and experiments by Nachlas et al. (2018) demonstrated that dynamic recrystallization of quartz re-equilibrated Ti concentrations to reflect pressure-temperature conditions of deformation.

We conducted Ti-in-qtz thermometry on a subset of samples (n=9) focused on category 4 mylonitic Late Cretaceous leucogranites and quartz veins in order to provide additional constraints on the mylonitization temperatures. We focused on category 4 mylonites because Ti re-equilibration in quartz is mostly likely to occur in mylonites that experienced grain boundary migration recrystallization (Gruijic et al., 2011). Ti concentrations were determined using a Cameca 6f secondary ion mass spectrometer (SIMS) at Arizona State University. Unknowns were calibrated against three Ti-doped synthetic silica glass samples with known Ti concentrations of 0 ppm, 100 ppm, and 500 ppm (Gallagher and Bromiley, 2013). The use of pure silica standards avoids the ~30% bias introduced by calibrating against the common non-matrix matched standards such as the NIST 610, 612, and 614 glasses (Behr et al., 2010). During this analytical session, NIST 612 was analyzed and a NIST soda-lime vs. silica glass standards bias consistent with values reported by Behr et al. (2011) was confirmed. Reported error values only account for uncertainty in the Ti concentration measurements. Individual Ti spot analyses were averaged to calculate a single temperature estimate for each sample. We used the geothermobarometric calibration of Thomas et al. (2010) to convert Ti concentrations into temperatures.

Important unknowns in this calibration are the pressure and TiO_2 activity (a_{TiO2}). The minimum pressure to reach sufficient temperatures to produce extensive mylonitization of quartzofeldspathic rocks, assuming a reasonable 30°C/km geothermal gradient, is 3 kbar. However, the extensive grain boundary migration recrystallization in quartz (Stipp et al., 2002a;

Faleiros et al., 2010) and subgrain rotation recrystallization of feldspar (e.g., Fitz Gerald and Stunitz, 1993 and references therein) recorded by category 4 quartzofeldspathic mylonites require amphibolite-facies conditions (>500°C), suggesting a pressure range of 4–6 kbar is more appropriate for calculations on category 4 samples. This pressure range is reasonable given preliminary thermobarometry from the Harcuvar Mountains, which indicates that Late Cretaceous metamorphism occurred at 6–10 kbar pressures (Walsh et al., 2016), suggesting that the footwall had been deeply buried. We calculate temperatures using a pressure range of 4–6 kbar (Table 1), with calculated temperatures shifting by ~15°C per kbar under these conditions.

The a_{TiO2} can be difficult to estimate, with most studies assuming values of 0.5-1.0, the general range given for most igneous to metapelitic rocks (e.g., Ghent and Stout, 1984). However, Gruijic et al. (2011) demonstrated that these values systematically underestimated the temperatures of quartz deformation in the well–constrained Tonale shear zone and instead suggested a_{TiO2} of 0.2–0.3 is more appropriate for quartz-dominated samples. Furthermore, Thomas and Watson (2012) used melt inclusion compositions of the Bishop Tuff (Wallace et al., 1999) to calculate a_{TiO2} of ~0.23 using the MELTS program and a_{TiO2} of 0.15 using the Rhyolite–MELTS program, suggesting lower values may be more appropriate for felsic samples such as the leucogranite mylonites in our study. The absence of rutile as an oxide mineral in these samples also supports the use of a lower a_{TiO2} value. As such, we used $a_{TiO2} = 0.3$ in these calculations for our granite and quartz vein samples. Assuming a higher Ti activity of 0.7 would lower calculated temperatures by ~60°C.

For all analyzed category 3 and 4 samples, average Ti concentrations range from 0.5 – 13.5 ppm (mean = 6.7 ppm, Table 1) with a corresponding calculated temperature range of 377–588°C (mean = 512°C) at 6 kbar or 345–546°C (mean =474°C) at 4 kbar (Figure 10). Notably, 7 of the 8 samples in these categories yielded calculated temperatures of >500°C within error at 6 kbar, with one anomalously low temperature of 377 ± 13°C (from a quartz vein sample). The range of calculated temperatures for category 3 and 4 samples did not appear to be controlled by lithology. Although one quartz vein yielded the lowest calculated temperature, two other quartz veins yielded relatively high temperatures. All of the category 4 granitic samples yielded temperatures >500°C within error at 6 kbar. The single category 2 granite sample yielded an average Ti concentration of 5.9 ± 1.9 ppm with a calculated temperature of 520 ± 20°C at 6 kbar (482 ± 10°C at 4 kbar), similar to the category 3 and 4 mylonite samples.

Table 1. Ti-In-Quartz Analyses

Sample name	Description	Deformation category	# of analyzed spots	Average Ti (ppm) ± 1σ	Calculated temp. (°C) at 4 kbar*	Calculated temp. (°C) at 6 kbar*
JSH-36	Granitoid	2	7	5.9 ± 1.9	482 ± 10	520 ± 20
HV-48	Quartz vein	3	8	0.5 ± 0.2	345 ± 12	377 ± 13
HV-69	Granitoid	4	9	13.5 ± 2.3	546 ± 12	588 ± 13
15-JB-96	Granitoid	4	7	10.1 ± 1.4	523 ± 10	564 ± 11
LB-12X	Granitoid	4	7	6.6 ± 0.9	491 ± 9	531 ± 10
LB-197	Granitoid	4	7	2.6 ± 2.5	411 ± 56	447 ± 59
HAR38	Granitoid	4	6	4.8 ± 2.3	463 ± 35	501 ± 36
HV-34	Quartz vein	4	7	9.5 ± 0.4	518 ± 3	559 ± 4
EM-2-27	Quartz vein	4	7	5.9 ± 0.2	484 ± 3	522 ± 3

*Calculated temperatures assume $a_{TiO2} = 0.3$

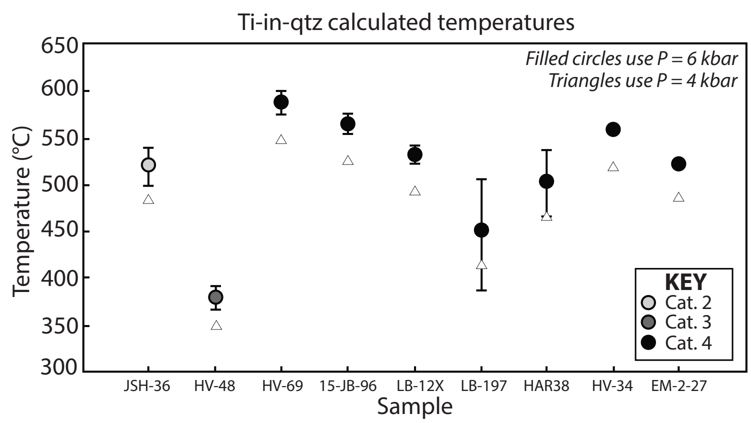

Figure 10. Calculated Ti-in-qtz temperatures for analyzed mylonites organized by deformation category. Filled circles assume pressure = 6 kbar and triangles = 4 kbar ($a_{TiO2} = 0.3$ in both cases). These results show that a significant majority of the samples yield calculated temperatures >500°C within error at 6 kbar pressure and >475°C at 4 kbar. Where no error bars are visible, the error is smaller than the symbol size.

3.7 $^{40}Ar/^{39}Ar$ thermochronology

The microstructural, EBSD, and Ti-in-quartz results all suggest that significant portions of the Buckskin-Rawhide and Harcuvar core complexes footwall underwent mylonitization at relatively high temperatures (amphibolite grade). This raises the question of whether the high temperature mylonitization was part of Miocene extension or a distinctly earlier event. We conducted new $^{40}Ar/^{39}Ar$ analyses on hornblende and biotite (Figure 11) from across the study area to provide new insights into the high temperature thermal history of the footwall and constrain the timing of the high temperature mylonitization. $^{40}Ar/^{39}Ar$ analyses were conducted

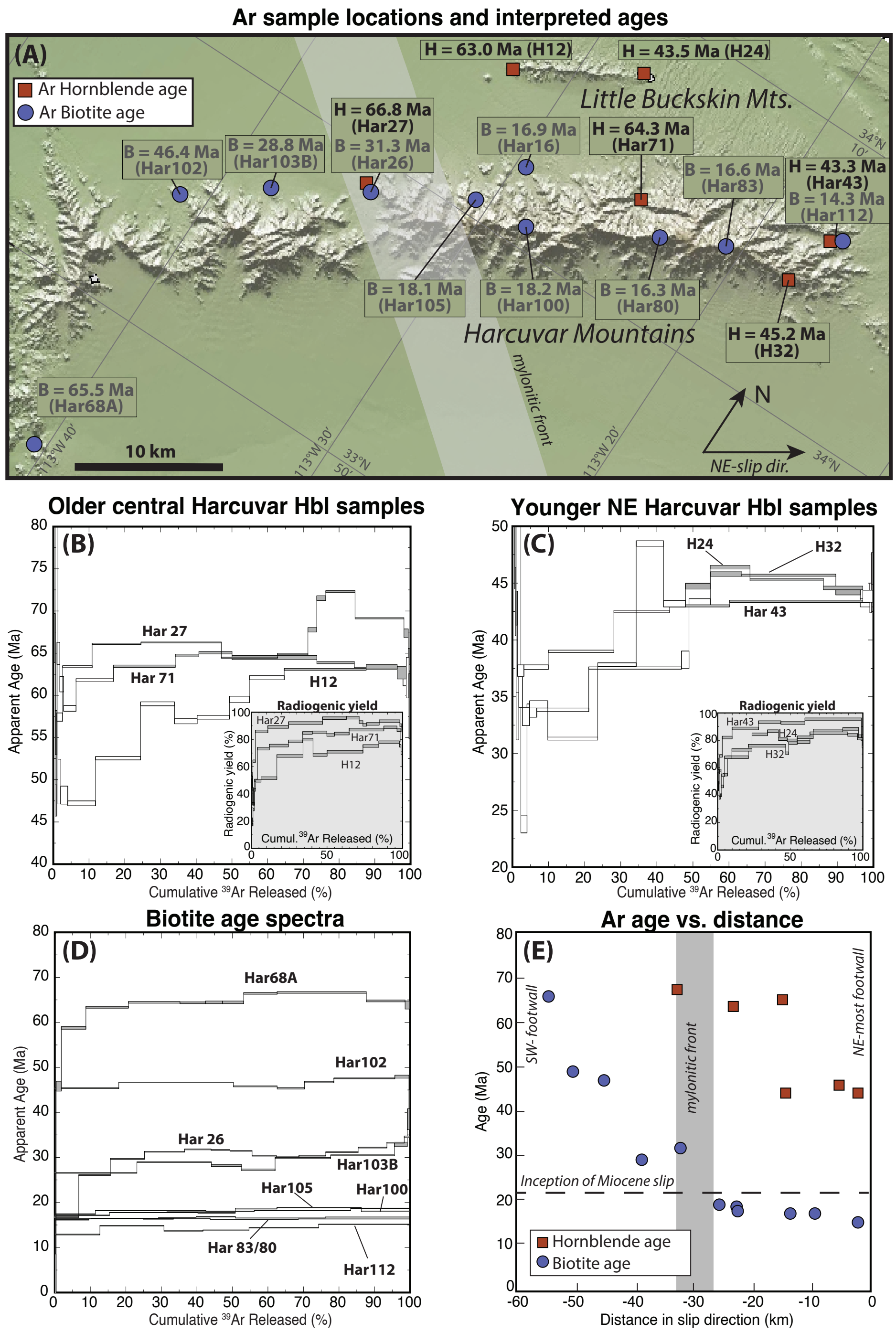

Figure 11. (A) Map of $^{40}Ar/^{39}Ar$ analyses and preferred ages of hornblende and biotite samples from the Harcuvar and Little Buckskin Mountains. (B) $^{40}Ar/^{39}Ar$ age spectra and radiogenic yields for older hornblende samples from the central footwall. Most age spectra show a climbing pattern with a flatter segment at moderate to high temperature steps. See text for additional details. (C) Age spectra for the younger hornblende samples from the northeastern footwall. These spectra also show a climbing pattern but flatten for the last half of the analyzed gas at high temperature steps. (D) $^{40}Ar/^{39}Ar$ age spectra for biotite samples from across the footwall. These spectra are flatter than the hornblende samples and yield readily interpretable ages, although show small variations in step ages. (E) Plot of interpreted hornblend and biotite $^{40}Ar/^{39}Ar$ age versus distance in the slip direction. Ages generally young in the hanging wall slip direction (NE). Hornblende ages are all significantly older than the age of Miocene

detachment faulting (ca. 21 Ma). Biotite ages to the southwest of the mylonitic front are also older than the age of detachment faulting but are younger northeast of the front. The flattening of biotite ages northeast of the front reflects rapid cooling and exhumation during Miocene detachment faulting.

at the $^{40}Ar/^{39}Ar$ geochronology laboratory at UC Santa Barbara. Specific information and more detailed data on the $^{40}Ar/^{39}Ar$ analyses can be found in Supplementary Table S2.

$^{40}Ar/^{39}Ar$ analyses conducted on metamorphic hornblende from the central and NE-central footwall yield the oldest interpreted $^{40}Ar/^{39}Ar$ hornblende ages (Fig. 11b). Har-27 from the central Harcuvar Mountains yields an age spectrum that is relatively flat for 60% of the spectrum (weighted mean age of 66.7 ± 0.1 Ma but no well-defined isochron) with slightly older apparent ages for the highest temperatures steps. Har-71 from the NE-central Harcuvar Range yields a slightly hump-shaped age spectrum with most step ages ranging from 58.5–65 Ma and a weighted mean age of 64.3 ± 0.1 Ma for the flattest part of the age spectrum (80% of final gas release). Alternatively, the sample yields a four-point isochron age of 60.7 ± 0.4 Ma (MSWD = 0.8) that comprises 57% of the gas release ($^{40}Ar/^{36}Ar_{init}$ = 339 ± 4). Sample H-12 from the southwest end of the Little Buckskin range yields an age spectrum with a more pronounced age gradient that climbs from ca. 47–63 Ma with a flat segment at the highest temperature steps (comprising 35% of gas release with the highest radiogenic yields) with a weighted mean age of 63.1 ± 0.2 Ma. A four–point isochron yields a similar age of 66.4 ± 0.8 Ma with no well defined isochron.

Results from the northeastern-most footwall yield distinctly younger $^{40}Ar/^{39}Ar$ hornblende ages (Fig. 11c). Age spectra from these samples are similar in that they tend to climb from minimum ages of 24–37 Ma up to ages of 43–46 Ma for the first ~50% of gas release at low temperature and then flatten significantly for the second half of gas release at high temperature steps. Radiogenic yields follow a similar pattern for these samples. The flatter portion of the age spectrum for Har-43 yields a weighted mean age of 43.3 ± 0.1 Ma and a three-point isochron that comprises 40% of the gas yields a similar age of 43.4 ± 0.14 Ma (MSWD = 0.8, $^{40}Ar/^{36}Ar$ = 300.5 ± 10). The flatter portion of the H-32 age spectrum comprises 51% of the gas release and yields a weighted mean age of 45.2 ± 0.1 Ma. The flatter portion of the age spectra of H-24, from the northeasternmost Little Buckskin Mountains, produces a weighted mean age of 45.3 ± 0.1 Ma for the flat portion. No isochron could be reasonably fit to the H-32 or H-24 sample data. All of these spectra are best interpreted as reflecting varying degrees of argon loss or possibly very slow cooling of older (pre-45 Ma) hornblende.

While most of the $^{40}Ar/^{39}Ar$ hornblende data do not yield age spectra with simple plateaus, we interpret the preferred ages reported here as geologically meaningful and reflecting the time of footwall cooling through hornblende $^{40}Ar/^{39}Ar$ closure temperature of ~480–550°C (Harrison, 1981; McDougal and Harrison, 1988). Excess argon contamination can be a common issue with $^{40}Ar/^{39}Ar$ analyses of metamorphic hornblende, but the standard hallmarks of significant excess argon issues, such as strongly U-shaped spectra or highly irregular step ages (e.g. McDougall and Harrison, 1999) are not evident in the data. The isochron plots also do not suggest significant excess argon issues where good fits were possible. The spatial trend of hornblende ages that young towards the structurally deeper northeastern footwall also support that these ages are geologically meaningful. Given the correlation between the shape of the age spectra and radiogenic yields, the oldest high temperature age steps likely record cooling through hornblende closure temperature during the Late Cretaceous to Paleocene with the younger low temperature steps documenting moderate argon loss during alteration, perhaps during Miocene deformation. Taken together, these results suggest that most of the footwall had cooled through ~480–550°C by ca. 65 Ma and the entire footwall by ca. 43 Ma.

New $^{40}Ar/^{39}Ar$ biotite age results also shed light on the thermal history of the Harcuvar footwall. Overall, the $^{40}Ar/^{39}Ar$ biotite age spectra are relatively flat and show little complexity, making them readily interpretable (Fig. 11d). The biotite ages show clear spatial trends that consistently young towards the northeast, with a few minor anomalies. Biotite ages range from a maximum of 65.5 Ma in the southwesternmost footwall and young significantly to ca. 31–28 Ma ages in the central footwall near the mylonitic front. Further northeast, there is a distinct break in the age vs. distance slope (Fig. 11e) and $^{40}Ar/^{39}Ar$ biotite ages decrease from ca. 18 Ma to a minimum of 14.3 Ma in the northeasternmost footwall. These results indicate that the footwall southwest of the mylonitic front had cooled below 325 ± 30°C (biotite closure temperature, McDougall and Harrison, 1999) by the start of Miocene extension at ca. 21 Ma but the footwall northeast of the mylonitic front was above this temperature at that time.

3.8 U-Pb geochronology

Significant portions of the mylonitic zone in the Harcuvar footwall occur in leucogranite. Given the variability of deformation in this unit and its extensive presence within the footwall, we conducted LA–ICP–MS U-Pb zircon geochronology on leucogranite units, leucogranite/pegmatite dikes and sills, and other granite units, in order to constrain the timing of footwall magmatism and its relationship to deformation. U-Pb geochronology was conducted at the Laser Ablation Split Stream facility at the University of California, Santa Barbara. Analysis spots 20 µm in diameter were picked based on cathodoluminescence images of polished zircon mounts to avoid inherited cores and metamorphic overgrowths. For each sample, we report weighted mean U^{238}/Pb^{206} ages of analyses with <5% discordance. Data analysis was conducted using the IsoplotR program (Vermeesch, 2018) and we allowed the program to reject outlier ages for weighted mean age calculations.

Geochronologic results indicate that a major pulse of magmatism occurred in the latest Cretaceous to early Paleocene, with most leucogranite units yielding ages from ca. 74–64 Ma (Figure 12, Table 2). These results are similar to but somewhat younger than the 80–78 Ma U-Pb date of the type locality of the Tank Pass Granite in the western Harcuvar Mountains (DeWitt and Reynolds, 1990). We infer these leucogranitic intrusions to all be part of the Late Cretaceous Tank Pass granite suite and these results document a more protracted phase of magmatism during this time period than previously recognized. The preponderance of latest Cretaceous U-Pb ages in our results still undersells the volumetric significance of the leucogranites, which make up substantial portions of the Harcuvar Mountains footwall as stocks and sills intruded into other footwall units. These Late Cretaceous leucogranites are variably deformed, typically as intensely strained category 4 mylonites. Leucogranite units as young as ca. 64 Ma (Har-81, Table 2) record significant mylonitization in northeastern footwall.

Minor magmatism continued into the Paleocene and early Eocene, primarily in the form of rare pegmatite dikes. Although minor volumetrically, these units provide important constraints on the timing of footwall fabrics. In several localities in the Harcuvar and Little Buckskin mountains, rare pegmatite and leucogranite dikes cut the mylonitic foliation at high angles (Figure 13). These dikes are weakly deformed, with the surrounding mylonitic foliation feathering weakly into their margins. Given these characteristics, we interpret these dikes as synkinematic intrusions that were emplaced towards the end of mylonitization. One such dike (Har-50, strike and dip of 220/88 NW) cuts category 3-4 granitic mylonites at a high angle along the northwest flank of the Harcuvar footwall. Zircon U-Pb results on this dike yielded nearly concordant dates with a weighted mean age of 63.0 ± 0.5 Ma (MSWD = 1.2, n=7, Fig. 13). In the Cunningham Pass region in the central Harcuvar footwall, completely undeformed pegmatitic dikes crosscut foliation within a non-mylonitic biotite-feldspar gneiss. U-Pb dates from one of

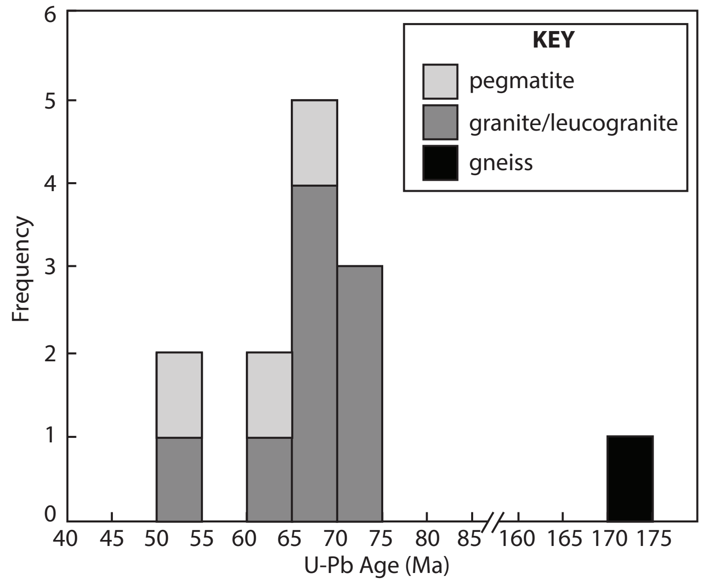

Figure 12. Summary histogram of U-Pb geochronology from the Harcuvar footwall. These analyses focused on the geochronology of the Tank Pass leucogranites, although some other granitic units and pegmatite dikes were also dated. The main pulse of magmatism in the Harcuvar footwall occurred from ca. 74-64 Ma, with minor magmatism (mainly pegmatite dikes) occurring until ca. 53 Ma. The Cretaceous leucogranites are a substantial volumetric unit and make up large portions of the Harcuvar footwall. Note the break in the age scale on the x-axis.

these dikes (Har-55) yield younger concordant ages that typically form zoned rims around inherited Jurassic cores, with the rim ages yielding a weighted mean age of 54.4 ± 0.7 Ma (MSWD = 1.2, n = 10).

4 Discussion

4.1 Temperature conditions of footwall mylonitization

The range of deformation styles evident from the microstructural data strongly suggest that footwall mylonites of the Harcuvar and Buckskin-Rawhide core complexes formed under a wide range of temperature conditions. At strain rates of ~10^{-12} to 10^{-13}/s^{-1}, quartz bulging recrystallization dominates in the lower greenschist-facies (~280–400°C; chlorite zone), whereas quartz subgrain rotation recrystallization dominates in the upper greenschist-facies (400–500°C), and grain boundary migration dominates in the amphibolite-facies (>500°C) (Stipp et al., 2002a; Faleiros et al., 2010). At slower strain rates of ~10^{-14}/s^{-1}, the transition from quartz bulging recrystallization to subgrain rotation recrystallization likely occurs in the lower greenschist-facies (~350°C), whereas the transition from subgrain rotation to grain boundary migration

Table 2. U-Pb Geochronologic Results

Sample name	Description	Latitude*	Longitude	# of analyzed spots†	U^{238}/Pb^{206} weighted mean age ± 2σ	MSWD
HAR-68A	unstrained leucogranite	33.7413	-113.6735	16	74.1 ± 0.7	4.0
HAR-72	mylonitic leucogranite	34.0822	-113.4194	3	70.2 ± 3.9	5.0
HAR-87	mylonitic leucogranite	34.0924	-113.3160	13	70.0 ± 1.2	12
HAR-42	protomylonitic leucogranite sill	34.1085	-113.2807	21	69.9 ± 0.6	4.0
LB-H-11	ultramylonitic leucogranite	34.0878	-113.5360	3	69.8 ± 1.9	1.8
HAR-48	mylonitic leucogranite sill	34.0322	-113.4746	10	68.9 ± 0.7	2.4
HAR-45	mylonitic leucogranite	34.1068	-113.2874	14	68.3 ± 0.5	2.1
HAR-84	mylonitic pegmatite dike	34.0789	-113.2990	21	67.3 ± 0.6	1.9
HAR-81	mylonitic leucogranite	34.0529	-113.3863	22	63.7 ± 0.4	0.8
HAR-50	protomylonitic pegmatite dike	34.0420	-113.4856	6	63.0 ± 0.5	1.2
HAR-55	unstrained pegmatite dike	33.9705	-113.5438	10	54.4 ± 0.7	1.2
HAR-54	fine grain granite sill	33.9705	-113.5436	7	54.2 ± 0.8	0.9

*Latitude and Longitude locations are given in the NAD27 datum.

† Spot analyses that yielded ages with >5% discordance are not reported here.

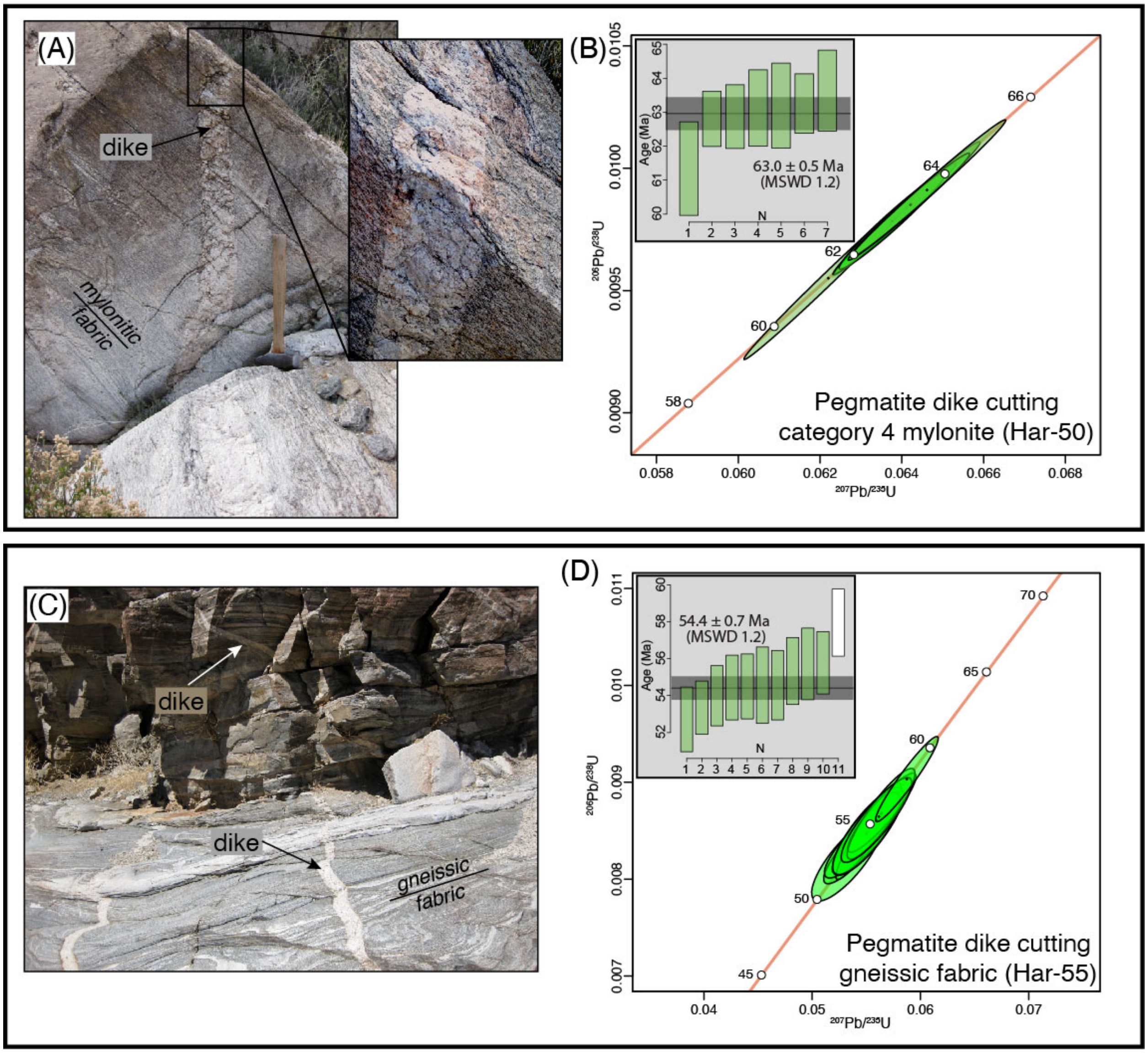

Figure 13. Images of cross-cutting pegmatite dikes and related U-Pb zircon geochronology. (A) Pegmatite dike (Har50) cross-cutting highly deformed category 4 mylonites at a high angle. Closeup view shows the straight but slightly feathered dike margins and a very weak fabric in the dike. (B) Concordia plot and weighted mean U-Pb ages (63.0 ± 0.5 Ma) of Har50 illustrating the concordant nature of the ages. (C) Pegmatite dikes (Har54) cutting gneissic fabrics in the central footwall. (D) Concordia plot and weighted mean U-Pb ages (54.2 ± 0.8 Ma) of the Har54 sample.

recrystallization likely occurs in the middle greenschist facies (~400°C) (Stipp et al., 2002b; Law, 2014).

The correlation between feldspar deformation mechanisms and temperature is complicated by several processes that may occur at a range of conditions, including chemically-driven alteration and breakdown, fracturing, diffusion creep, and solution-precipitation (e.g., Tullis and Yund, 1991; Fitz Gerald and Stunitz, 1993; Fukuda and Okudaira, 2013). Dislocation creep and subgrain rotation recrystallization typically become important in the amphibolite facies (Simpson, 1985; Gapais, 1989; Pryer, 1993; Fitz Gerald and Stunitz, 1993 and references therein; Kruse et al., 2001).

In the quartzofeldspathic category 4 mylonites in this study, the dominance of quartz grain boundary migration recrystallization and feldspar subgrain rotation recrystallization strongly suggest that deformation occurred in the amphibolite facies, likely >500°C. This temperature is consistent with the quartz CPO patterns, where the strong Y-axis strain maxima evident in most samples typically correlates with dominance of prism <a> slip and deformation temperatures >500°C (Law, 2014). The lack of evidence for prism <c> slip suggests that deformation temperatures were largely below ~600°C (Lister and Dornseipen, 1982; Mainprice et al., 1986; Okudaira et al., 1995; Stipp et al., 2002a). Although deformation mechanisms may be influenced by factors other than temperature, including water content and strain rate, the pervasive subgrain rotation recrystallization in feldspar and fast grain boundary migration in quartz observed in many of the category 3 and 4 samples likely requires temperatures >500° C, regardless of other variables. Moreover, estimates of strain rates during mylonitization along this belt of core complexes are relatively high (~10^{-11} to 10^{-14} s^{-1}; Behr and Platt, 2011; Campbell-Stone and John, 2002), so it is unlikely that low strain rates under greenschist-facies conditions account for development of these microstructures.

The Ti-in-quartz results provide independent support that deformation of category 3 and 4 mylonites occurred in the amphibolite facies, with the vast majority of samples in these categories yielding calculated temperatures >500°C within the error of the analyses, assuming 6 kbar pressure (Fig. 10). At 4 kbar, 7 of the 9 samples still yield calculated temperatures above 475°C within error. An important question is whether the Ti concentrations were fully reset during mylonitization. Nachlas et al. (2014) demonstrated that Ti concentrations in quartz were re-equilibrated during experimental dynamic recrystallization. In addition, Grujic et al. (2011) and Behr and Platt (2012) have applied these methods to well-constrained shear zones, demonstrating the utility of this approach in constraining mylonitization temperatures. A few of our results are somewhat more complex. For example, two of the category 3–4 samples yield calculated temperatures <500 °C and one category 2 sample yields a temperature above 500 °C (Fig. 10). These results are likely the product of uneven or partial re-equilibration during lower-temperature deformation. Grujic et al. (2011) noted that Ti diffusion at the greenschist facies may be too slow to fully reset the Ti system in quartz, and thus these temperatures may reflect significant Ti inheritance from the earlier high temperature mylonitization. This may especially be an issue when deformation is not accompanied by significant dynamic recrystallization (Nachlas et al., 2014). Aside from these minor complexities, the Ti-in-quartz results, when combined with the petrographic and EBSD data, strongly suggest that substantial portions of the mylonite zone were deformed under amphibolite-facies conditions (>500°C), especially in the Harcuvar, Little Buckskin, and southern Buckskin mountains (Fig. 8).

Our results also demonstrate that some mylonitization occurred at lower temperatures in the greenschist facies. The presence of quartz bulging recrystallization, the dominance of feldspar fracturing/cataclasis, significant chloritization and distinct CPO patterns of category 1 mylonites strongly suggest deformation in the middle to lower greenschist facies (e.g. Passchier and Trouw, 2005). Category 2 and 3 mylonites likely represent deformation in upper greenschist to lower amphibolite-facies conditions. In many areas, these samples may record an incomplete upper greenschist-facies overprint of amphibolite-facies (category 4) mylonitic fabrics. Greenschist-facies mylonites appear to be more widespread in the Buckskin-Rawhide footwall and within the metasedimentary carapace located <250 m below the detachment fault across the entire footwall but are rare within the crystalline core of the Harcuvar footwall (Figs. 8 and 9). Taken together, our results suggest that the mylonitic shear zone formed during both amphibolite and greenschist-facies conditions, and that there is a strong spatial control on the location of these distinct mylonite categories.

4.2 Timing of amphibolite vs. greenschist-facies mylonites

The presence of both greenschist and amphibolite-facies mylonites within the footwall raises important questions about the timing of footwall mylonitization and whether all of the deformation was coeval with Miocene core complex development. Given that the ca. 22–21 Ma Swansea Plutonic Suite in the Buckskin-Rawhide core complex was deformed at middle to upper greenschist-facies conditions (Singleton and Mosher, 2012), it is clear that significant mylonitization occurred in parts of the footwall in concert with the Miocene initiation of detachment faulting. The highest footwall deformation temperatures during Miocene extension were likely where Swansea Plutonic Suite magmatism was concentrated in the central part of the Buckskin-Rawhide core complex (Fig. 2). Accordingly, we interpret the prevalence of (category 2) upper greenschist-facies fabrics in the Swansea Plutonic Suite in the Buckskin-Rawhide footwall (Fig. 8) to record peak mylonitization conditions during Miocene core complex development.

Further away from the Swansea intrusions, the footwall was likely cooler in the Miocene, although our new $^{40}Ar/^{39}Ar$ biotite results, combined with those of Scott et al. (1998), demonstrate that the mylonitic footwall was hotter than biotite Ar closure temperature (325 ± 30°C) at the inception of Miocene extension. As a result, it is likely that all greenschist-facies mylonites across the study area are Miocene in age. The dominance of category 1 (middle- to lower greenschist-facies) fabrics in metasedimentary mylonites (Fig. 8) suggests that these relatively weak rocks preferentially absorbed Miocene strain directly below the detachment system as the footwall was sheared through the brittle-plastic transition. Although metasedimentary mylonites only form a thin footwall carapace (<1 to 100 m-thick) and are volumetrically minor, they were likely present along 25–35% of the detachment system in the Buckskin-Rawhide core complex (Singleton et al., 2018), and thus played an important role in absorbing Miocene detachment-related strain. Category 1 fabrics that were not developed in metasedimentary mylonites are largely found near the southwestern end of the mylonitic footwall and reflect shallower Miocene structural levels near the mylonitic front.

It is less clear whether the amphibolite-facies mylonites identified in this study also formed during Miocene extension or during an earlier and distinct tectonic event. Given that the geometries (Fig. 9) and top-NE kinematics (Fig. 5) of the two types of mylonites are indistinguishable, the simplest interpretation would be that both fabrics formed as part of the same Miocene extensional shear zone that evolved from amphibolite to greenschist-facies temperatures. However, this simple model is not supported by our results. First, the ~65–43 Ma $^{40}Ar/^{39}Ar$ hornblende ages from the Harcuvar footwall suggest that all of the mylonitic footwall had cooled below the amphibolite facies well before the Miocene (assuming a hornblende closure temperature of 525 ± 40°C; McDougall and Harrison, 1999). Although not all of the age spectra yield simple plateaus, the results are consistent with cooling through the closure temperature in the Paleocene-Eocene followed by variable Ar loss due to minor retrograde (Miocene?) alteration. The preservation of a hornblende age gradient in the slip direction (similar to the biotite data), with younger $^{40}Ar/^{39}Ar$ hornblende ages in the northeasternmost (structurally deepest) footwall (Fig. 11) also suggest that these data are geologically meaningful.

Previous work in the Buckskin-Rawhide footwall yielded similar 70–45 Ma $^{40}Ar/^{39}Ar$ hornblende ages (Richard et al., 1990; Scott, 1995; Fryxell in Bryant, 1995; Scott et al., 1998). Although Richard et al. (1990) reported a few ca. 29–26 Ma $^{40}Ar/^{39}Ar$ hornblende ages, these samples were located near the Early Miocene Swansea Plutonic Suite (Bryant, 1995) and likely experienced substantial argon loss during reheating. Thus, all available thermochronology suggests that, outside of local zones of Miocene reheating in the Buckskin-Rawhide footwall, the footwall had cooled below amphibolite-facies conditions no later than ca. 43 Ma and largely before ca. 65–60 Ma. These results strongly suggest that amphibolite-facies mylonites predate Miocene deformation and instead formed during a discrete event that predated the ca. 65–60 Ma $^{40}Ar/^{39}Ar$ hornblende cooling ages.

Our new U-Pb geochronologic results further refine the timing of this earlier phase of mylonitic deformation. The development of amphibolite-facies mylonitic fabrics in the Late Cretaceous Tank Pass leucogranite indicates that at least some of this deformation postdated the 74–64 Ma emplacement of this suite. The variably deformed nature of the Tank Pass leucogranite also suggests that this unit was intruded syn-tectonically and that various phases captured different degrees of deformation as it intruded the footwall. Finally, the weakly deformed ca. 63 Ma pegmatitic dike that cuts amphibolite-facies mylonites in the central Harcuvar footwall (Fig. 13) provides direct evidence that this phase of mylonitization was waning by the early Paleogene in that part of the footwall. The fact that some leucogranite units as young as ca. 64 Ma in the northeasternmost footwall record amphibolite-facies mylonitization suggests that some strain probably continued after ca. 64 Ma in the structurally deepest part of the footwall, likely aided by heating from intrusion of the leucogranites themselves. Taken together, the microstructural, thermochronologic and geochronologic results provide strong evidence that amphibolite-facies mylonitization occurred during a discrete event in the latest Cretaceous to early Paleogene.

4.3 Evidence for Late Cretaceous extension

The presence of pre-Miocene mylonitic fabrics within the footwalls of these core complexes raises important questions about the kinematics and tectonic significance of this older phase of mylonitization. It is perhaps not surprising that mylonitic deformation occurred in mid-crustal rocks in this region during the Late Cretaceous. During this time, the entire western margin of North America was experiencing subduction, and the Maria fold-and-thrust belt southwest of the study area experienced significant Cretaceous shortening (e.g. Hamilton 1982, 1987; Laubach et al. 1989; Spencer and Reynolds, 1990; Boettcher et al., 2002; Cawood et al., 2022). Within the study area, Cretaceous thrust faulting has been described in the Granite Wash Mountains (e.g. Laubach et al., 1989) and in the adjacent Harquahala Mountains (e.g., Richard, 1988). However, thrusting in these areas is interpreted as top-SW directed, whereas the kinematics of the amphibolite-facies mylonites in the Harcuvars are top-NE, which is the same as Miocene extension. In addition, shortening in the Maria fold-and-thrust belt was largely complete by ca. 80 Ma (e.g. Martin et al., 1982; Isachsen et al., 1999; Flansburg et al., 2021), whereas we interpret top-NE shearing to have continued until ca. 63 Ma. This suggests that amphibolite-facies mylonites record an earlier episode of top-NE extensional deformation during the latest Cretaceous. Other workers have also reported evidence for Late Cretaceous top-NE extension in the Maria fold-and-thrust belt and adjacent areas, including the Dome Rock Mountains (Boettcher and Mosher, 1998), Little Maria Mountains (Ballard and Ballard, 1990), Iron Mountains (Wells et al., 2002), and Granite Mountains (Salem, 2009), suggesting a significant and regional tectonic event. Taken together, these data suggest that amphibolite-facies mylonites in the Harcuvar and Rawhide-Buckskin core complexes accommodated top-NE extension during the latest Cretaceous.

Fundamental to this interpretation is the assumption that the footwall had a similar structural orientation during the latest Cretaceous as it did during top-NE directed Miocene extension. Thermochronologic data confirms that the exposed footwall dipped northeast in the Late Cretaceous. The 65.5 Ma $^{40}Ar/^{39}Ar$ biotite age from the southwestern Harcuvar footwall (Har68A, Fig. 11) suggests this part of the footwall cooled below 325 ± 30°C (biotite closure temperature, McDougall and Harrison, 1999) by the latest Cretaceous. A similar 64.5 ± 5 Ma zircon (U-Th)/He age from a Proterozoic granitoid in the southwesternmost footwall of the Buckskin detachment fault (Singleton et al., 2014) suggests that this part of footwall had cooled below ~180–200°C by that time. In contrast, the central and NE-central footwall must have been much hotter in the latest Cretaceous, as ca. 67–63 Ma $^{40}Ar/^{39}Ar$ hornblende ages from this area (Fig. 11) indicate cooling through hornblende closure temperatures of 525 ± 40°C at that time. Finally, the northeasternmost footwall must have been even hotter than ~525°C in the latest Cretaceous, given the ca. 43–45 Ma $^{40}Ar/^{39}Ar$ hornblende ages in this area. Taken together, these data strongly indicate that the northeastern footwall was >200–350°C hotter and therefore structurally deeper than the southwest footwall during the latest Cretaceous. As a result, we conclude that latest Cretaceous top-NE-directed mylonitization in the study area records normal-sense shear and an episode of extensional deformation with the same kinematics as that of Miocene extension.

The recognition of two discrete extensional fabrics raises questions about the prevalence of latest Cretaceous versus Miocene mylonitization. In the Harcuvar footwall, only the greenschist-facies mylonites can plausibly have formed in the Miocene. While upper greenschist-facies mylonities locally overprint structurally deeper portions of the Harcuvar footwall (producing category 2 and 3 mylonites), pervasive greenschist-facies mylonitization is limited a relatively narrow zone of mylonites ≤250 m below the detachment fault (Figs. 8 and 9). In the Buckskin-Rawhide footwall, significant Miocene mylonitation is evident from deformation of the Miocene Swansea Plutonic Suite (Singleton et al., 2012) and widespread upper greenschist-facies fabrics (Fig. 8), which almost certainly reflects hotter footwall temperatures associated with plutonism. Amphibolite-facies fabrics are locally preserved in the southern Buckskin-Rawhide footwall, where Late Cretaceous leucogranite is common and Swansea Plutonic Suite intrusions are rare. Thus, it is likely that the Buckskin-Rawhide footwall also experienced significant Late Cretaceous mylonitization, although it is more difficult to evaluate the extent of this phase of deformation given significant Miocene overprinting.

Significant Late Cretaceous extension should have produced thermal, metamorphic, and other geologic signals that could provide additional evidence for these interpretations. Previous $^{40}Ar/^{39}Ar$ thermochronology from the Colorado River Extensional Corridor indicate widespread cooling in the Late Cretaceous to early Cenozoic (e.g., Knapp and Heizler, 1990; Foster et al., 1990; Richard et al., 1990). While this cooling has been interpreted to record erosion (e.g., Knapp and Heizler, 1990) or refrigeration from flat slab subduction (e.g., Dumitru et al., 1991), we suggest it may instead record regional extensional exhumation during the latest Cretaceous to Paleogene. In addition, there is tantalizing thermobarometric evidence for significant tectonic exhumation during this time period. For example, Anderson et al. (1988) interpreted that Late Cretaceous granitoids in the lower plate of the Whipple Mountains core complex were emplaced at ~30 km and were exhumed to <20 km depths prior to Oligo-Miocene detachment faulting. This exhumation may record Laramide extensional unroofing. Similarly, Walsh et al. (2016) reported preliminary thermobarometry and monazite geochronology on rare pelitic garnet ± kyanite schists from the Harcuvar footwall that suggests Late Cretaceous (76–70 Ma) garnet growth during decompression from pressures as high at ~10 kbar to as low as ~4 kbar during that time. These data suggest a major exhumational event of ~4–6 kbar occurred during the Late Cretaceous. Finally, in the nearby northern Plomosa Mountains, the Late Cretaceous (~73 Ma) Orocopia Schist was underplated as a subduction complex and subsequently exhumed to ~3–5 km depths prior to ~21 Ma (Strickland et al. 2018; Spencer et al., 2018), requiring major exhumation before the inception of Miocene detachment faulting. Paleogene exhumation of the Orocopia Schist in southern Arizona has been associated with extension (Jacobson et al., 2002, 2007; Oyarzabal et al., 1997).

Although there is currently a lack of evidence for normal faulting and extensional basin formation in this region during the latest Cretaceous to Paleogene, there has been substantial Miocene denudation, which may have removed much of the surficial geologic evidence of this early phase of extension. It may also be difficult to distinguish older normal faults from Miocene structures, especially given the possibility of reactivation. Alternatively, Hodges and Walker (1992) presented a kinematic model whereby Late Cretaceous mid-crustal extension in the Western U.S. Cordillera was decoupled from upper-crustal deformation. Regardless, existing thermochronology and thermobarometry provide additional support for a significant exhumational event in the latest Cretaceous.

In summary, we conclude that both the footwalls of the Harcuvar and Buckskin-Rawhide core complexes experienced two discrete phases of top-NE extensional mylonitization: an earlier Late Cretaceous to early Paleogene phase followed by overprinting during Miocene extension. The earlier extensional fabrics are well preserved in the Harcuvar footwall where Miocene fabrics are limited, whereas the earlier fabrics are more strongly overprinted in the Buckskin-Rawhide core complex where Miocene magmatism locally reheated the footwall, allowing for more pervasive Miocene mylonitization.

4.4 Implications for core complex formation

Cordilleran metamorphic core complexes have long been interpreted as unique and enigmatic features of crustal extension owing in large part to their low-angle fault geometry, juxtaposition of brittle and ductile features, and the large magnitude and high rate of extension inferred to be integral to their formation (see reviews by Lister and Davis, 1989; Wernicke, 1995; Whitney et al., 2013; Platt et al., 2015). Central to most core complex models is the interpretation that they represent the product of a single phase of Cenozoic extension, where footwall mylonites represent the mid-crustal roots of coeval detachment fault systems (e.g., Wernicke, 1981; Davis et al., 1986; Lister and Davis, 1989; Spencer and Reynolds, 1991).

This study demonstrates that the tectonic evolution of at least some core complexes may be more protracted than these prior models recognized. Our results suggest that the Harcuvar and Rawhide-Buckskin core complexes experienced two discrete phases of extension and footwall mylonitization separated by more than 40 Myr, indicating a protracted and polyphase tectonic evolution. If this conclusion is broadly correct, it raises fundamental questions about the nature of core complexes and the processes by which they form.

One controversial aspect of core complexes has been the low-angle geometry of the mylonitic fabrics and bounding detachment fault. The central issue is whether these normal faults initiated and slipped at their present shallow dips (e.g., Wernicke, 1981, 1985; Scott and Lister, 1992) or formed at steep initial dips and were rotated to shallower dips through time either by rotation on other normal faults (e.g., Proffett, 1977; Gans et al., 1985; Wong and Gans, 2008) or by isostatic rebound (rolling hinge) processes (Buck, 1988; Wernicke and Axen, 1988). The initiation of low-angle normal faults is at odds with classic rock mechanics (Anderson, 1951), and slip on low-angle normal faults appears to be rare in actively extending regions (e.g., Jackson, 1987; Jackson and White, 1989; *cf.* Abers, 1991; Boncio et al., 2000), so this question is fundamental to our understanding of how faults form and slip.

The recognition of a polyphase extensional history at the Harcuvar and Buckskin-Rawhide core complexes adds a new dimension to this long-standing debate. If extension in these core complexes began in the Late Cretaceous, then subsequent Miocene extensional structures were superimposed on earlier crustal fabrics, which may have important mechanical consequences. Our results indicate that the Late Cretaceous shear zone was reactivated during Miocene extension and this pre-existing weakness may have allowed the crust to fail in non-ideal orientations, including at shallower angles than would be predicted for intact crust. Such a reactivation scenario also provides a compelling explanation for the identical geometries of Late Cretaceous and Miocene footwall fabrics in that Miocene structures inherited their orientation from pre-existing weaknesses established by the Late Cretaceous shear zone. In addition, pre-existing shear zones in the middle crust may rotate stress fields to non-Andersonian orientations and allow extensional failure at lower dips (e.g., Wu and Lavier, 2016). Recognition of a polyphase extensional history at these core complexes also raises questions about other fundamental aspects of core complex development including understanding the contribution of earlier phases of extension to the total magnitude and rate of detachment fault slip.

4.5 Regional tectonic implications

The recognition of substantial Late Cretaceous extension within this part of the North American Cordillera raises significant questions about the tectonic evolution of the region. One important question is what drove syn-orogenic extension during the latest Cretaceous. Many workers have evoked gravitational collapse of the Cretaceous Sevier orogen either during or immediately following crustal thickening (e.g., Hodges and Walker, 1992), and our results are consistent with such a model. The spatial and temporal association of voluminous Late Cretaceous Tank Pass leucogranite with coeval extensional fabrics strongly suggests that the leucogranite played an important role in this tectonic event. The leucogranite is typically peraluminous with two micas ± garnet, suggesting it was derived from significant crustal melting (Miller and Bradfish, 1980; Lee et al., 1981; Farmer and DePaolo, 1983; Haxel et al., 1984; Miller and Barton, 1990; Patiño-Douce et al., 1990; Wright and Wooden, 1991, see review by Chapman et al., 2021). This is consistent with a cycle of crustal thickening producing localized crustal melting from heating and dehydration-derived fluids, which triggered crustal collapse of overthickened crust (Figure 14).

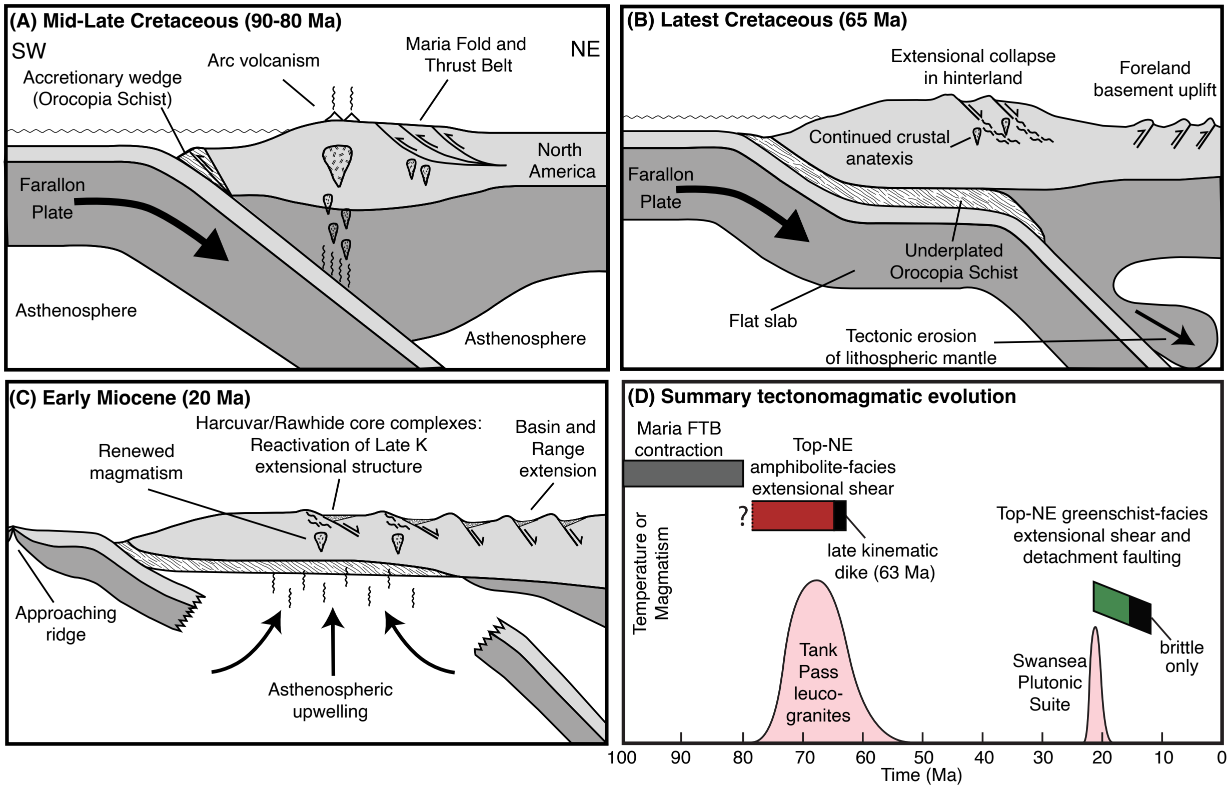

Figure 14. Schematic tectonic evolution of the Buckskin-Rawhide and Harcuvar core complexes in the context of the North American Cordillera. (A) South-vergent crustal shortening and thickening in the Maria fold and thrust belt was occurring during the mid-Late Cretaceous (ca. 90-80) as a result of the subduction of the Farallon plate beneath North America. Thickening generated significant crustal melting. The Pelona-Orocopia schist was forming within the accretionary wedge at that time. (B) During the latest Cretaceous (ca. 65 Ma) the overthickened crust was collapsing due to reheating, resulting in top-NE directed extension. Flat slab subduction of the Farallon underplated the Pelona-Orocopia schist beneath the study area, possibly with the tectonic erosion of some of the North American lithospheric mantle. (C) In the Early Miocene (ca. 21-20 Ma), extension and magmatism resumed, perhaps due to the emergence of a slab window or gap and the resultant influx of heat. In the Rawhide-Buckskin and Harcuvar core complexes, Miocene extension reactivated existing Late Cretaceous extensional structures whereas elsewhere, typical "Basin and Range" extension occurred. (D) Summary chart of the proposed tectonomagmatic evolution of the region.

An important element of this model is the assumption that substantial crustal thickening occurred within the Maria fold-and-thrust belt during mid- to Late Cretaceous contraction. While there are a number of mapped thrust faults and other contractional features documented in the region, the magnitude of crustal shortening and thickening in the region during Sevier/Laramide time remains poorly known. However, Chapman et al. (2020) applied geochemical proxies to suggest that crustal thickness in southern United States Cordillera during the Laramide orogeny (ca. 80–40 Ma) was 57 ± 12 km. In addition, preliminary thermobarometry and monazite geochronology on rare pelitic garnet ± kyanite schists from the Harcuvar Mountains suggests that Late Cretaceous metamorphism occurred at 6–10 kbar pressures at ca. 76–70 Ma (Walsh et al., 2016). Although Spencer et al. (2018) argued that any crustal welt in the region may have been tectonically removed from the base of the crust as a result of Laramide emplacement of the Orocopia Schist (Jacobson et al., 2017; Seymour et al., 2018; Strickland et al., 2018) during low-angle subduction, it is unclear that schist emplacement requires the removal of a Cretaceous crustal welt. Given the strong temporal overlap between Tank Pass leucogranite emplacement and Late Cretaceous extension, combined with the recent evidence for substantial early Laramide-age crustal thickening in the region, our preferred tectonic model is that crustal thickening drove heating and local anatexis which triggered collapse of overthickened crust.

Other tectonic models are also viable and may have acted alone or in concert with an orogenic collapse model. For example, tectonic underplating of the Orocopia Schist during the Laramide may have triggered extension by emplacing rheologically weak schist in the middle to lower crust and/or by hydration weakening due to dehydration reactions (Strickland et al., 2018). Alternatively, synorogenic extension may have been triggered by mantle delamination via density-driven foundering, as has been suggested for the North American Cordillera as a whole (Wells and Hoisch, 2008). Mantle delamination would result in elevated geothermal gradients, partial melting, and rock uplift, which might drive extension. Finally, regional Late Cretaceous extension may have been driven by the subduction of thickened oceanic crust (conjugate of the Shatsky Rise) on the Farallon slab and its passage through this region (Saleeby, 2003; Chapman et al., 2010). This proposed aseismic ridge may have driven low-angle subduction during the Laramide orogeny in the Late Cretaceous to early Paleogene, and the trailing edge of the rise is modeled to have passed through the region at ca. 68 Ma (e.g., Liu et al., 2010).

Looking more broadly at the North American Cordillera as a whole, a number of studies have suggested that the Cordillera experienced significant extensional exhumation during the Late Cretaceous to early Cenozoic (e.g. Hodges and Walker, 1992; Applegate and Hodges, 1995; Wells and Hoisch, 2008), but such studies have often relied on thermobarometric data, and the structures that may have accomplished such exhumation are commonly unclear. This study is significant in that it identifies a structure that accommodated significant extension in the middle crust during the latest Cretaceous. However, this does not resolve the question of why such structures remain poorly identified throughout the Cordillera. We speculate that many other Cordilleran core complexes experienced a similar polyphase tectonic evolution with an older period of extension, but tectonic inheritance and middle Cenozoic overprinting effects may make it difficult to recognize these older footwall fabrics. We anticipate that future studies applying new analytical tools will be able to test this hypothesis.

5 Conclusions

The mylonitic shear zones of the Harcuvar and Rawhide-Buckskin core complexes are the result of two distinct phases of crustal extension. Amphibolite-facies mylonitization had top-NE kinematics and occurred during the Late Cretaceous to early Paleogene. This deformation was spatially associated with voluminous ca. 74–64 Ma footwall leucogranites, which were emplaced syn-kinematically. A late kinematic ca. 63 Ma dike indicates this phase of mylonitization had largely waned by the early Paleogene. The leucogranites were likely the result of crustal melting due to orogenic thickening, implying a model whereby crustal heating from thickening and magmatism triggered gravitational collapse of overthickened crust, although the tectonic underplating of Orocopia Schist and/or mantle delamination may have also played a role in triggering orogenic collapse. Miocene footwall mylonitization occurred in the greenschist facies and is largely restricted to areas within and near the Early Miocene Swansea Plutonic Suite and narrow (<250 m-thick) zones immediately below the detachment fault. Miocene extension was superimposed on the latest Cretaceous to early Paleocene shear zone and had similar kinematics, suggesting that the location and geometry of Miocene extension was strongly influenced by tectonic inheritance. The tectonic development of these core complexes was more protracted and polyphase than previously recognized, suggesting that models of core complex development may need to be reevaluated.

Acknowledgments

This work was supported by the National Science Foundation grant number EAR-1321407 and by the Malcolm ’54 and Sylvia Boyce Fund for Geology Research at Colgate University. We thank Colgate undergraduates Jacky Baughman and Austin Sun for assistance with some of the EBSD measurements and Sam Jackson for work on some of the U-Pb geochronology. Andrew Kylander-Clark provided assistance with the U-Pb geochronology at the

Laser Ablation Split Stream facility at the University of California, Santa Barbara and Rick Hervig at Arizona State University provided assistance with the Ti-in-quartz analyses.

Open Research

Additional figures and data on sample characterization, petrographic analyses, U-Pb and $^{40}Ar/^{39}Ar$ geochronology are provided in the supplementary materials. Topographic maps were generated using the GeoMapApp available at https://www.geomapapp.org and using data from the U.S. Geological Survey's National Elevation Dataset available from https://apps.nationalmap.gov/downloader/. Stereonet plots were generated using Stereonet 10.1.6, which is available at https://www.rickallmendinger.net/. U-Pb geochronology figures were generated using IsoplotR (Vermeesch, 2018) which is available at http://www.isoplotr.com/isoplotr/home/index.html. Analysis of the crystallographic preferred orientation data was conducted using the MTEX toolbox (Bachmann et al., 2010), which is available at https://mtex-toolbox.github.io.

References

Abers, G. A. (1991). Possible seismogenic shallow-dipping normal faults in the Woodlark-D'Entrecasteaux extensional province, Papua New Guinea. *Geology*, *19*(12), 1205-1208.

Anderson, E.M. (1951). *The dynamics of faulting and dyke formation, with applications to Britain*, ed. 2., 183 pp., Oliver and Boyd, Edinburgh.

Anderson, J.L. (1988). Core complexes of the Mojave-Sonoran Desert: Conditions of plutonism, mylonitization, and decompression. In Ernst, W.G. (Ed.), *Metamorphism and crustal evolution of the western United States,* Rubey (Vol. 7, pp. 503-525).

Applegate, J. D. R., & Hodges, K. V. (1995). Mesozoic and Cenozoic extension recorded by metamorphic rocks in the Funeral Mountains, California. *Geological Society of America Bulletin*, 107(9), 1063-1076.

Axen, G.J. (1992). Pore pressure, stress increase, and fault weakening in low-angle normal faulting. *Journal of Geophysical Research*, v. 97, p. 8979-8991.

Bachmann, F., Hielscher, R., and Schaeben, H. (2010). Texture Analysis with MTEX - Free and Open Source Software Toolbox. *Solid State Phenomena*, v. 160, pp. 63-68.

Ballard, S.N., and Ballard, P.D. (1990). Geology of the Little Maria Mountains, western end of the Maria tectonic belt, southeastern Mojave, California. *Geological Society of America Abstracts with Programs*, v. 22, p. A140.

Behr, W.M., Platt, J.P. (2011). A naturally constrained stress profile through the middle crust in an extensional terrane. *Earth and Planetary Science Letters*, v. 303, p. 181-192.

Behr, W. M., Thomas, J. B., & Hervig, R. L. (2011). Calibrating Ti concentrations in quartz for SIMS determinations using NIST silicate glasses and application to the TitaniQ geothermobarometer. *American Mineralogist*, *96*(7), 1100-1106.

Bestmann, M., & Pennacchioni, G. (2015). Ti distribution in quartz across a heterogeneous shear zone within a granodiorite: The effect of deformation mechanism and strain on Ti resetting. *Lithos*, *227*, 37-56.

Beyene, M. A. (2011). *Mesozoic burial, Mesozoic and Cenozoic exhumation of the Funeral Mountains core complex, Death Valley, Southeastern California* (Doctoral dissertation). Retrived from Digital Scholarship@UNLV (https://digitalscholarship.unlv.edu/thesesdissertations/1386/). University of Nevada, Las Vegas.

Block, L., and Royden, L.H. (1990). Core complex geometries and regional scale flow in the lower crust. *Tectonics*, v. 9, pp. 557-567.

Boettcher, S.S., Mosher, S., and Tosdal, R.M. (2002). Structural and tectonic evolution of Mesozoic basement-involved fold nappes and thrust faults in the Dome Rock Mountains, Arizona. In Barth, A. (Ed.). *Contributions to Crustal Evolution of the Southwestern United States*, *Geological Society of America Special Paper* (Vol. 365, pp. 73-97).

Boettcher, S.S., Mosher, S. (1998). Mid- to Late Cretaceous ductile deformation and thermal evolution of the crust in the northern Dome Rock Mountains, Arizona. *Journal of Structural Geology*, v. 20, pp. 745-764.

Boncio, P., Brozzetti, F., & Lavecchia, G. (2000). Architecture and seismotectonics of a regional low-angle normal fault zone in central Italy. *Tectonics*, *19*(6), 1038-1055.

Bryant, B. (1995). *Geologic map, cross sections, isotopic dates, and mineral deposits of the Alamo Lake 30' x 60' Quadrangle, west-central Arizona*. U.S. Geological Survey Miscellaneous Investigations Series, Map 1-2489, scale 1:100,000.

Bryant, B., and Wooden, J.L. (2008). Geology of the northern part of the Harcuvar complex, west-central Arizona. *U.S. Geological Survey Professional Paper 1752*, 52 p.

Buck, W. R. (1988). Flexural rotation of normal faults. *Tectonics*, *7*(5), 959-973.

Buck, W.R. (1991). Modes of continental lithospheric extension. *Journal of Geophysical Research: Solid Earth*, *96* (B12), pp.20161-20178.

Campbell-Stone, E., & John, B. E. (2002). Temporal changes in deformation mode: From failure to flow in the Colorado River extensional corridor. *International Geology Review*, *44*(6), 512-527.

Cawood, T.K., Moser, A., Borsook, A. and Rooney, A.D. (2022). New constraints on the timing and character of the Laramide Orogeny and associated gold mineralization in SE California, USA. *Geological Society of America Bulletin*. Advanced online publication. doi:10.1130/B36251.1

Carter, T.J., Kohn, B.P., Foster, D.A., and Gleadow, A.J.W. (2004). How the Harcuvar Mountains metamorphic core complex became cool: Evidence from apatite (U-Th)/He thermochronometry. *Geology*, v. 32, pp. 985-988.

Chapman, J.B., Greig, R. and Haxel, G.B. (2020). Geochemical evidence for an orogenic plateau in the southern US and northern Mexican Cordillera during the Laramide orogeny. *Geology*, v. 48(2), pp.164-168.

Chapman, J. B., Runyon, S. E., Shields, J. E., Lawler, B. L., Pridmore, C. J., Scoggin, S. H., ... & Haxel, G. B. (2021). The North American Cordilleran Anatectic Belt. *Earth-Science Reviews*, *215*, 103576.

Chapman, A. D., Kidder, S., Saleeby, J. B., & Ducea, M. N. (2010). Role of extrusion of the Rand and Sierra de Salinas schists in Late Cretaceous extension and rotation of the southern Sierra Nevada and vicinity. *Tectonics*, *29*(5). doi:10.1029/2009TC002597

Cross, A. J., Kidder, S., & Prior, D. J. (2015). Using microstructures and TitaniQ thermobarometry of quartz sheared around garnet porphyroclasts to evaluate microstructural evolution and constrain an Alpine Fault Zone geotherm. *Journal of Structural Geology*, *75*, 17-31.

Davis, G.A., Lister, G.S., and Reynolds, S.J. (1986). Structural evolution of the Whipple and South Mountains shear zones, southwestern United States. *Geology*, v. 14, pp. 7-10.

DeWitt, E., & Reynolds, S. J. (1990). Late Cretaceous plutonism and cooling in the Maria fold and thrust belt, west-central Arizona. In *Geol. Soc. Am. Abstr. Programs* (Vol. 22, No. 3, p. 18).

Ducea, M.N., Triantafyllou, A. and Krcmaric, J. (2020). New timing and depth constraints for the Catalina metamorphic core complex, southeast Arizona. *Tectonics*, 39(8). doi:10.1029/2020TC006383

Dumitru, T. A., Gans, P. B., Foster, D. A., & Miller, E. L. (1991). Refrigeration of the western Cordilleran lithosphere during Laramide shallow-angle subduction. *Geology*, *19*(11), 1145-1148.

Farmer, G. L., & DePaolo, D. J. (1983). Origin of Mesozoic and Tertiary granite in the western United States and implications for Pre-Mesozoic crustal structure: 1. Nd and Sr isotopic studies in the geocline of the Northern Great Basin. *Journal of Geophysical Research: Solid Earth*, *88*(B4), 3379-3401.

Fukuda, J. I., & Okudaira, T. (2013). Grain-size-sensitive creep of plagioclase accompanied by solution–precipitation and mass transfer under mid-crustal conditions. *Journal of Structural Geology*, *51*, 61-73.

Faleiros, F.M., da Cruz Campanha, G.A., da Silveira Bello, R.M., Fuzikawa, K. (2010). Quartz recrystallization regimes, c-axis texture transitions and fluid inclusion reequilibration in a prograde greenschist to amphibolite facies mylonite zone (Ribeira Shear Zone, SE Brazil). *Tectonophysics*, 485 (1–4), pp. 193–214.

Faleiros, F.M., Moraes, R.D., Pavan, M., Campanha, G.A.D.C. (2016). A new empirical calibration of the quartz c-axis fabric opening-angle deformation thermometer. *Tectonophysics*, 671, 173–182.

Gerald, J. F., & Stünitz, H. (1993). Deformation of granitoids at low metamorphic grade. I: Reactions and grain size reduction. *Tectonophysics*, *221*(3-4), 269-297.

Flansburg, M.E., Stockli, D.F., and Singleton, J. (2021). Multi-mineral U-Pb geo- and thermochronology of Late Cretaceous-Paleocene deformation in the Maria fold-and-thrust belt (SW USA). *Geological Society of America Abstracts with Programs,* v. 51, no. 5, doi: 10.1130/abs/2019AM-337873.

Foster, D. A., Harrison, T. M., Miller, C. F., & Howard, K. A. (1990). The $^{40}Ar/^{39}Ar$ thermochronology of the eastern Mojave Desert, California, and adjacent western Arizona with implications for the evolution of metamorphic core complexes. *Journal of Geophysical Research: Solid Earth*, *95*(B12), 20005-20024.

Foster, D.A., and John, B.E. (1999). Quantifying tectonic exhumation in an extensional orogen with thermochronology: Examples from the southern Basin and Range province. In Lister, G.S., and Willett, S.D. (Eds.), *Exhumation processes: Normal faulting, ductile flow and erosion*, *Geological Society of London Special Publication* (Vol. 154, p. 343-364).

Gallagher, C., & Bromiley, G. (2013). Ti in quartz standards. Retrieved from https://www.ed.ac.uk/geosciences/about/facilities/all/ionprobe/technical/standards/quartz/composition

Gans, P.B. (1987), An open-system, two-layer crustal stretching model for the eastern Great Basin. *Tectonics*, *6*(1), pp.1-12.

Gans, P., Miller, E. L., McCarthy, J., & Ouldcott, M. L. (1985). Tertiary extensional faulting and evolving ductile-brittle transition zones in the northern Snake Range and vicinity: New insights from seismic data. *Geology*, *13*(3), pp. 189-193.

Gans, P.B., and Gentry, B.J. (2016). Dike emplacement, footwall rotation, and transition from magmatic to tectonic extension in the Whipple Mountains metamorphic core complex, southeastern California. *Tectonics*, v. 35, p. 2564–2608, doi:10.1002 /2016TC004215.

Gapais, D. (1989). Shear structures within deformed granites: mechanical and thermal indicators. *Geology*, *17*(12), 1144-1147.

Ghent, E. D., & Stout, M. Z. (1984). TiO2 activity in metamorphosed pelitic and basic rocks: principles and applications to metamorphism in southeastern Canadian Cordillera. *Contributions to Mineralogy and Petrology*, *86*(3), 248-255.

Gottardi, R., McAleer, R., Casale, G., Borel, M., Iriondo, A., & Jepson, G. (2020). Exhumation of the Coyote Mountains metamorphic core complex (Arizona): Implications for orogenic collapse of the southern North American Cordillera. *Tectonics*, *39*(8), e2019TC006050.

Grujic, D., M. Stipp, and J. L. Wooden (2011). Thermometry of quartz mylonites: Importance of dynamic recrystallization on Ti-in-quartz reequilibration. *Geochemistry, Geophysics and Geosystems.*, v. 12, Q06012, doi:10.1029/2010GC003368

Hacker, B.R., Yin, A., Christie, J.M., and Davis, G.A. (1992). Stress magnitude, strain rate, and rheology of extended middle continental crust inferred from quartz grain sizes in the Whipple Mountains, California. *Tectonics*, v. 11, p. 36-46.

Hamilton, W. (1982). Structural evolution of the Big Maria Mountains, northeastern Riverside county, southeastern California. In Frost, E.G., and Martin, D.L., (Eds.)*, Mesozoic-Cenozoic tectonic evolution of the Colorado River region, California, Arizona, and Nevada.* San Diego, Calif., Cordilleran Publishers, p. 1–27.

Haxel, G. B., Tosdal, R. M., May, D. J., & Wright, J. E. (1984). Latest Cretaceous and early Tertiary orogenesis in south-central Arizona: Thrust faulting, regional metamorphism, and granitic plutonism. *Geological Society of America Bulletin,* 95(6), 631-653.

Haxel, G.B., Jacobson, C.E., and Wittke, J.H. (2014). Mantle peridotite in newly discovered far-inland subduction complex, southwest Arizona: Initial report. *International Geology Review*, v. 57, pp. 871–892.

Hodges, K. V., & Walker, J. D. (1992). Extension in the Cretaceous Sevier orogen, North American Cordillera. *Geological Society of America Bulletin*, 104(5), pp. 560-569.

Isachsen, C. E., Gehrels, G. E., Riggs, N. R., Spencer, J. E., Ferguson, C. A., Skotnicki, S. J., & Richard, S. M. (1999). U-Pb geochronologic data from zircons from eleven granitic rocks in central and western Arizona. *Arizona Geological Survey Open-file Report*, n. 99-5.

Jackson, J. A. (1987). Active normal faulting and crustal extension. *Geological Society, London, Special Publications*, *28*(1), 3-17.

Jackson, J. A., & White, N. J. (1989). Normal faulting in the upper continental crust: observations from regions of active extension. *Journal of Structural Geology*, *11*(1-2), 15-36.

Jacobson, C.E., Grove, M., Stamp, M.M., Vucic, A., Oyarzabal, F.R., Haxel, G.B., Tosdal, R.M., and Sherrod, D.R. (2002). Exhumation history of the Orocopia Schist and related rocks in the Gavilan Hills area of southeasternmost California. In Barth, A. (Ed.), *Contributions to Crustal Evolution of the Southwestern United States*. Geological Society of America Special Papers, v. 365, p. 129-154, doi:10.1130/0-8137-2365-5.129

Jacobson, C. E., Grove, M., Vucic, A., Pedrick, J. N., & Ebert, K. A. (2007). Exhumation of the Orocopia Schist and associated rocks of southeastern California: Relative roles of erosion, synsubduction tectonic denudation, and middle Cenozoic extension.

Jacobson, C.E., Hourigan, J.K., Haxel, G.B., and Grove, M. (2017). Extreme latest Cretaceous low-angle subduction: Zircon ages from Orocopia Schist at Cemetery Ridge, southwest Arizona, USA. *Geology*, v. 45, p. 951–954, doi:10.1130/G39278.1

John, B.E., and Musaka, S.B. (1990). Footwall rocks to the mid-Tertiary Chemehuevi detachment fault: A window into the middle crust in southern California. *Journal of Geophysical Research*, v. 95, p. 463-485.

John, B.E. (1987). Geometry and evolution of a mid-crustal extensional fault system: Chemehuevi Mountains, southeastern California. In Coward, M.P., Dewey, J.F., and Hancock, P.L. (Eds.), *Continental extensional tectonics, Geological Society of London Special Publication* (Vol. 28, p. 313-335).

John, B.E., and Foster, D.A. (1993) Structural and thermal constraints on the initiation of detachment faulting in the southern Basin and Range: the Chemehuevi Mountains case study. *Geological Society of America Bulletin*, v. 105, p. 1091-1108.

Kidder, S., Avouac, J. P., & Chan, Y. C. (2013). Application of titanium-in-quartz thermobarometry to greenschist facies veins and recrystallized quartzites in the Hsüehshan range, Taiwan. *Solid Earth*, *4*(1), 1-21.

Kidder, S. B., Toy, V. G., Prior, D. J., Little, T. A., Khan, A., & MacRae, C. (2018). Constraints on Alpine Fault (New Zealand) mylonitization temperatures and the geothermal gradient from Ti-in-quartz thermobarometry. *Solid Earth*, *9*(5), 1123-1139.

Knapp, J. H., & Heizler, M. T. (1990). Thermal history of crystalline nappes of the Maria fold and thrust belt, west central Arizona. *Journal of Geophysical Research: Solid Earth*, *95*(B12), 20049-20073.

Kohn, M. J., & Northrup, C. J. (2009). Taking mylonites' temperatures. *Geology*, *37*(1), 47-50.

Kruse, R., Stünitz, H., & Kunze, K. (2001). Dynamic recrystallization processes in plagioclase porphyroclasts. *Journal of Structural Geology*, *23*(11), 1781-1802.

LaForge, J., John, B. E., Grimes, C. B., Stunitz, H., & Heilbronner, R. (2016). Initiation of a Low-Angle Normal Fault Active Across the Upper Brittle-Plastic Transition, Chemehuevi

Mountains, CA. *American Geophysical Union Fall Meeting Abstracts* (Vol. 2016, pp. T11E-03).

Laubach, S.E., Reynolds, S.J., Spencer, J.E., and Marshak, S. (1989). Progressive deformation and superposed fabrics related to Cretaceous crustal underthrusting in western Arizona, U.S.A. *Journal of Structural Geology*, v. 11, p. 735-749.

Laubach, S. E., Reynolds, S. J., Spencer, J. E., & Marshak, S. (1989). Progressive deformation and superposed fabrics related to Cretaceous crustal underthrusting in western Arizona, USA. *Journal of Structural Geology*, *11*(6), 735-749.

Law, R.D., (2014). Deformation thermometry based on quartz c-axis fabrics and recrystallization microstructures: A review. *Journal of Structural Geology*, v. 66, pp. 129-161.

Lee, D. E., Kistler, R. W., Friedman, I., & Van Loenen, R. E. (1981). Two-mica granites of northeastern Nevada. *Journal of Geophysical Research: Solid Earth*, *86*(B11), 10607-10616.

Lister, G. S., & Davis, G. A. (1989). The origin of metamorphic core complexes and detachment faults formed during Tertiary continental extension in the northern Colorado River region, USA. *Journal of Structural Geology*, v. 11(1-2), pp. 65-94.

Lister, G.S., and Davis, G.A. (1989). The origin of metamorphic core complexes and detachment faults formed during Tertiary continental extension in the northern Colorado River region, U.S.A. *Journal of Structural Geology*, v. 11, pp. 65-94.

Lister, G. S., & Dornsiepen, U. F. (1982). Fabric transitions in the Saxony granulite terrain. *Journal of Structural Geology*, *4*(1), 81-92.

Liu, L., Gurnis, M., Seton, M., Saleeby, J., Müller, R. D., & Jackson, J. M. (2010). The role of oceanic plateau subduction in the Laramide orogeny. *Nature Geoscience*, *3*(5), pp. 353-357.

Lucchitta, I., and Suneson, N.H. (1993), Dips and extension. *Geological Society of America Bulletin*, v. 105, pp. 1346-1356.

Lucchitta I., and Suneson, N.H. (1996), Timing and character of deformation along the margin of a metamorphic core complex, west-central Arizona. In Beratan, K.K.. (Ed.), *Reconstructing the history of Basin and Range extension using sedimentology and stratigraphy, Geological Society of America Special Paper* (Vol. 303, p. 147-170).

Lyle, J.H., III (1982). Interrelationships of late Mesozoic thrust faulting and mid-Tertiary detachment faulting in the Riverside Mountains, southeastern California. In Frost, E.G., and Martin, D.L. (Eds.), *Mesozoic-Cenozoic tectonic evolution of the Colorado River region, California, Arizona, and Nevada* (, p. 470-491). Cordilleran Publishers, San Diego, CA.

Mainprice, D., Bouchez, J. L., Blumenfeld, P., & Tubià, J. M. (1986). Dominant c slip in naturally deformed quartz: Implications for dramatic plastic softening at high temperature. *Geology*, *14*(10), 819-822.

Martin, D. L., Krummenacher, D., & Frost, E. G. (1982). K-Ar geochronologic record of Mesozoic and Tertiary tectonics of the Big Maria-Little Maria-Riverside Mountains terrane. In Frost, E.G., and Martin, D.L. (Eds.), *Mesozoic-Cenozoic tectonic evolution of the Colorado River region, California, Arizona, and Nevada*. Cordilleran Publishers, San Diego, CA, pp. 518-549.

McDougall, I., & Harrison, T. M. (1999). *Geochronology and Thermochronology by the $^{40}Ar/^{39}Ar$ Method*. Oxford University Press on Demand.

McKenzie, D., Nimmo, F., Jackson, J.A., Gans, P.B., and Miller, E.L. (2000). Characteristics and consequences of flow in the lower crust. *Journal of Geophysical Research*, v. 105, p. 11029-11046.

Miller, C.F., and Barton, M.D. (1990). Phanerozoic plutonism in the Cordilleran Interior, U.S.A.. In Suzanne Mahlburg Kay, Carlos W. Rapela (Eds.), *Plutonism from Antarctica to Alaska*, Geological Society of America Special Papers, v. 241, pp. 213-231.

Miller, C. F., & Bradfish, L. J. (1980). An inner Cordilleran belt of muscovite-bearing plutons. *Geology*, *8*(9), 412-416.

Miller, E.L., Dumitru, T.A., Brown, R.W. and Gans, P.B. (1999). Rapid Miocene slip on the Snake Range– Deep Creek range fault system, east-central Nevada. *Geological Society of America Bulletin*, v. 111(6), pp.886-905.

Nachlas, W. O., Whitney, D. L., Teyssier, C., Bagley, B., & Mulch, A. (2014). Titanium concentration in quartz as a record of multiple deformation mechanisms in an extensional shear zone. *Geochemistry, Geophysics, Geosystems*, *15*(4), 1374-1397.

Nachlas, W. O., Thomas, J. B., & Hirth, G. (2018). TitaniQ deformed: Experimental deformation of out-of-equilibrium quartz porphyroclasts. *Journal of Structural Geology*, *116*, 207-222.

Okudaira, T., Takeshita, T., Hara, I., & Ando, J. I. (1995). A new estimate of the conditions for transition from basal< a> to prism [c] slip in naturally deformed quartz. *Tectonophysics*, *250*(1-3), 31-46.

Oyarzabal, F. R., Jacobson, C. E., & Haxel, G. B. (1997). Extensional reactivation of the Chocolate Mountains subduction thrust in the Gavilan Hills of southeastern California. *Tectonics*, *16*(4), 650-661.

Passchier, C. W., & Trouw, R. A. (2005). *Microtectonics*. Springer Science & Business Media.

Patino-Douce, A. E., Humphreys, E. D., and Johnston, A. D. (1990). Anatexis and metamorphism in tectonically thickened continental crust exemplified by the Sevier Hinterland, western North America. *Earth and Planetary Science Letters*, v. 97, p. 290–315.

Prior, M.G., Stockli, D.F., and Singleton, J.S. (2016). Miocene slip history of the Eagle Eye detachment fault, Harquahala Mountains metamorphic core complex, west-central Arizona. *Tectonics*, v. 35, pp. 1913–1924.

Prior, M.G, Singleton, J.S., and Stockli, D.F. (2018). Late-stage slip history of the Buckskin-Rawhide detachment fault and temporal evolution of the Lincoln Ranch supradetachment basin: New constraints from the middle Miocene Sandtrap Conglomerate. *Geological Society of America Bulletin*, v. 130, pp. 1747–1760.

Proffett, J. M. (1977). Cenozoic geology of the Yerington district, Nevada, and implications for the nature and origin of Basin and Range faulting. *Geological Society of America Bulletin*, *88*(2), 247-266.

Pryer, L. L. (1993). Microstructures in feldspars from a major crustal thrust zone: the Grenville Front, Ontario, Canada. *Journal of structural Geology*, *15*(1), 21-36.

Rehrig, W.A., and Reynolds, S.J. (1980). Geologic and geochronologic reconnaissance of a northwest-trending zone of metamorphic core complexes in southern and western Arizona. In Crittenden, M.L., Coney, P.J., and Davis, G.H (Eds.), *Cordilleran Metamorphic Core Complexes, Geological Society of America Memoir* (Vol. 153, pp. 131-157).

Reynolds, S. J., & Lister, G. S. (1990). Folding of mylonitic zones in Cordilleran metamorphic core complexes: Evidence from near the mylonitic front. *Geology*, *18*(3), 216-219.

Reynolds, S. J., and J. E. Spencer (1985). Evidence for large-scale transport on the Bullard detachment fault, west-central Arizona. *Geology*, v.13, pp. 353–356.

Reynolds, S.J., Shafiqullah, M., Damon, P.E. and DeWitt, E. (1986). Early Miocene mylonitization and detachment faulting, South Mountains, central Arizona. *Geology*, v. 14, pp.283-286.

Reynolds, S.J., and Spencer, J.E. (1993). Geologic Map of the western Harcuvar Mountains, La Paz County, west-central Arizona. *Arizona Geological Survey Open-File Report 93-3*, scale: 1:24,000.

Richard, S. M. (1988). Bedrock geology of the Harquahala Mountains, west-central Arizona: Mesozoic shear zones, cooling, and Tertiary unroofing (Doctoral dissertation). Santa Barbara, CA: University of California, Santa Barbara.

Richard, S.M., Fryxell, J.E., and Sutter, J.F. (1990). Tertiary structure and thermal history of the Harquahala and Buckskin Mountains, west central Arizona: Implications for denudation by a major detachment fault system. *Journal of Geophysical Research*, v. 95, no. B12, pp. 19973-19987.

Saleeby, J. (2003). Segmentation of the Laramide slab—Evidence from the southern Sierra Nevada region. *Geological Society of America Bulletin*, *115*(6), 655-668.

Salem, A.C., (2009). Mesozoic tectonics of the Maria Fold and Thrust Belt and McCoy Basin, southeastern California: An examination of polyphase deformation and synorogenic response (Doctoral dissertation). Alburquerque, NM: University of New Mexico.

Scott, R. J. (1995). *The geological development of the Buckskin-Rawhide metamorphic core complex, west-central Arizona* (Doctoral dissertation, Monash University).

Scott, R. J., & Lister, G. S. (1992). Detachment faults: Evidence for a low-angle origin. *Geology*, *20*(9), 833-836.

Scott, R. J., Foster, D. A., & Lister, G. S. (1998). Tectonic implications of rapid cooling of lower plate rocks from the Buckskin-Rawhide metamorphic core complex, west-central Arizona. *Geological Society of America Bulletin*, *110*(5), 588-614.

Selverstone, J., Axen, G.J., and Luther, A. (2012). Fault localization controlled by fluid infiltration into mylonites: Formation and strength of low-angle normal faults in the mid-crustal brittle-plastic transition. *Journal of Geophysical Research*, v. 117, doi:10.1029/2012JB009171

Seymour, N.M., Strickland, E.D., Singleton, J.S., Stockli, D.F., and Wong, M.S. (2018). Laramide subduction and metamorphism of the Orocopia Schist, northern Plomosa

Mountains, west-central Arizona: Insights from zircon U-Pb geochronology. *Geology*, v.46, p. 847–850.

Simpson, C. (1985). Deformation of granitic rocks across the brittle-ductile transition. *Journal of structural geology*, *7*(5), 503-511.

Singleton, J.S. (2011). Geologic map and cross sections of the Little Buckskin Mountains, La Paz County, west-central Arizona. *Arizona Geological Survey Contributed Map CM-11-B*, scale 1:12,000.

Singleton, J.S., Mosher, S. (2012). Mylonitization in the lower plate of the Buckskin-Rawhide detachment fault, west-central Arizona: Implications for the geometric evolution of metamorphic core complex. *Journal of Structural Geology*, v. 39, pp. 180-198.

Singleton, J.S., Stockli, D.F., Gans, P.B., and Prior, M.G. (2014). Timing, rate, and magnitude of slip on the Buckskin-Rawhide detachment fault, west-central Arizona. *Tectonics*, v. 33, pp. 1596–1615. doi:10.1002/2013TC003517

Singleton, J.S., (2015). The transition from large-magnitude extension to distributed dextral faulting in the Buckskin-Rawhide metamorphic core complex, west-central Arizona. *Tectonics*, v. 34, pp. 1685–1708. doi:10.1002/2014TC003786

Singleton, J.S., Wong, M.S., and Johnston, S.M. (2018). The role of calcite-rich metasedimentary mylonites in localizing detachment fault strain and influencing the structural evolution of the Buckskin-Rawhide metamorphic core complex, west-central Arizona. *Lithosphere*, v. 10, pp. 172–193.

Singleton, J.S., Seymour, N.M., Reynolds, S.J., Vomocil, T., and Wong, M.S. (2019). Distributed Neogene faulting across the western to central Arizona metamorphic core complex belt: Synextensional constriction and superposition of the Pacific-North America plate boundary on the southern Basin and Range. *Geosphere*, v. 15, p. 1409–1435, doi:10.1130/GES02036.1

Spencer, J.E., and Reynolds, S.J. (1990). Relationship between Mesozoic and Cenozoic tectonic features in west-central Arizona and adjacent southeastern California. *Journal of Geophysical Research*, v. 95, p. 539-555.

Spencer, J.E., and Reynolds, S.J. (1991). Tectonics of mid-Tertiary extension along a transect through west central Arizona. *Tectonics*, v. 10, pp. 1204-1221.

Spencer, J. E., Singleton, J. S., Strickland, E., Reynolds, S. J., Love, D., Foster, D. A., & Johnson, R. (2018). Geodynamics of Cenozoic extension along a transect across the Colorado River extensional corridor, southwestern USA. *Lithosphere*, v. 10(6), pp. 743-759.

Stipp, M., Stunitz, H., Heilbronner, R., Schmid, S.M. (2002a). The eastern Tonale fault zone: a 'natural laboratory' for crystal plastic deformation of quartz over a temperature range from 250 to 700°C. *Journal of Structural Geology*, v. 24, p. 1861-1884.

Stipp, M., Stünitz, H., Heilbronner, R. and Schmid, S.M., (2002b). Dynamic recrystallization of quartz: correlation between natural and experimental conditions. *Geological Society, London, Special Publications*, v. 200(1), pp. 171-190.

Strickland, E.D., Singleton, J.S., Haxel, G.B. (2018). Orocopia Schist in the northern Plomosa Mountains, west-central Arizona: A Laramide subduction complex exhumed in a Miocene metamorphic core complex. *Lithosphere*, v. 10, p. 723–742.

Thomas, J. B., Bruce Watson, E., Spear, F. S., Shemella, P. T., Nayak, S. K., & Lanzirotti, A. (2010). TitaniQ under pressure: the effect of pressure and temperature on the solubility of Ti in quartz. *Contributions to Mineralogy and Petrology*, *160*(5), 743-759.

Thomas, J. B., & Bruce Watson, E. (2012). Application of the Ti-in-quartz thermobarometer to rutile-free systems. Reply to: a comment on:'TitaniQ under pressure: the effect of pressure and temperature on the solubility of Ti in quartz' by Thomas et al. *Contributions to Mineralogy and Petrology*, *164*(2), 369-374.

Tullis, J., & Yund, R. A. (1991). Diffusion creep in feldspar aggregates: experimental evidence. *Journal of Structural Geology*, *13*(9), 987-1000.

Vermeesch, P. (2018). IsoplotR: A free and open toolbox for geochronology. *Geoscience Frontiers*, v. 9, doi:10.1016/j.gsf.2018.04.001

Wallace, P. J., Anderson Jr, A. T., & Davis, A. M. (1999). Gradients in H2O, CO2, and exsolved gas in a large-volume silicic magma system: Interpreting the record preserved in melt inclusions from the Bishop Tuff. *Journal of Geophysical Research: Solid Earth*, *104*(B9), 20097-20122.

Walsh, E.O., Wong, M.S., Singleton, J.S., Wrobel, A.J., Weiss, T., and Christensen, K. (2016). Evidence for polyphase exhumation of the Harcuvar metamorphic core complex, western Arizona. *Geological Society of America Abstracts with Programs*, v. 48 (7), doi:10.1130/abs/2016AM-287659

Wark, D. A., & Watson, E. B. (2006). TitaniQ: a titanium-in-quartz geothermometer. *Contributions to Mineralogy and Petrology*, *152*(6), 743-754.

Wells, M.L., Snee, L.W., and Blythe, A.E. (2000). Dating of major normal fault systems using thermochronology: An example from the Raft River detachment, Basin and Range, western United States. *Journal of Geophysical Research*, v. 105, p. 16,303-16,327.

Wells, M.L., Spell, T.L., and Grove, M. (2002). Late Cretaceous intrusion and extensional exhumation of the Cadiz Valley batholith, Iron Mountains, southeastern California. *Geological Society of America Abstracts with Programs*, v. 34, no. 6, p. 178.

Wells, M.L., Beyene, M.A., Spell, T.L., Kula, J.L., Miller, D.M., and Zanetti, K.A. (2005). The Pinto shear zone; a Laramide synconvergent extensional shear zone in the Mojave Desert region of southwestern United States. *Journal of Structural Geology*, v. 27, p. 1697-1720.

Wells, M. L., & Hoisch, T. D. (2008). The role of mantle delamination in widespread Late Cretaceous extension and magmatism in the Cordilleran orogen, western United States. *Geological Society of America Bulletin*, 120(5-6), 515-530.

Wernicke, B.P. (1981). Low angle normal faults in the Basin and Range province: Nappe tectonics in an extending orogen. *Nature*, v. 291, pp. 645-648.

Wernicke, B. (1985). Uniform-sense normal simple shear of the continental lithosphere. *Canadian Journal of Earth Sciences*, v. 22(1), pp. 108-125.

Wernicke, B., & Axen, G. J. (1988). On the role of isostasy in the evolution of normal fault systems. *Geology*, *16*(9), 848-851.

Wong, M.S., and Gans, P.B. (2008). Geologic, structural, and thermochronologic constraints on the tectonic evolution of the Sierra Mazatán core complex, Sonora, Mexico: New insights into metamorphic core complex formation. *Tectonics*, v. 27, TC4013, doi:10.1029/2007TC002173.

Wong, M.S., and Gans, P.B. (2009). Late Cretaceous-early Tertiary extension in the central Mojave metamorphic core complex: Implications for core complex formation and the Laramide orogeny. *Geological Society of America Abstracts with Programs*, v. 41, p. 588.

Wright, J. E., & Wooden, J. L. (1991). New Sr, Nd, and Pb isotopic data from plutons in the northern Great Basin: Implications for crustal structure and granite petrogenesis in the hinterland of the Sevier thrust belt. *Geology*, *19*(5), 457-460.

Wu, G., & Lavier, L. L. (2016). The effects of lower crustal strength and preexisting midcrustal shear zones on the formation of continental core complexes and low-angle normal faults. *Tectonics*, *35*(9), 2195-2214.

Zuza, A. V., Cao, W., Hinz, N. H., DesOrmeau, J. W., Odlum, M. L., & Stockli, D. F. (2019). Footwall rotation in a regional detachment fault system: Evidence for horizontal-axis rotational flow in the Miocene Searchlight pluton, NV. *Tectonics*, 38, 2506– 2539. doi:10.1029/2019TC005513

Tectonics

Supporting Information for

Late Cretaceous-early Paleogene extensional ancestry of the Harcuvar and Buckskin-Rawhide metamorphic core complexes, western Arizona

Martin S. Wong[1], John S. Singleton[2], Nikki M. Seymour[2*], Phillip B. Gans[3], and Alexander J. Wrobel[1†]

[1]Department of Earth and Environmental Geosciences, Colgate University, 13 Oak Drive, Hamilton, New York, 13346 USA.

[2] Department of Geosciences, Colorado State University, 1482 Campus Delivery, Fort Collins, Colorado 80523, USA.

[3]Department of Earth Science, University of California, Santa Barbara, California, 93105, USA

Contents of this file

Figures S1 to S2
Table S2

Additional Supporting Information (Files uploaded separately)

Table S1

Introduction

The supporting information includes detailed information about the sample locations and their structural and deformation characteristics (Table S1), grain size analysis (Figure S1), $^{40}Ar/^{39}Ar$ analyses (Table S2), and U-Pb geochronology (Figure S2).

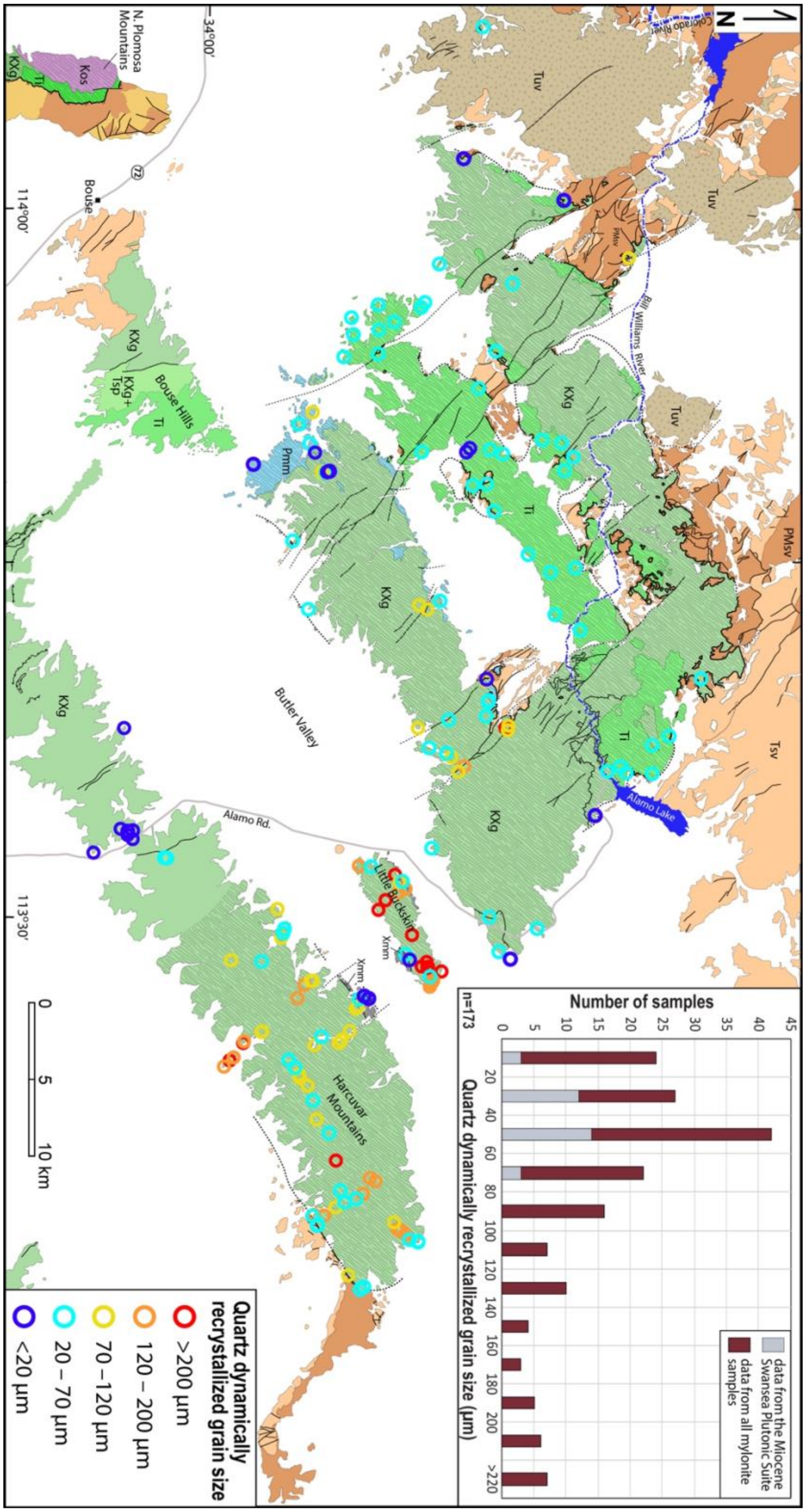

Quartz dynamically recrystallized grain size
>200 µm
120 – 200 µm
70 – 120 µm
20 – 70 µm
<20 µm
Number of samples
Quartz dynamically recrystallized grain size (µm)
data from the Miocene Swansea Plutonic Suite
data from all mylonite samples
n=173
Harcuvar Mountains
Little Buckskin
Butler Valley
Alamo Rd.
Alamo Lake
Bill Williams River
Colorado River
Bouse Hills
Bouse
N. Plomosa Mountains
34°00'
114°00'
113°30'
0
5
10 km
N
KXg
KXg+Tsp
Ti
Tuv
Tsv
PMsv
Pmm
Kos
Xmm

Figure S1. Map and associated histogram (upper-right insert) of measured average grain size for dynamically recrystallized quartz in mylonitic samples.

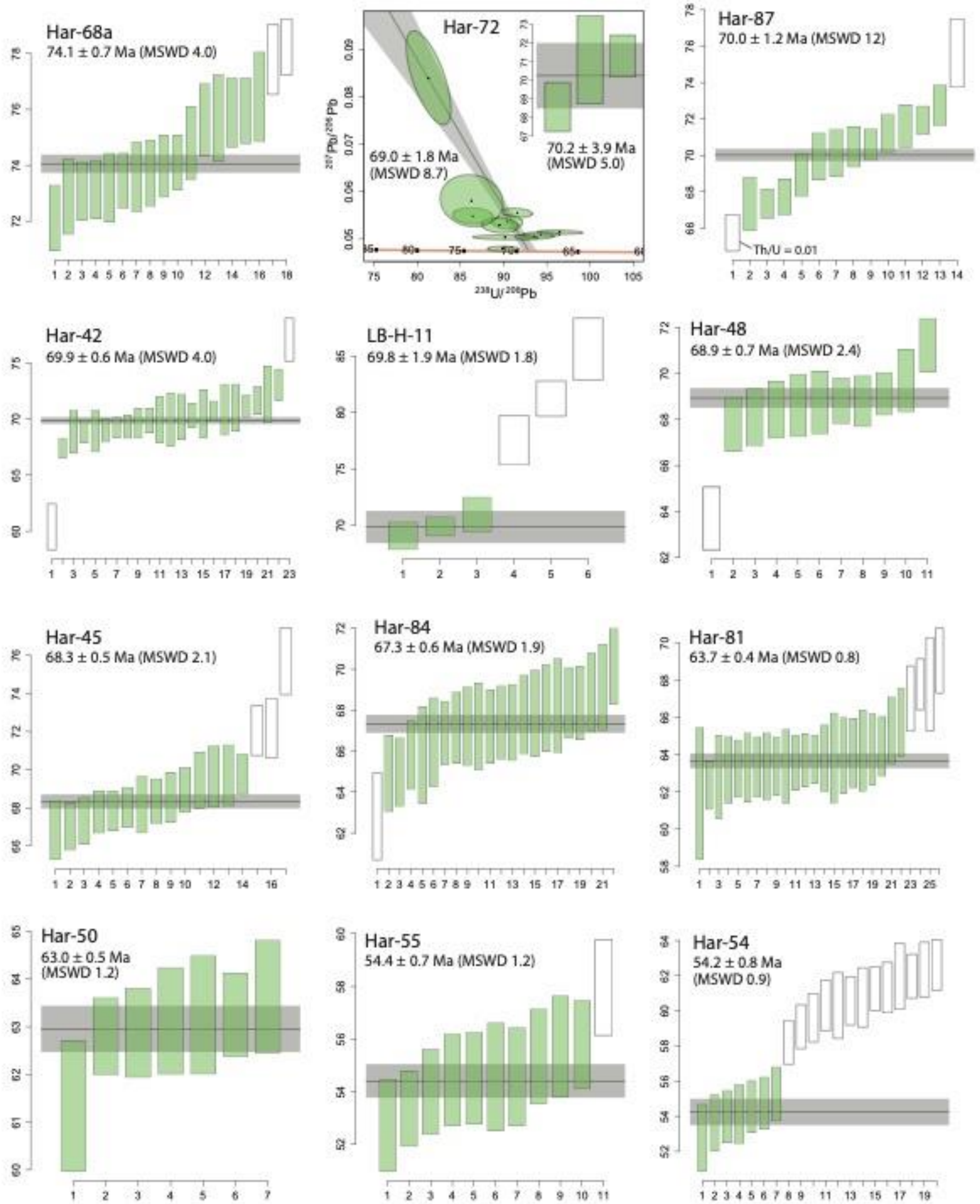

Figure S2. U-Pb geochronologic results showing the U^{238}/Pb^{206} spot ages for each dated sample and the calculated weighted mean age (horizontal gray bar). Spot analyses that yielded ages with >5% discordance are not shown here. The inverse concordia plot and lower intercept age for Har-72 is shown due to the higher fraction of discordant ages in that sample. Ages included in the weighted mean age calculation are filled green. Plots were generated using IsoplotR program (Vermeesch, 2018) and we allowed the program to reject outlier ages for weighted mean age calculations.

Table S1. Additional information on sample locations, kinematics, microstructures, deformation category and grain size (file attached separately).

Table S2. $^{40}Ar/^{39}Ar$ geochronologic analyses

$^{40}Ar/^{39}Ar$ analytical details

All $^{40}Ar/^{39}Ar$ analyses were conducted at the $^{40}Ar/^{39}Ar$ geochronology laboratory at UC Santa Barbara. Samples were step-heated in a Staudecher-type furnace and analyzed on a Nier source MAP 216 mass spectrometer. Samples were irradiated at the Oregon State University research reactor in the CLICIT facility and J-values were monitored using Taylor Creek Rhyolite sanidine using an assumed age of 27.92 Ma.

Hornblende data:

Sample: SB66-59 Har-71 hbl J=0.0041480

T	t	40(mol)	40/39	38/39	37/39	36/39	K/Ca	∑ 39Ar	40Ar*	Age (Ma)
700	14	1.6e-14	58.7182	5.5e-5	1.2997	0.1413	0.38	0.00251	0.289	122.7 ± 3.9
780	14	1.6e-14	42.3941	1.4e-3	1.3428	0.1127	0.36	0.00593	0.214	66.8 ± 2.8
850	14	2.1e-14	43.3787	4.3e-4	2.1768	0.1213	0.23	0.01026	0.174	55.6 ± 2.6
910	14	2.8e-14	30.9949	4.2e-4	3.9596	0.0750	0.12	0.01826	0.285	64.9 ± 1.3
950	14	2.3e-14	19.4007	1.4e-3	5.0907	0.0375	0.096	0.02885	0.429	61.3 ± 0.9
990	14	6.2e-14	16.0089	1.0e-3	4.3187	0.0273	0.11	0.06369	0.496	58.4 ± 0.4
1030	14	1.9e-13	16.3035	3.3e-4	3.9042	0.0268	0.13	0.16836	0.515	61.8 ± 0.2
1060	14	2.5e-13	12.7139	0.0e+0	3.6392	0.0138	0.13	0.34136	0.678	63.4 ± 0.2
1090	14	8.1e-14	11.0249	0.0e+0	3.6760	0.0075	0.13	0.40762	0.798	64.7 ± 0.2
1120	14	1.3e-13	12.9022	0.0e+0	3.7004	0.0137	0.13	0.50038	0.686	65.0 ± 0.2
1150	14	3.3e-13	12.3657	3.4e-4	3.6465	0.0122	0.13	0.73762	0.709	64.4 ± 0.1
1150	14	1.4e-13	11.5555	0.0e+0	3.6738	0.0097	0.13	0.84268	0.752	63.8 ± 0.2
1180	14	1.7e-13	11.0256	0.0e+0	3.6180	0.0082	0.14	0.97875	0.779	63.2 ± 0.2
1210	14	1.3e-14	11.1569	4.6e-4	4.2519	0.0093	0.12	0.98908	0.754	61.8 ± 0.7
1300	14	1.5e-14	12.0825	0.0e+0	5.6733	0.0123	0.086	1.00000	0.699	62.1 ± 0.7

Total fusion age, TFA= 63.65 ± 0.13 Ma (including J)
t = dwell time in minutes.
40(mol) = moles corrected for blank and reactor-produced 40.
Ratios are corrected for blanks, decay, and interference.
∑39Ar is cumulative, 40Ar* = rad fraction.

Sample: SB66-62 JS-H-12 hbl J=0.0041358

T	t	40(mol)	40/39	38/39	37/39	36/39	K/Ca	∑ 39Ar	40Ar*	Age (Ma)
700	14	1.3e-14	43.7451	0.0e+0	3.8877	0.0710	0.13	0.00647	0.521	162.4 ± 2.9
780	14	1.2e-14	43.1053	2.4e-3	1.7443	0.0822	0.28	0.01270	0.436	135.1 ± 3.1
850	14	7.6e-15	20.7441	1.0e-3	2.2319	0.0473	0.22	0.02063	0.326	49.8 ± 2.6
920	14	1.2e-14	13.1212	9.2e-4	5.1216	0.0223	0.096	0.04005	0.498	48.1 ± 1.0
970	14	3.2e-14	8.7524	1.9e-3	5.0953	0.0079	0.096	0.11840	0.732	47.2 ± 0.3
1000	14	5.5e-14	9.4668	1.7e-3	5.0213	0.0079	0.098	0.24437	0.754	52.5 ± 0.2
1030	14	4.5e-14	10.2254	1.2e-3	4.8338	0.0074	0.10	0.33949	0.786	59.0 ± 0.3

1050	14	2.7e-14	9.1387	1.5e-3	4.8144	0.0047	0.10	0.40281	0.848	56.9 ± 0.3
1070	14	4.1e-14	9.1804	1.2e-3	4.7671	0.0046	0.10	0.49920	0.851	57.4 ± 0.2
1100	14	2.2e-14	9.7373	9.0e-4	5.0140	0.0055	0.098	0.54880	0.832	59.5 ± 0.4
1120	14	4.5e-14	10.0400	1.8e-3	4.9329	0.0053	0.099	0.64620	0.843	62.0 ± 0.3
1140	14	1.0e-13	9.8635	1.2e-3	4.7843	0.0043	0.10	0.87559	0.872	63.0 ± 0.2
1160	14	3.9e-14	9.7253	1.2e-3	4.7942	0.0037	0.10	0.96256	0.888	63.3 ± 0.3
1190	14	1.2e-14	9.8423	2.5e-3	5.1334	0.0044	0.095	0.98817	0.868	62.6 ± 0.7
1230	14	3.7e-15	10.9731	5.4e-3	7.3783	0.0085	0.066	0.99552	0.771	62.0 ± 2.3
1300	14	2.7e-15	13.2248	4.3e-3	10.4957	0.0177	0.047	1.00000	0.604	58.6 ± 3.8

Total fusion age, TFA= 59.59 ± 0.14 Ma (including J)
40(mol) = moles corrected for blank and reactor-produced 40.
Ratios are corrected for blanks, decay, and interference.
∑39Ar is cumulative, 40Ar* = rad fraction.

Sample: SB66-74 Har-27 hbl J=0.0040847

T	t	40(mol)	40/39	38/39	37/39	36/39	K/Ca	∑ 39Ar	40Ar*	Age (Ma)
780	14	2.8e-14	51.9054	0.0e+0	1.0894	0.0791	0.45	0.00519	0.550	198.9 ± 1.6
850	14	8.6e-15	19.9746	1.3e-3	1.4579	0.0455	0.34	0.00931	0.327	47.5 ± 1.8
920	14	2.1e-14	12.3770	9.6e-4	2.9308	0.0151	0.17	0.02594	0.639	57.4 ± 0.5
970	14	8.8e-14	10.1942	5.3e-4	3.1407	0.0049	0.16	0.10852	0.859	63.4 ± 0.2
1000	14	1.5e-13	10.2480	4.3e-4	3.1060	0.0038	0.16	0.24506	0.891	66.1 ± 0.2
1030	14	2.3e-13	9.9482	6.4e-4	3.1141	0.0027	0.16	0.46998	0.920	66.2 ± 0.1
1050	14	1.5e-13	9.3120	7.1e-4	3.1190	0.0014	0.16	0.62750	0.956	64.4 ± 0.1
1070	14	8.3e-14	9.3429	2.9e-4	3.1284	0.0013	0.16	0.71243	0.959	64.9 ± 0.2
1100	14	2.6e-14	10.1003	3.5e-4	3.3362	0.0025	0.15	0.73716	0.928	67.7 ± 0.3
1120	14	2.9e-14	10.9114	9.9e-4	3.7016	0.0034	0.13	0.76270	0.907	71.5 ± 0.3
1140	14	9.3e-14	10.9450	4.4e-4	3.3816	0.0032	0.14	0.84456	0.914	72.3 ± 0.2
1160	14	1.5e-13	10.2330	4.3e-4	3.1380	0.0023	0.16	0.98137	0.934	69.1 ± 0.2
1190	14	1.3e-14	10.2909	5.5e-4	3.2500	0.0033	0.15	0.99371	0.905	67.3 ± 0.5
1300	14	6.8e-15	10.3211	2.6e-3	3.9992	0.0047	0.12	1.00000	0.864	64.6 ± 0.9

Total fusion age, TFA= 67.13 ± 0.14 Ma (including J)
t = dwell time in minutes.
40(mol) = moles corrected for blank and reactor-produced 40.
Ratios are corrected for blanks, decay, and interference.
∑39Ar is cumulative, 40Ar* = rad fraction.

Sample: SB66-66 JS-H-24 hbl J=0.0041141

T	t	40(mol)	40/39	38/39	37/39	36/39	K/Ca	∑ 39Ar	40Ar*	Age (Ma)
780	14	1.4e-14	29.3337	0.0e+0	1.0423	0.0419	0.47	0.01050	0.578	121.6 ± 1.6
850	14	3.7e-15	11.8976	0.0e+0	1.8673	0.0250	0.26	0.01761	0.380	33.3 ± 2.0
920	14	5.3e-15	12.0297	0.0e+0	6.8682	0.0244	0.071	0.02758	0.400	35.3 ± 1.3
970	14	7.2e-15	8.2807	1.3e-4	7.2366	0.0128	0.068	0.04743	0.545	33.2 ± 0.8
1000	14	1.5e-14	6.9012	8.2e-4	5.8825	0.0076	0.083	0.09774	0.676	34.3 ± 0.3
1030	14	3.6e-14	5.8219	4.2e-4	5.6819	0.0053	0.086	0.23644	0.730	31.3 ± 0.1
1050	14	2.9e-14	6.1050	1.4e-4	5.2720	0.0033	0.093	0.34326	0.843	37.8 ± 0.2
1070	14	2.5e-14	7.6320	2.5e-4	5.1047	0.0034	0.096	0.41900	0.867	48.4 ± 0.2
1100	14	1.9e-14	7.2805	5.7e-5	5.3079	0.0047	0.092	0.47936	0.808	43.1 ± 0.3
1120	14	2.3e-14	7.6280	1.8e-7	5.4532	0.0052	0.090	0.54782	0.799	44.7 ± 0.3
1140	14	3.7e-14	7.6985	2.9e-4	5.3580	0.0046	0.091	0.65834	0.822	46.4 ± 0.2
1160	14	6.3e-14	7.0909	5.2e-4	5.2298	0.0031	0.094	0.86163	0.871	45.3 ± 0.1
1190	14	3.3e-14	6.8820	4.5e-4	5.2251	0.0027	0.094	0.97078	0.883	44.5 ± 0.2
1300	14	9.3e-15	7.2023	0.0e+0	5.6205	0.0042	0.087	1.00000	0.829	43.8 ± 0.5

Total fusion age, TFA= 42.45 ± 0.11 Ma (including J)
t = dwell time in minutes.
40(mol) = moles corrected for blank and reactor-produced 40.
Ratios are corrected for blanks, decay, and interference.
∑39Ar is cumulative, 40Ar* = rad fraction.

Sample: SB66-68 JS-H-32 hbl J=0.0041075

T	t	40(mol)	40/39	38/39	37/39	36/39	K/Ca	∑ 39Ar	40Ar*	Age (Ma)
800	14	1.4e-14	15.131	0.0e+0	1.3731	0.0215	0.36	0.02348	0.580	63.9 ± 0.8
880	14	4.7e-15	6.9724	0.0e+0	2.6303	0.0127	0.19	0.04063	0.463	23.8 ± 0.8
950	14	8.9e-15	8.3698	2.1e-3	8.1244	0.0128	0.060	0.06770	0.549	33.7 ± 0.6
990	14	3.9e-14	6.8105	2.3e-3	7.1755	0.0075	0.068	0.21184	0.676	33.8 ± 0.2
1030	14	6.8e-14	6.7225	1.7e-3	6.0340	0.0055	0.081	0.46862	0.760	37.5 ± 0.1
1060	14	6.2e-15	7.3869	2.2e-3	5.8005	0.0074	0.084	0.48984	0.705	38.2 ± 0.8
1100	14	1.8e-14	7.5828	6.5e-4	5.5737	0.0056	0.088	0.54891	0.780	43.3 ± 0.3
1130	14	2.7e-14	7.9456	2.5e-3	5.6789	0.0057	0.086	0.63610	0.787	45.8 ± 0.2
1160	14	7.5e-14	7.3301	2.0e-3	5.3863	0.0037	0.091	0.89607	0.851	45.7 ± 0.1
1190	14	1.9e-14	7.1893	1.5e-3	5.4388	0.0039	0.090	0.96385	0.839	44.2 ± 0.2
1300	14	1.0e-14	7.2636	2.0e-3	5.8460	0.0046	0.084	1.00000	0.813	43.2 ± 0.4

Total fusion age, TFA= 41.11 ± 0.10 Ma (including J)
t = dwell time in minutes.
40(mol) = moles corrected for blank and reactor-produced 40.
Ratios are corrected for blanks, decay, and interference.
∑39Ar is cumulative, 40Ar* = rad fraction.

Sample: SB64=162 HAR-43 Hbl J=0.0037467

T	t	40(mol)	40/39	38/39	37/39	36/39	K/Ca	∑ 39Ar	40Ar*	Age (Ma)
700	14	1.5e-14	300.099	1.5e-2	3.5066	0.2696	0.14	0.00096	0.735	1086.1 ± 12.9
800	14	1.2e-14	110.978	5.0e-3	1.6420	0.0724	0.30	0.00291	0.807	522.0 ± 4.1
860	14	3.5e-15	36.3059	0.0e+0	1.5014	0.0416	0.33	0.00471	0.661	155.4 ± 3.4
900	14	1.7e-15	20.4857	2.4e-3	2.7863	0.0364	0.18	0.00624	0.475	64.5 ± 4.1
940	14	1.3e-15	16.3865	1.2e-3	2.0255	0.0309	0.24	0.00769	0.442	48.3 ± 3.8
980	14	1.5e-15	13.2861	2.5e-3	2.7871	0.0229	0.18	0.00977	0.490	43.4 ± 3.0
1020	14	2.6e-15	11.2722	2.7e-3	3.3195	0.0164	0.15	0.01413	0.569	42.8 ± 1.5
1060	14	7.6e-15	8.1162	1.5e-3	4.3069	0.0086	0.11	0.03167	0.687	37.3 ± 0.5
1100	14	2.5e-14	6.8449	1.5e-3	3.9192	0.0041	0.13	0.09921	0.821	37.6 ± 0.2
1140	14	6.4e-14	6.5762	1.6e-3	3.8082	0.0025	0.13	0.28112	0.887	39.0 ± 0.1
1180	14	5.6e-14	6.8135	1.4e-3	3.6539	0.0015	0.13	0.43519	0.933	42.5 ± 0.1
1230	14	6.2e-14	6.9478	1.4e-3	3.6987	0.0017	0.13	0.60107	0.927	43.0 ± 0.1
1290	14	1.4e-13	6.8175	1.1e-3	3.6563	0.0011	0.13	0.98981	0.954	43.4 ± 0.1
1350	14	2.2e-15	7.8790	4.4e-3	4.5909	0.0045	0.11	0.99504	0.831	43.7 ± 1.3
1450	14	2.4e-15	9.1902	0.0e+0	6.0951	0.0076	0.08	1.00000	0.755	46.3 ± 1.4

Total fusion age, TFA= 44.58 ± 0.09 Ma (including J)
Weighted mean plateau age, WMPA= 43.30 ± 0.10 Ma (including J)
Inverse isochron age =43.72 ± 0.46 Ma. (MSWD =3.91; 40Ar/36Ar=244.9 ± 52.4)
Steps used: 1230, 1290, 1350, (12–14/15 or 56% ∑ 39Ar
t = dwell time in minutes.
40(mol) = moles corrected for blank and reactor-produced 40.
Ratios are corrected for blanks, decay, and interference.
∑39Ar is cumulative, 40Ar* = rad fraction.

Biotite data:

Sample: SB64-166 Har-68A Bio J=0.0037117

T	t	40(mol)	40/39	38/39	37/39	36/39	K/Ca	∑ 39Ar	40Ar*	Age (Ma)
650	14	2.3e-15	34.8697	1.3e-2	1.1011	0.1164	0.44	0.00345	0.014	3.1 ± 5.5
730	14	3.9e-15	14.2670	1.8e-3	0.2372	0.0247	2.1	0.01788	0.488	46.0 ± 1.1
800	14	1.4e-14	10.7635	0.0e+0	0.0663	0.0061	7.4	0.08695	0.832	59.0 ± 0.3
850	14	2.4e-14	10.3321	0.0e+0	0.0239	0.0023	21	0.20710	0.936	63.6 ± 0.2
900	14	2.8e-14	10.1879	0.0e+0	0.0165	0.0012	30	0.35203	0.966	64.7 ± 0.2
950	14	1.4e-14	10.3452	0.0e+0	0.0440	0.0018	11	0.42355	0.949	64.6 ± 0.2
1000	14	9.6e-15	10.5074	0.0e+0	0.1300	0.0023	3.8	0.47169	0.936	64.7 ± 0.3
1050	14	1.2e-14	10.6228	0.0e+0	0.3523	0.0027	1.4	0.53167	0.926	64.7 ± 0.3
1100	14	1.9e-14	10.7732	0.0e+0	0.6253	0.0021	0.78	0.62581	0.942	66.7 ± 0.2
1150	14	5.0e-14	10.5889	4.5e-4	1.1273	0.0014	0.43	0.87717	0.961	66.9 ± 0.2

1210	14	2.1e-14	10.3976	0.0e+0	0.4510	0.0017	1.1	0.98636	0.951	65.0 ± 0.2
1270	14	3.0e-15	11.5861	0.0e+0	1.7218	0.0062	0.28	1.00000	0.841	64.1 ± 0.9

Total fusion age, TFA= 64.46 ± 0.12 Ma (including J)
t = dwell time in minutes.
40(mol) = moles corrected for blank and reactor-produced 40.
Ratios are corrected for blanks, decay, and interference.
∑39Ar is cumulative, 40Ar* = rad fraction.

Sample: Har-102 bio J=0.0032260

T	t	40(mol)	40/39	38/39	37/39	36/39	K/Ca	∑ 39Ar	40Ar*	Age (Ma)
680	12	3.4e-14	8.7666	0.0e+0	0.0087	0.0029	56	0.18009	0.901	45.4 ± 0.1
760	12	5.8e-14	8.4019	0.0e+0	0.0080	0.0009	61	0.50251	0.967	46.7 ± 0.1
840	12	2.2e-14	8.3841	0.0e+0	0.0276	0.0014	18	0.62535	0.950	45.8 ± 0.2
920	12	1.4e-14	8.5047	0.0e+0	0.0202	0.0021	24	0.70295	0.928	45.4 ± 0.2
1000	12	1.5e-14	8.6231	0.0e+0	0.0004	0.0016	1096	0.78492	0.944	46.7 ± 0.2
1080	12	3.2e-14	8.5979	0.0e+0	0.0082	0.0011	60	0.95661	0.963	47.6 ± 0.2
1160	12	7.7e-15	8.9832	0.0e+0	0.0140	0.0021	35	0.99673	0.930	48.0 ± 0.3
1250	12	9.5e-16	13.5178	6.0e-4	0.3267	0.0218	1.5	1.00000	0.524	40.8 ± 4.2

Total fusion age, TFA= 46.43 ± 0.12 Ma (including J)
t = dwell time in minutes.
40(mol) = moles corrected for blank and reactor-produced 40.
Ratios are corrected for blanks, decay, and interference.
∑39Ar is cumulative, 40Ar* = rad fraction.

Sample: SB61-42 Har-26 bio J=0.0033127

T	t	40(mol)	40/39	38/39	37/39	36/39	K/Ca	∑ 39Ar	40Ar*	Age (Ma)
600	12	6.3e-14	6.7382	1.1e-4	0.0300	0.0132	16	0.06727	0.419	16.8 ± 0.1
660	12	7.3e-14	5.9000	0.0e+0	0.0125	0.0051	39	0.15622	0.746	26.1 ± 0.1
700	12	7.9e-14	5.8996	0.0e+0	0.0085	0.0030	58	0.25250	0.850	29.7 ± 0.1
740	12	9.2e-14	5.8820	0.0e+0	0.0074	0.0020	67	0.36515	0.898	31.3 ± 0.1
780	12	6.2e-14	5.9260	0.0e+0	0.0076	0.0019	65	0.44012	0.905	31.8 ± 0.1
830	12	4.5e-14	6.1454	0.0e+0	0.0106	0.0027	46	0.49303	0.872	31.7 ± 0.1
890	12	5.3e-14	6.1861	0.0e+0	0.0155	0.0030	32	0.55542	0.859	31.5 ± 0.1
950	12	6.0e-14	6.3510	0.0e+0	0.0218	0.0041	23	0.62373	0.808	30.4 ± 0.1
980	12	5.4e-14	6.0664	0.0e+0	0.0126	0.0033	39	0.68740	0.841	30.2 ± 0.1
1010	12	6.1e-14	5.8608	0.0e+0	0.0109	0.0025	45	0.76289	0.876	30.4 ± 0.1
1040	12	7.4e-14	5.8336	0.0e+0	0.0112	0.0019	44	0.85406	0.903	31.2 ± 0.1
1070	12	6.7e-14	5.9455	0.0e+0	0.0241	0.0017	20	0.93505	0.915	32.2 ± 0.1
1120	12	4.1e-14	6.0486	0.0e+0	0.1076	0.0014	4.6	0.98391	0.931	33.3 ± 0.1
1200	12	1.4e-14	6.4271	0.0e+0	0.3173	0.0020	1.5	1.00000	0.909	34.6 ± 0.2

Total fusion age, TFA= 29.81 ± 0.08 Ma (including J)
t = dwell time in minutes.
40(mol) = moles corrected for blank and reactor-produced 40.
Ratios are corrected for blanks, decay, and interference.
∑39Ar is cumulative, 40Ar* = rad fraction.

Sample: Har-103B bio J=0.0032260

T	t	40(mol)	40/39	38/39	37/39	36/39	K/Ca	∑ 39Ar	40Ar*	Age (Ma)
680	12	2.2e-14	6.3773	0.0e+0	0.0179	0.0060	27	0.23117	0.721	26.6 ± 0.1
760	12	1.9e-14	6.0537	0.0e+0	0.0041	0.0035	119	0.44072	0.828	28.9 ± 0.1
840	12	8.5e-15	6.5682	0.0e+0	0.0559	0.0057	8.8	0.52583	0.744	28.2 ± 0.2
920	12	9.5e-15	6.6485	0.0e+0	0.0790	0.0065	6.2	0.62037	0.709	27.2 ± 0.2
1000	12	1.6e-14	6.7791	0.0e+0	0.1196	0.0054	4.1	0.77627	0.763	29.9 ± 0.2
1080	12	1.7e-14	6.3157	0.0e+0	0.0833	0.0035	5.9	0.95559	0.836	30.5 ± 0.1
1160	12	4.0e-15	7.2640	0.0e+0	0.1619	0.0053	3.0	0.99219	0.785	32.9 ± 0.5
1250	12	1.3e-15	10.8130	0.0e+0	0.3789	0.0140	1.3	1.00000	0.618	38.5 ± 2.3

Total fusion age, TFA= 28.81 ± 0.09 Ma (including J)
t = dwell time in minutes.
40(mol) = moles corrected for blank and reactor-produced 40.

Ratios are corrected for blanks, decay, and interference.
∑39Ar is cumulative, 40Ar* = rad fraction.

Sample: Har-105 bio J=0.0032260

T	t	40(mol)	40/39	38/39	37/39	36/39	K/Ca	∑ 39Ar	40Ar*	Age (Ma)
670	12	1.9e-14	4.1147	0.0e+0	0.0209	0.0039	23	0.15363	0.719	17.1 ± 0.1
750	12	2.5e-14	3.3895	0.0e+0	0.0166	0.0011	30	0.40256	0.905	17.8 ± 0.1
870	12	1.2e-14	3.7599	0.0e+0	0.0397	0.0024	12	0.50826	0.813	17.7 ± 0.1
980	12	1.5e-14	4.3154	0.0e+0	0.2169	0.0037	2.3	0.62525	0.746	18.6 ± 0.1
1070	12	2.6e-14	3.7496	0.0e+0	0.1045	0.0016	4.7	0.86262	0.870	18.9 ± 0.1
1250	12	1.4e-14	3.5134	0.0e+0	0.0947	0.0013	5.2	1.00000	0.887	18.0 ± 0.1

Total fusion age, TFA= 18.07 ± 0.05 Ma (including J)
t = dwell time in minutes.
40(mol) = moles corrected for blank and reactor-produced 40.
Ratios are corrected for blanks, decay, and interference.
∑39Ar is cumulative, 40Ar* = rad fraction.

Sample: Har-100 bio J=0.0032260

T	t	40(mol)	40/39	38/39	37/39	36/39	K/Ca	∑ 39Ar	40Ar*	Age (Ma)
670	12	2.3e-14	4.7319	0.0e+0	0.0274	0.0058	18	0.11427	0.636	17.4 ± 0.1
750	12	3.2e-14	3.7562	0.0e+0	0.0138	0.0021	35	0.31565	0.837	18.2 ± 0.1
870	12	2.1e-14	4.6033	0.0e+0	0.0262	0.0050	19	0.42531	0.681	18.1 ± 0.1
980	12	2.4e-14	4.1623	0.0e+0	0.0387	0.0036	13	0.56149	0.747	18.0 ± 0.1
1070	12	4.1e-14	3.5849	0.0e+0	0.0130	0.0015	38	0.83305	0.876	18.2 ± 0.1
1250	12	2.5e-14	3.5839	0.0e+0	0.0470	0.0012	10	1.00000	0.902	18.7 ± 0.1

Total fusion age, TFA= 18.16 ± 0.05 Ma (including J)
t = dwell time in minutes.
40(mol) = moles corrected for blank and reactor-produced 40.
Ratios are corrected for blanks, decay, and interference.
∑39Ar is cumulative, 40Ar* = rad fraction.

Sample: Har-83 bio J=0.0032260

T	t	40(mol)	40/39	38/39	37/39	36/39	K/Ca	∑ 39Ar	40Ar*	Age (Ma)
670	12	1.4e-14	3.3529	0.0e+0	0.0284	0.0018	17	0.10312	0.845	16.4 ± 0.1
750	12	2.4e-14	3.0318	0.0e+0	0.0262	0.0006	19	0.29205	0.939	16.5 ± 0.1
870	12	1.4e-14	3.1126	0.0e+0	0.0400	0.0008	12	0.39776	0.920	16.6 ± 0.1
980	12	1.5e-14	3.2091	0.0e+0	0.1083	0.0010	4.5	0.50854	0.906	16.8 ± 0.1
1070	12	3.2e-14	3.0083	0.0e+0	0.0239	0.0005	21	0.76121	0.949	16.5 ± 0.1
1250	12	3.0e-14	3.0365	0.0e+0	0.0616	0.0005	8.0	1.00000	0.953	16.8 ± 0.1

Total fusion age, TFA= 16.61 ± 0.05 Ma (including J)
t = dwell time in minutes.
40(mol) = moles corrected for blank and reactor-produced 40.
Ratios are corrected for blanks, decay, and interference.
∑39Ar is cumulative, 40Ar* = rad fraction.

Sample: Har-80 bio J=0.0032260

T	t	40(mol)	40/39	38/39	37/39	36/39	K/Ca	∑ 39Ar	40Ar*	Age (Ma)
670	12	2.0e-14	3.8073	0.0e+0	0.0236	0.0035	21	0.09607	0.732	16.1 ± 0.1
750	12	2.6e-14	3.1483	0.0e+0	0.0240	0.0011	20	0.24886	0.901	16.4 ± 0.1
870	12	1.6e-14	3.4269	0.0e+0	0.0724	0.0020	6.8	0.33341	0.824	16.4 ± 0.1
980	12	1.9e-14	3.3805	0.0e+0	0.1641	0.0018	3.0	0.43713	0.841	16.5 ± 0.1
1070	12	4.2e-14	3.1169	0.0e+0	0.0139	0.0010	35	0.68581	0.901	16.3 ± 0.1
1250	12	5.3e-14	3.0694	0.0e+0	0.0368	0.0008	13	1.00000	0.919	16.3 ± 0.0

Total fusion age, TFA= 16.33 ± 0.04 Ma (including J)
t = dwell time in minutes.
40(mol) = moles corrected for blank and reactor-produced 40.
Ratios are corrected for blanks, decay, and interference.
∑39Ar is cumulative, 40Ar* = rad fraction.

Sample: Har-112 bio J=0.0032260

T	t	40(mol)	40/39	38/39	37/39	36/39	K/Ca	∑ 39Ar	40Ar*	Age (Ma)
670	12	2.6e-14	5.5718	0.0e+0	0.0231	0.0113	21	0.12688	0.398	12.9 ± 0.1
750	12	2.7e-14	4.0702	0.0e+0	0.0214	0.0051	23	0.30703	0.629	14.8 ± 0.1
870	12	2.7e-14	6.6346	0.0e+0	0.0561	0.0144	8.7	0.41718	0.357	13.7 ± 0.1
980	12	2.6e-14	5.6117	0.0e+0	0.1449	0.0109	3.4	0.54662	0.425	13.8 ± 0.1
1070	12	2.8e-14	3.9728	0.0e+0	0.0609	0.0050	8.0	0.74265	0.625	14.4 ± 0.1
1250	12	3.1e-14	3.3070	0.0e+0	0.0707	0.0023	6.9	1.00000	0.791	15.2 ± 0.1

Total fusion age, TFA= 14.33 ± 0.05 Ma (including J)
Weighted mean plateau age, WMPA= 14.72 ± 0.05 Ma (including J)
Inverse isochron age =15.34 ± 0.21 Ma. (MSWD =15.49; 40Ar/36Ar=273.6 ± 5.5)
Steps used: 750, 870, 980, 1070, 1250, (2–6/6 or 87% ∑ 39Ar
t = dwell time in minutes.
40(mol) = moles corrected for blank and reactor-produced 40.
Ratios are corrected for blanks, decay, and interference.
∑39Ar is cumulative, 40Ar* = rad fraction.

Table S1. Sample locations, kinematics, microstructures, deformation category and grain size

Harcuvar samples

Sample	UTM Easting (m)*	UTM Northing (m)	Sample description	Sense of shear	Qtz recrystalliz.	Quartz grain size analyses: # grains	median diameter (μ)	geometric mean (μ)	stdev	Feldspar deformation	additional microstructures, comments	Def. conditions category**
Har-1	290605	3777739	granite mylonite	top-NE	SGR, GBM	69	64.8	58.9	33.8	BLG, SGR	minor epi, ~3% biotite, no chlorite, obl qtz GSPO, subtle C' s.b.	3
Har-2	290605	3777739	quartzo-feldspathic ultramylonite	top-NE	SGR+GBM	57	65.5	61.2	45.9	BLG, SGR	ultramylonite; wide range of quartz grain sizes (probably from SGR overprint of GBM)	3
Har-3	290596	3777809	2-mica granite mylonite/protomylonite	top-NE	GBM+SGR					SGR, fracturing	subtle top-NE sense of shear from feldspar sigma-clasts; sample forqtz EBSD	3
Har-4	290445	3777259	mylonitic quartzo-feldspathic gneiss	top-NE	SGR+GBM	63	64.8	62	32.1	SGR	wide range of qtz grain sizes, qtz prism <a> slip inferred to be dominant, subtle biot-lined C' s.b. & obl qtz GSPO, pervasive feldspar rexstallization	3
Har-6	290286	3776882	amphibolite mylonite	top-NE	SGR+GBM					SGR+BLG	syn-kin hbl along C' shears	3
Har-8	289814	3776685	moderately-strained granite	unclear	GBM	63	154.1	162.8	164.6	SGR	~1% biot, ~1% chl after biot	4
Har-9	289814	3776685	biotite-quartz amphibolite	top-NE	minor SGR+GBM					minor SGR	C' shear bands with some feldspar BLG, synkin biot	3
Har-11	289733	3776473	weakly-strained granite sill	top-NE	GBM	53	126.7	125.8	93.1	SGR, myrm	subtle C' s.b., ~5% biot with no chlorite	4
Har-13	288960	3776088	weakly-strained granite	top-NE	GBM, SGR	59	70.3	75.2	40.5	SGR+BLG	top-NE C' s.b. with biotite and feldspar BLG, ~5% biot, minor chl	3
Har-16	269983	3769636	granite mylonite	top-NE	SGR	51	57.7	60.8	33	fracturing, BLG	synkin epi+biot, C' s.b. with biot & feldspar BLG, subtle obl qtz GSPO	2
Har-17	270283	3769527	high-strain granite mylonite	top-NE	SGR	53	38.9	35.9	17.7	BLG+SGR	C' s.b., qtz obl GSPO, abundant titanite with asym biotite tails, abundant feldspar rexstalliz.	3
Har-17a	270283	3769527	high-strain granite mylonite	top-NE	SGR	50	41.1	42.8	16.6	SGR+BLG	S-C fabric, obl qtz GSPO, ~15% fine-grained biot	3
Har-19	270541	3769405	high-strain granite mylonite	coaxial	SGR+GBM	54	89.8	91.9	47.9	SGR+BLG, minor fracturing	conjugate shear bands - no bulk asymmetry	3
Har-22	250306	3747693	quartz vein with slicks	top-NE	SGR						spectacular obl qtz GSPO, muscovite-fish, C-planes lined by muscovite	2
Har-28	262289	3762730	muscovite schist	top-NE	SGR						muscovite fish & biotite-lined C' s.b., localy qtz obl GSPO	2
Har-36	273422	3771354	granite mylonite	top-NE	SGR+GBM	58	101.7	96.1	43.9	SGR, BLG, minor fracturing	pervasive feldspar recrystallization, subtle obl qtz GSPO, <3% fine-grained biot	3 or 4
Har-37	273409	3771284	low-strain granite	top-NE	GBM+SGR	202	96.5	100	63	SGR	sericitized feldspar, synkin epi & titanite, subtle qtz obl GSPO	4
Har-38	273668	3770836	granite sill	top-NE	GBM	101	172.1	172.4	114.9	SGR	ultramylonite, abundant epi and associated titanite	4
Har-40	274121	3770603	moderately-strained granite	top-NE?	GBM					SGR	pervasive feldspar recrystallization, subtle C' s.b. and sigma clasts	4
Har-41	274524	3770359	weakly-strained granite	top-NE	GBM	77	149.4	151.1	79.2	SGR	obl GSPO in recrystallized feldspar, <2% biot with some chl after biot, serICititization of feldspar common	4
SJ-1	289626	3776345	granite mylonite	top-NE	SGR					BLG	C-planes & C' s.b. with BLG recrystalliz., ~10% biot+chl, obl qtz GSPO	2
SJ-5	271171	3768698	high-strain gneiss with narrow band of lower-T deformation w/060 lineation	top-NE	SGR, GBM?					BLG+SGR	quartz SGR is incomplete, subtle obl GSPO in qtz & feldspar, ~10% biot+chl	3
SJ-6	271529	3768297	granite mylonite	top-NE	GBM, SGR					SGR	subtle obl qtz GSPO, ~5% biot+chl	4
SJ-7	271529	3768297	quartzo-feldspathic mylonite	top-NE	SGR+GBM					SGR+BLG	C' s.b., subtle obl qtz GSPO, abundant epi, chl, some garnet; GS overprint on amphib fabric	3
SJ-8	272069	3768086	granite protomylonite w/ N-S lineation	top-N	SGR+GBM	59	61	59.7	29.6	minor BLG	subtle C' s.b., local qtz obl GSPO, discontinuous qtz lenses, incomplete quartz SGR	2
SJ-16	276758	3773713	granite mylonite with shear bands	top-NE	GBM+SGR	53	97.8	96.3	29.8	SGR	C' s.b. with biot, local qtz obl GSPO, ~10% biot, no chl	4
SJ-17	277331	3773162	granite protomylonite	top-NE	SGR, GBM	54	79.6	78	34.9	SGR+BLG	incomplete qtz SGR, C' s.b., ~10% biot, no chl	3
SJ-18	277524	3772973	granite with high-strain shear zone	coaxial	SGR+GBM	73	82.7	79.7	33	SGR+BLG	~10% biot, minor chl; symmetric conjugate shear bands	3
SJ-19	277867	3772247	low-strain granite	top-NE	GBM, SGR					SGR	(thin section is too thick, hard to see microstructures clearly), C' s.b., local obl qtz GSPO, pervasive feldspar rxstalliz., some large qtz grains lack SGR overprint	4
SJ-21	277084	3771866	granite ultramylonite	top-NE	GBM+SGR	61	67	63.6	25.6	SGR	~10% biot, no chl, abundant feldspar SGR, C' s.b. and obl biot laths	4
7-H1	264697	3757318	protomylonitic 2-mica granite	top-NE	BLG II	60	10.1	10.3	4.4	fracturing	crudely developed S-C-C' fabric, qtz ribbons with relatively little recrystallization	1
H-3	263593	3759560	leucogranite S-C-C' mylonite	top-SW	BLG II	75	8.7	8.6	2.5	cataclasis, no recrystalliz.	S-C-C' fabric, obl qtz GSPO, ~8% muscov+biot (locally chloritized), feldspar sericitization	1
H-5	263197	3759125	granite mylonite	top-NE	SGR, BLG	55	7.9	8	2.1	chem breakdown+BLG+cataclasis	top-NE asym folds, obl qtz GSPO, fractured epi porphyroclasts (~5%), ~20% fine-grained white mica	1
H-6	263131	3759212	granite with gneissic fabric								NOT mylonitic; coarse-grained, interlocking quartz, feldspar, biotite, epidote, local zones of quartz subgrain development & BLG	
H-7C	263351	3759584	gneiss								gneissic fabric with brittle overprint of feldspar, white mica development from feldspar, qtz blobs/pods show BLG II	
H-7D	263351	3759584	mylonitic gneiss	top-NE	SGR+BLG	77	13.8	13.7	4.5	fracturing, some chemical breakdown	S-C-C' fabric, qtz obl GSPO, some qtz p.clasts and ribbons without recryst., ~12% muscov (compared to ~5% in nonmylon protolith)	1
H-8	263340	3759897	quartzo-feldspathic mylonite	top-NE	SGR, BLG	209	11	10.6	4.5	fracturing & cataclasis, BLG	quartz & feldspar obl GSPO, abundant synkin epi & biot, C' s.b., some ribboned qtz porphyroclasts lacking pervasive recrystallization	1

H-10	263877	3759932	quartzo-feldspathic mylonite	top-NE	BLG+SGR	227	6.9	6.8	3.9	cataclasis, chem breakdown (no BLG)	obl qtz GSPO, some qtz porphyroclasts; qtz ribbons without recrystalliz common, brittle-ductile C' s.b.	1
H-22	266087	3759957	shear band cutting gneissic fabric	top-NE	SGR					fracturing, chemical breakdown	abundant fine-grained epi & biot/muscov matrix, rounded feldspar porphyroclasts likely derived from fracturing, local S-C fabric	2
H-33	288225	3772485	leucogranite mylonite	top-NE	GBM, minor SGR	65	89.6	90.3	51.3	SGR+BLG, myrmek.	~3% biot, subtle qtz obl GSPO, 1 C' s.b., some very large qtz grains lacking SGR	4
H-34	289373	3771258	meta-arkose? mylonite	top-NE	SGR	58	31.3	32.1	9.3	pervasive SGR?	~10% f-grained chl, ~5% opaques, ~5% f-gr epi, ~40% qtz, ~40% grungy feldspar - mixed with qtz, obl qtz GSPO	2
H-35	289303	3771314	granitoid ultramylonite	top-NE	SGR, GBM	104	46.2	45.7	22.1	pervasive feldspar SGR	~5% f-gr epi, ~5-10% mica (mostly chl after biot)	3
H-36	292673	3773185	granitoid (?) ultramylonite (meta-arkose?)	top-NE	SGR+GBM	51	107.6	102.8	38.6	SGR?	grungy feldspar - difficult to evaluate def mechanisms, particularly given potential metased protolith, all mica is chl, subtle qtz obl GSPO	3
H-37A	290084	3776991	shear band cutting amphibolite	top-NE	SGR, GBM					static recrystalliz., BLG along shear bands, myrmek., Qtz SGR along high-strain zones	~20% hbl, ~10% qtz, obl qtz GSPO, minor feldspar recrystalliz overprinting static recrystallz.; amphib-facies protomylonite with upper GS-facies shear bands	3
H-37B	290084	3776991	leucogranite mylonite w/ hbl-rich layers	unclear	GBM	110	143.3	140.6	91.5	SGR, myrmek.	weakly-developed mylon fabric	4
H-37C	290084	3776991	amphibolite with NE-trending lin	top-NE	minor GBM					static?, myrmek, minor BLG	hbl aligned along subtle C' s.b.	4
H-38	289802	3776569	leucogranite mylonite/ultramylon	top-NE	GBM	60	134.4	143.7	74.3	SGR? recrystallized grains mixed with qtz & myrmek.	obl qtz GSPO	4
H-39	290314	3777223	leucogranite mylonite	top-NE	GBM+SGR	81	57.4	58.1	31.3	SGR, BLG, myrmek.	feldspar SGR dominant, C' s.b., obl qtz GSPO, incomplete qtz SGR overprint of GBM (some very large qtz grains)	3
H-40	293448	3774209	musc-chl mylonitic schist	top-NE	SGR+GBM	62	55.4	53.5	23.8		S-C-C' fabric, ~30% mica (mostly muscov, some chl+biot),mica fish, ~60% qtz, feldspar (?) porphyroclasts altered to cryptocrystalline grunge (not on matrix)	3
H-42	293610	3773948	quartzo-feldspathic ultramylonite	top-NE	SGR, GBM	84	44.4	43.1	14.7	SGR	pervasive feldpsar SGR, locally altered to cryptocrystalline grunge & f-grained sericite, ~10% biot+chl+white mica, qtz SGR is fairly pervasive, but locally some large quartz grains from GBM, obl qtz GSPO	3
Har-50a	270543	3769406	pegmatite protomylonite, cuts high-strain mylon fabric	unclear	GBM+SGR	119	131.7	133.9	44.5	SGR, myrmek.	feldspar SGR along porphyroclast margins	4
HV-32	278861	3765380	biotite granitoid mylonite	top-NE	GBM. SGR					SGR + BLG, myrmek	C' s.b. common, ~40% of biot is chloritized	3 or 4
HV-33	278866	3765459.2	high-strain felsic ultramylonite within platy bio-rich mylonite	top-NE	GBM, SGR	80	129.7	120.6	59.2	SGR	ob qtz GSPO, complete feldspar SGR, partial chloritization of biot	4
HV-34	278466	3765839.7	mylonitic milky quartz vein	top-NE	GBM	73	201.5	210.4	164.3	--	minor muscov defines macroscopic fol, ob qtz GSPO	4
HV-35	278473	3765818.1	granite ultramylonite	top-NE	GBM					SGR, myrmek	very little chloritization of biot, biot-lined C' s.b., pervasive feldspar rexstalliz - mixed with quartz	4
HV-36	278275	3766103.6	granitoid protomylonite, locally gneissic	top-NE	GBM, SGR	85	172.4	176.6	65	SGR+BLG	biot-lined C' s.b., ~25% of biot is chloritized, relatively minor feldspar rexstalliz.	4
HV-37	277321	3766777.4	quartz-rich portion of leucogranite mylonite	top-NE	GBM	115	209.3	210.2	129.3		minor biot with trace chl, obl qtz GSPO	4
HV-38B	277313	3766779.2	kyanite schist			221	141	131.3	71			4
HV-40	276636	3767985.3	mylonitic granitoid gneiss	top-NE	GBM, SGR	60	100.4	95.5	47.3	minor BLG	~15% biot (no chl), ~5% epi p.clasts, qtz SGR heterogeneously distribued (locally absent, locally dominant), obl qtz GSPO, very little feldspar rxstalliz (perhaps b/c abundant biot takes up much strain)	3
HV-41	276639	3767995.7	ultramylonitic granitoid gneiss	top-NE	GBM	56	104.1	104.9	37.3	SGR	~20% biot (minor chlo)+hbl, ~5% epi, pervasive feldspar SGR, sublte alignment of biot & hbl along C' bands	4
HV-41B	276639	3767995.7	gneiss/protomylonite	unclear	GBM					minor SGR	minor chloritiz of biot, epi common (associated with biot)	4
HV-43A	280228	3770867	mylonitic milky quartz vein	top-NE	SGR+GBM	64	94.7	88.9	40.9		obl qtz GSPO	3
HV-46	278535	3769679.6	leucogranite mylonite	top-NE	SGR+GBM	60	65.2	62.8	37.2	SGR+BLG	pervasive feldspar rxstalliz, well-defined obl qtz GSPO, C' s.b., biot+muscov - no chl	3
HV-48	279055	3770091.1	mylonitic milky quartz vein	top-NE	SGR, GBM	97	64.9	64.2	27.3		qtz SGR overprints GBM, qtz obl GSPI, some epi-rich layers	3
HV-49	279551	3770349.5	leucogranite mylonite	top-NE	SGR+GBM	118	93.6	97.4	34	SGR+BLG	obl qtz GSPO, pervasive feldspar rexstalliz, ~1% muscovite	3
HV-50/Har-81	279744	3770388.4	leucogranite mylonite	top-NE	SGR+GBM	85	82.1	83.9	37.6	SGR, BLG	obl qtz GSPO, pervasive feldspar rexstalliz, ~3% biot+muscov - no chl, some subtle C' s.b. (same location as Har-81)	3
HV-51	281222	3771206.2	leucogranite ultramylonite	top-NE	GBM+SGR	58	43.7	45.1	22.7	SGR	~90% feldspar rxstalliz., locally qtz GBM dominant with minor SGR, obl qtz GSPO, ~3-5% biot with no chl, qtz mixed with rxstallized feldspar	4
HV-52/Har-82	282456	3771404	layered protomylonitic gneiss	top-NE	GBM+SGR	71	76.4	80.7	31	BLG, myrmek	weakly-developed mylon fabric, ~5% hbl (concentrated in layers), subtle C' s.b., trace biot & no chl (same location as Har-82)	4
HV-53	283365	3772186.6	leucogranite mylonite	top-NE	GBM+SGR	60	67.6	65.5	28.5	SGR+BLG, myrmek	obl qtz GSPO, no chloritization of biot, locally qtz SGR is dominant, a few C' s.b.	4
HV-54	285169	3772593.6	layered leucogranite protomylonite	top-NE	GBM	97	217.4	215	121.9	myrmek, SGR	some C' s.b., ~50% of biot is chloritized, myrmek development very common along feldspar p.clasts	4

HV-56	287128	3772830.9	leucogranite ultramylonite	top-NE	SGR, GBM	58	51.9	52.5	23.7	SGR, BLG	obl qtz GSPO, some subtle C' s.b., pervasive feldspar rxstalliz, no chloritization of biot	3
HV-57	287903	3773098.8	mylonitic milky quartz vein	top-NE	GBM, SGR	108	62.4	63.4	36.6		some qtz SGR overprint of GBM, obl qtz GSPO, macroscopic fol defined by zones of aligned feldpsar (not recrystallized)	3
HV-60	287696	3773839.5	biotite granitoid mylonite/protomylonite	top-NE	SGR+GBM	79	66.3	65.8	38.7	BLG	biot-lined C' s.b. common, obl qtz GSPO, ~30% of biot is chloritized, locally qtz SGR is dominant	3
HV-62	287390	3774301.5	layered leucogranite mylonite	unclear	GBM, SGR	59	195.9	197.4	78.1	SGR, BLG	minor chloritiz of biot, qtz SGR locally not important	4
HV-67	286588	3775148.6	leucogranite mylonite	unclear	GBM	84	128.3	122.7	95.3	SGR	very long, single layer quartz grains present, little to no qtz SGR, feldspar myrmekite common, ~1% biot with trace chl	4
HV-69	286374	3774779.2	leucogranite mylonite	top-NE	GBM	92	131.8	138.5	101.9	SGR, myrmek	some very large qtz grains present, ~5% biot - no chl, some subtle biot-lined C' s.b.	4
HV-71	286383	3774572.7	massive leucogranite mylonite	top-NE	GBM					SGR, myrmek	biot-lined C' s.b., feldspar SGR grains are relatively large, ~5-7% biot with trace chl	4
HAR73	278467	3765840	leucogranite ultramylonite	unclear	GBM					SGR	~5% biot with no chl, pervasive feldspar rxstalliz., qtz does not form distinct continuous layers	4
HAR90, 90a	272480	3761864	biotite-rich mylonite with shallowly-dipping foliation (anomalous orientation compared to other steep shear zones here)	unclear	SGR, GBM					SGR+BLG?, chem breakdown	~15% biot with almost no chl, grungy feldspar, locally large irregular qtz grains lack SGR, anhedral titanite common (associated with epi), relatively large, fractured epi porphyroclasts common, no	3
HAR91	272339	3761907	10-20 cm thick mylonite zone	unclear	GBM, SGR					SGR, BLG, some myrmek	chloritization of biot, some subtle indicators of top-NE shear (obl qtz & feldspar) but overall poorly developed shear indicators	4
HAR92b	272298	3761918	muscovite-garnet schist with variable amounts of biotite								nonmylonitic, fresh coarse-grained biot+muscov; odd myrmek intergrowth btw biot & qtz (?) in one spot; garnet has inclusion of rounded biot, one small grain of kyanite noted	
HAR95	271971	3762001	quartz vein in amphibolite-rich gneiss								nonmylonitic, huge qtz grains with some GBM & SGR	
HAR96	271871	3762096	biotite augen gneiss (weakly mylonitic)	unclear	GBM+SGR					chemical breakdown, minor SGR?	~10% biot, ~50% of biot is chloritized, grungy feldspar is pervasively sericitized, discontinous qtz does not form clear layers	3
HAR97	272196	3764254	discrete mylonitic shear zone in gneiss	top-NE	GBM+SGR					SGR, BLG?	4-5 cm shear zone; shear bands abundant, obl qtz GSPO, rxstallized feldspar mixed with fine-grained biot, large epi/allanite porphyroclasts common, no chloritization of biot	4
HAR98	272123	3764740	mylonitic muscovite schist	top-NE	GBM+SGR						S-C-C' fabric, grungy feldspar - minor SGR+BLG?, locally pervasive small qtz subgrain development, other qtz-rich areas characterized by very large & irregular grains	3
HAR99	271976	3765905	mylonitic pegmatite	top-NE	GBM+SGR					SGR+BLG, fracturing	relatively large Fe-rich (green pleochroic) epi common, obl qtz GSPO, C' s.b. sigma-type clasts, partial chloritization of biot, muscov is commonly sheared	3
HAR101	271919	3766105	quartz vein, parallel to gneissic foliation		GBM, SGR	93	105.8	101.2	37.9		large feldspar along margin of vein is not recrystallized, epi veinlet along top margin, subtle obl qtz GSPO suggests dextral (orientation unclear), qtz SGR polygonization in some areas (but GBM is dominant)	3
HAR103	256633	3759523	mylonitic biotite-feldspar-rich gneiss	top-NE	BLG+SGR					cataclasis, fracturing, chem breakdown	qtz ribbons mostly lacking recrystallization, pervasive feldspar fracturing/crushing, evidence for mixed qtz slip, ~2% epidote, biot is not chloritized, C' s.b.	1
HAR103A	256633	3759523	mylonitic quartz vein		BLG+SGR							
HAR103B	256633	3759523	protomylonitic pegmatite		BLG+SGR	87	15.1	15.3	3.6	fracturing, local cataclasis & chemical breakdown	ribboned quartz grains mostly lacking recrystallization, evidence for qtz basal slip based on inferred CPO, local obl qtz GSPO & white mica-lined shear band (dextral)	1
HAR104	268690	3769217	mylonitic tank pass	top-SW?	SGR	87	71	71.8	24.8	BLG, fracturing	subtle indicators of dextral shear (e.g. shear bands, fractured feldspar porphyroclasts), pervasive fracturing of feldspar	2
HAR106	268419	3766125	thin quartz vein associated with pegmatite with NE-trending lineation	top-NE	GBM+SGR					minor BLG+SGR, fracturing	partial chloritization of biot, obl qtz GSPO	3
HAR110	274132	3770583	protomylonitic pegmatite	top-NE	GBM					SGR	some subtle C' s.b. & sigma-type clasts, minor chloritization of biot	4
HAR114	254628	3753807	strained leucogranite with NW-trending lineation		annealed					static		
HAR116	254664	3753861	muscovite schist (not mylonitic)		static/annealed						relatively coarse-grained muscovite lacking shear bands, static/annealed qtz rextalliz, minor GBM	
15-JB-03	274669	3775001	quartzite mylonite	top-NE	SGR+BLG	53	16.7	16.5	5.3	fracturing	spectacular S-C-C' fabric, qtz basal slip inferred to be common, muscovite is fine-grained & sheared, some ribboned qtz lacking recrystalliz, some feldspar porphyroclasts appear to be disaggretagated by fracturing	1
15-JB-15	274504	3774714	quartzite mylonite	top-NE	BLG	60	10.1	10	3.8		minor feldspar porphyroclasts are fractured, obl qtz GSPO, fol locally rotated along brittle-ductile shear bands, transposition of synkin qtz veinlets, very fine grained sheared white mica common	1
15-JB-25	275129	3774361	meta-arkose mylonite/cataclasite	top-NE	BLG						pervasive cataclastic overprint, brittle top-NE shears, some zones of qtz BLG, clasts showing SGR+BLG, very fine grained mica abundant - locally aligned // to fol	1

15-JB-26	275172	3774314	leucogranite mylonite	top-NE	GBM, SGR	55	77.9	79.6	37.6	SGR, GBM	abundant feldspar rxstalliz., locally qtz SGR not important, partial chloritization of biot, subtle obl qtz GSPO, sigma clasts	4
15-JB-27	275177	3774311	leucogranite mylonite with pseudotachylyte								pseudotachylyte & cataclastic overprint on predominantly amphibolite-facies mylonitic fabric	
15-JB-30	275322	3774145	leucogranite mylonite	top-NE	GBM, minor SGR	72	111.1	107.7	56.1	SGR, myrmek	obl qtz GSPO, subtle C' shear bands, partial chloritization of biot (~25%)	4
15-JB-53	277628	3771387	leucogranite mylonite	top-NE	GBM, minor SGR	58	69.5	74.82	44.1	SGR	C' s.b., abundant feldspar SGR, little to no chloritization of biot, some very large qtz grains unaffected by SGR	4
15-JB-86	288745	3770968	leucogranite mylonite	top-NE	SGR	56	51.3	49.1	21	SGR	obl qtz GSPO, C' s.b. with fine-grained chl, pervasive feldspar SGR, all mica is chlorite, ~10% epidote	3
15-JB-89	288657	3771072	leucogranite mylonite	top-NE	SGR+GBM	60	132.8	126.8	46.8	SGR	obl qtz GSPO, pervasive feldspar SGR, musc+biot with trace chl	3
15-JB-96	288727	3771714	leucogranite mylonite	top-NE	GBM, SGR	60	125	120.2	54	SGR, myrmek, BLG	qtz GBM dominant, locally SGR overprint, ~50% of biot is chloritized, some subtle C' s.b, relatively little feldspar rxstalliz.	4
15-JS-67	265165	3761922	granitoid mylonite zone	top-NE	SGR	52	47.7	45.7	20.2	BLG, fracturing	S-C-C' fabric, obl qtz GSPO, muscov + sheared chloritized biot	2
15-JS-70	265191	3762079	mylonitic quartz vein (low strain)	top-NE (?)	SGR, BLG	55	43.4	42.6	19.8		heterogenous recrystallization - SGR in some areas, other areas characterized by patchy extinction & relative large subgrains, sutured grain boundarys from BLG (very small bulges), subtle obl qtz GSPO (but fol is not well defined)	1 or 2
16-3-BW2	274647	3774589	biot-rich meta-arkose mylonite	top-NE	SGR, BLG	51	37.7	39.4	15.5	SGR?	obl qtz GSPO, C' s.b. in biot-rich areas, ~25% fine-grained biot, minor qtz BLG overprint of SGR, pure-qtz layers are very thin, epi common but no chlorite	1
16-3-BW3	274738	3774871	meta-arkose mylonite	unclear	SGR+BLG					fracturing	rounded detrital feldspar grains are brittely deformed, little evidence for rxstalliz, discountinuous qtz pods; biot, actinolite/hbl, epi all common; weak foliation development due to abundant rigid feldspar	1

* UTM locations given in NAD27 Datum

**categories for deformation conditions

1: mid- to lower GS facies microstructures

2: pervasive upper GS microstructures, little to no evidence of amphibolite-facies deformation

3: lower amphibolite facies to upper GS (transitional or evidence for upper GS overprint on amphibolilte-facies deformation)

4: amphibolite-facies fabric. little to no evidence for GS overprint

Little Buckskin samples — **Quartz grain size analyses**

Sample	UTM Easting (m)*	UTM Northing (m)	Sample description	Sense of shear	Qtz recrystalliz.	# grains	median diameter (μ)	geometric mean (μ)	stdev	Feldspar deformation	additional microstructures, comments	Def. conditions category**
LB-H-11	266015	3774600	leucogranite ultramylonite	top-NE	GBM	102	144	135	64	SGR	obl mica laths, pervasive feldspar SGR (no BLG or fracturing)	4
LB-11-113	266084	3775392	leucogranite mylonite	top-N	SGR + GBM	75	60	58	30	SGR	>80% feldspar recrystalliz., synkin biot (some chl) & titanite fish, subtle C' s.b.	3
LB-9-293	266654	3776937	leucogranite mylonite	unclear	GBM	61	250	272	185	SGR, minor fracturing, no BLG	qtz prism <a>, 1% mica (chloritized biot, minor muscov)	4
LB-11-171	267142	3777209	mylonitic quartz vein	top-NNE	GBM, SGR	249	76	73	48	--	inferred prism <a> dominant, some grains suggest basal slip	3
LB-11-173	267107	3777404	meta-arkose mylonite	app. top-NE	SGR	59	44	45	18.5	minor BLG, SGR?	~20% fine-grained biotite, qtz obl GSPO, biotite-lined C' s.b., 5-10% epi	2
LB-7-197	268302	3776275	leucogranite ultramylonite	top-NE	GBM	62	216	205	103	SGR, mnor kinking and fracturing, not BLG	prism <a> qtz slip, subtle qtz obl GSPO, abundant feldspar SGR	4
LB-7-154	267831	3777126	leucogranite ultramylonite	top-NE?	GBM	60	189	186	104	SGR	~4% biot (~50% chloritized), some very large qtz grains (1-layer wide grains), pervasive feldspar rexstallization	4
LB-7-126	267600	3777596	leucogranite mylonite	unclear	GBM	76	142	139	88	SGR, no BLG	abundant feldspar SGR, large prism <a> qtz grains, subtle qtz obl GSPO, ~2% biotite, trace muscovite	4
LB-7-190	268923	3775793	leucogranite mylonite	top-NE	GBM	61	281	256	150	SGR	S-C-C' fabric, abundant feldspar SGR, ~5% biot with some chl, no muscov., smeared out biot along C-planes	4
HAR108	270606	3777903	mylonitic tank pass	top-NE	GBM	73	200	200	64	SGR	obl qtz GSPO, pervasive feldspar rxstalliz, ~3% biot (~50% chloritized)	4
LB-11-3	272041	3776984	calc. quartzite mylonite	top-NE	SGR+BLG						~50% calcite, rounded detrital quartz & feldspar, quartz mixed with calcite, calcite obl GSPO	1
LB-10-231	271870	3777483	meta-arkose mylonite	app. top-NE	SGR	50	50	51	21		synkinematic epidote + chlorite, obl qtz GSPO, subtle C' s.b.	2
LB-10-232	272220	3777737	quartzite	app. top-NE	SGR, BLG	133	11	12	3		obl qtz GSPO, ~10% epi, <5% chl	1
LB-11-9	272583	3777778	meta-arkose	unoriented	SGR	59	34	33	13	BLG, chemical breakdown	obl qtz GSPO, grungy feldspar locally altered to epi & Fe-poor chl, ~5-10% epi, synkin chl+epi vein is buckled (cool!)	2
LB-7-106	272397	3778843	leucogranite mylonite	top-NE	GBM	69	212	223	106	SGR, myrkem, no BLG	>50% feldspar SGR, prism <a> qtz slip, subtle obl qtz GSPO, <4% biot, no muscov	4
LB-7-116	272672	3778505	leucogranite? ultramylonite	unclear	GBM	97	355	358	213	static recrystalliz, SGR	qtz prism <a> domimant, >70% feldpsar recrystalliz., <2% biot, no muscov.	4
LB-7-81	272268	3779625	leucogranite ultramylonite	top-NE	GBM					SGR	nearly complete SGR of feldsar, qtz obl GSPO, subtle C' s.b. with recrystallized muscov	4
LB-7-71	272716	3778930	leucogranite mylonite	top-NE	GBM	53	233	237	168	SGR (no BLG)	recrystallized quartz grains up to ~3 mm wide, subtle S-C fabric, <5% mica (biot, chloritized biot, trace muscov)	4
LB-7-69	272794	3778879	mylonitic quartz vein	top-NE	GBM	219	271	274	163	--	prism <a> slip dominant, trace mica & feldspar define fol, qtz obl GSPO	4
LB-7-77	272674	3779197	amphibolite	unclear								
LB-H-23	273171	3778877	hbl amphibolite	unclear	GBM					static recrystalliz.	weakly mylonitic; synkin hbl	4
LB-H-24	273239	3778979	hbl amphibolite									
LB-H-25	273354	3779049	mylonitic quartz vein	top-NE	SGR, GBM	204	44	44	27		SGR overprint on GBM, oblique quartz GSPO	3
LB-7-21	273665	3778681	leucogranite(?) ultramylonite	top-NE	GBM					SGR	oblique preferred orientation of biotite, qtz layers typically 1 grain wide, pervasive feldspar rxstalliz	4
LB-7-12	273034	3779791	leucogranite mylonite	unclear	GBM	54	287	276	133	SGR, minor BLG	<5% mica (biot with some muscov), abundant feldspar SGR but large porphyroclasts still present	4
LB-7-28	273632	3779232	mylonitic quartz vein	top-NE	GBM	268	183	187	109	--	irregular quartz grains >100 µm wide, obl GSPO	4
LB-H-26	273792	3779078	leucogranite mylonite	top-NE	GBM	81	196	197	106	SGR	S-C-C' fabric, pervasive feldspar SGR, ~3% biot, 5-10% muscov, mica fish	4
LB-7-3	274007	3779010	leucogranite mylonite	top-NE	GBM	95	155	156	114	SGR	S-C fabric visible at outcrop scale, ~3% biot, trace muscov.	4

* UTM locations given in NAD27 Datum

**categories for deformation conditions

1: mid- to lower GS facies microstructures

2: pervasive upper GS microstructures, little to no evidence of amphibolite-facies deformation

3: lower amphibolite facies to upper GS (transitional or evidence for upper GS overprint on amphibolilte-facies deformation)

4: amphibolite-facies fabric. little to no evidence for GS overprint

Buckskin - Rawhide samples

Sample	UTM Easting (m)*	UTM Northing (m)	Sample description	Sense of shear	Qtz recrystalliz.	Quartz grain size analyses: # grains	median diameter (µ)	geometric mean (µ)	stdev	Feldspar deformation	additional microstructures, comments	Def. conditions category**
3-231	764620	3783440	quartzo-feldspathic mylonite (meta-	top-NE	SGR, GBM					fracturing, BLG, SGR	obl qtz GSPO, C' s.b.	3
3-230	764686	3783496	meta-arkose mylonite	top-NE	SGR, GBM	59	61.2	56.4	25.3	BLG, SGR?	obl qtz GSPO, C' s.b. cleavage	3
3-214	773260	3782512	quartzo-feldspathic mylonite (granitic)	top-NE	SGR, minor BLG	70	16.3	15.8	5.9	fracturing & catacl., BLG, fl.perthite	obl qtz GSPO, C' s.b.	1
3-214a	773260	3782512	marble mylonite	top-NE							subtle S-C fabric, dark brown mica common, some calcite porphroclasts - postmylonitic replacement?	1
3-137	224357	3788294	cataclastic carbonate just below detachment	top-NE	--						beautiful S-C fabric (brittle-ductile?), some synkin chlorite defining S-C fabric in one area, grungy fine-grained calcite matrix	1
5-161	232780	3774982	layered bio-hbl quartzo-feldspathic mylonite	top-NE	SGR						obl qtz GSPO, local SC fabric, C' s.b.	2
5-190	231139	3776805	meta-arkose mylonite	top-NE	SGR	63	36.8	37.7	14	BLG, SGR, fracturing, myrmek.	obl qtz GSPO, C' s.b.	2
1-110	237161	3771422	aplite mylonite	top-NE	SGR	60	44.3	43.2	20.2		obl qtz GSPO, some qtz porphyroclasts	2
8-4	236366	3772317	calcareous meta-arkose mylonite	top-NE	GBM, SGR						obl qtz GSPO, C' s.b.	3
8-5	236400	3772355	quartzite (arenite)	top-NE	GBM, SGR	61	93	93.3	54.9		obl qtz GSPO, qtz grain pinning by mica, muscovite fish, qtz c-axis opening angle suggsts T ~400 C	3
1-52	229759	3779611	porphyritic granite mylonite	top-NE	SGR	75	42.7	38.6	25	fracturing, BLG	obl qtz GSPO, qtz ribbons, C' s.b.	2
3-143	775834	3789161	meta-arkose mylonite	top-NE	SGR+BLG	60	8.37	8.38	2.9	fracturing, minor BLG, SGR?	obl qtz GSPO, qtz ribbons, C' s.b.	1
2-34	232263	3784327	porphyritic granite mylonite	top-NE	SGR					fracturing & local catacl., BLG	obl qtz GSPO, C' s.b.	2
4-339	239547	3785134	porphyritic granite mylonite	top-NE	SGR+BLG					fracturing & catacl., BLG	obl qtz GSPO, C' s.b., qtz ribbons	1
9-257	238062	3787678	epi+cpx marble mylonite	top-NE	SGR						local obl calcite GSPO & SC fabric, finely-recrystallized calcite grain size, minor qtz-rich clasts show SGR+BLG	1 or 2
9-206	238826	3788528	granite mylonite w/ muscov.+garnet	top-NE	SGR	60	36.1	39.1	20.5	fracturing & catacl., BLG, fl.perthite	obl qtz GSPO, C' s.b., mica fish	2
4-188	239295	3789483	granite mylonite w/ muscov.+garnet	(YZ-cut)	SGR+GBM					pervasive SGR, minor BLG, myrmek.	NE-trending isoclinal fold, syn-folding biot.	4
4-175	238597	3790352	amphibolite gneiss (60% hbl, 40% plag)	none	(no quartz)					static recrystallization	NE-trending hbl lineation, granoblastic texture	
2-8	239394	3789562	hbl-rich qtz dioritic mylonitized gneiss	top-NE	SGR+GBM					fracturing, minor BLG	obl qtz GSPO, qtz ribbons, C' s.b., synmylon. hbl	2
1-91	239178	3789780	quartzo-feldspathic gneiss/mylonite	top-NE	SGR+GBM					fracturing, minor SGR & BLG	obl qtz GSPO, qtz ribbons, C' s.b.	2
4-636	239755	3789272	granite mylonite w/ muscov.+garnet	top-NE	SGR	61	56.5	56.6	24.4	fracturing & catacl., BLG, fl. perthite	obl qtz & BLG feldspar GSPO, C' s.b., mica fish	2
1-90	239168	3790129	quartzo-feldspathic gneiss, weakly mylonitic	top-NE	GBM+SGR					minor BLG, fracturing	obl qtz GSPO, minor qtz recrystalliz.., C' s.b.	3
10-161	254522	3783645	quartzite (silty arenite) mylonite	top-NE	SGR+BLG						obl qtz GSPO, C' s.b., synmylon. qtz veins, muscovite fish	1
1-122	260260	3790913	meta-arkose mylonite	top-NE	SGR					fracturing, BLG, SGR?	obl qtz GSPO	2
5-57	254416	3797210	meta-arkose mylonite	top-NE	SGR	61	34.5	34.8	12.9	BLG, SGR, fracturing, myrmek.	obl qtz GSPO, C' s.b., minor calcite layers with epidote	2
1-117	260080	3791941	porphyritic granite mylonite	top-NE	SGR+GBM					fracturing, SGR, BLG	obl qtz GSPO, C' s.b.	3
5-29	258611	3794024	meta-arkose mylonite	top-NE	SGR, GBM					BLG, SGR, fracturing, myrmek.	obl qtz GSPO	3
5-24	259073	3793973	porphyritic granite mylonite	top-NE	SGR, GBM					SGR, BLG, fracturing, myrmek.	obl qtz GSPO, C' s.b., local SC fabric	3
5-35	259180	3794588	porphyritic granite mylonite	top-NE	SGR					fracturing & local catacl., BLG	obl qtz GSPO, qtz ribbons dominant, C' s.b.,	2
12-BS-2	270858	3784030	meta-arkose (?) mylonite	dextral	SGR					fracturing	qtz zones are small, discontinuous; ~15% mica (mostly biot, locally chloritized), feldspar has undergone relatively little deformation, subtle shear bands	2
12-BS-3	269561	3783005	biotite granite mylonite	top-NE	SGR	60	50.7	48.1	18	BLG+SGR	C' s.b. and subtle obl qtz GSPO, ~15% biot with minor chl, pervasive feldpsar recrystallization	3
12-BS-5	257145	3778675	leucogranite mylonite	top-NE	SGR+GBM	134	79.5	79.8	24.2	SGR	pervasive feldpsar SGR and sericitization, most biot is chloritized, obl qtz GSPO	3
12-97	249224	3771726	leucogranite mylonite	top-NE	SGR, BLG	60	36.7	35.3	17.3	fracturing, minor BLG	incomplete qtz SGR - several large ribbons lacking recrystallization, no chloritization of biot, subtle C' s.b	1
12-131	244735	3770826	quartzofeldspathic granitic mylonite	top-NE	SGR, minor BLG	69	35.5	35.3	15.2	fracturing, BLG	C' s.b., incomplete qtz recrystallization, most biot not chloritized	2
12-142	239696	3768483	calcareous quartzite mylonite	top-NE	SGR+GBM					--	abundant tremolite, zones of pure quartz are rare, minor calcite, very subtle qtz obl GSPO	3
12-146	239642	3768342	marble mylonite	top-NE							obl calcite GSPO, relatively coarse-grained calcite, minor zones of qtz show GBM+local SGR	3

LR-4-2012	254557	3783637	calcareous quartzite mylonite	unclear	SGR+BLG						mostly recrystallized calcite, minor pods of qtz are partially recrystallized, tremolite & cpx p.clasts	1
H-1	270409	3786105	muscovite-bearing leucogranite (?)	top-NE	SGR, GBM	109	53.5	51.1	19.4	mostly undeformed, minor subgrain development	qtz locally mixed with feldspar, incomplete qtz SGR, ~15% muscov (throughgoing) - takes up much strain, <1% biot with minor chl, S-C' fabric, muscov fish	2
H-16	255530	3783297	amphibolite	top-NE								
H-17	255526	3783303	leucogranite mylonite	top-NE	GBM, SGR	168	55.6	57.2	37.5	SGR, myrmek	biot locally chloritized, subtle biot-lined C' s.b., very little feldspar fracturing, some very large qtz grains untouched by SGR	4
H-18	255483	3783339	leucogranite mylonite	top-NE	GBM+SGR	133	60.3	57.1	30.1	SGR	pervasive feldspar SGR, subtle qtz obl GSPO, biot-lined C' s.b., minor chloritization of biot, some large qtz grains lacking SGR	4
H-19	255523	3781732	granitoid mylonite	top-NE	GBM, SGR					SGR	pervasive feldspar SGR, recrystallized qtz mixed with feldspar, subtle obl biot & GSPO, ~13% biot (no chl), mix of feldspar & qtz probably inhibits GBM grain size	4
H-20	256666	3780698	leucogranite ultramylonite	top-NE	GBM, SGR	202	52.7	55.9	34.2	SGR	~3% biot - commonly chloritized, pervasive feldspar SGR, some large qtz grains lacking SGR oveprint	4
H-21	256741	3780690	amphibolite		GBM					SGR	not really mylonitic, ~25% hbl, ~5-10% biot - mostly chloritized, ~5% qtz pods with some GBM, ~50+% plag with some zones of SGR	
BP-179	240238	3772517	biotite gneiss	unclear	GBM, some SGR					minor subgrain development & SGR	gneissic fabric, ~12% bio, ~12% epi	4
BP-181A	240290	3772850	biotite gneiss protomylonite	top-NE	GBM, SGR	60	82.6	82	51.8	SGR+BLG, fracturing, chemical breakdown	fol // barite (+/- calcite) veins common, subtle obl qtz GSPO, some subtle C' s.b., ~50% of biot is chloritized, pervasive sericitization of feldspar, relatively minor feldpsar rxstalliz	3
BP-181B	240290	3772850	quartzite mylonite	top-NE	GBM, SGR						obl qtz GSPO, ~10% f-grained muscovite, qtz grains commonly	3
BP-187B	240337	3773120	biotite quartzo-feldspathic mylonite	top-NE	SGR+GBM	129	81	80	31	BLG & chemical breakdown/sericitiz, minor fracturing	C' s.b., ~10% mica (mostly biot with some chl), subtle qtz obl GSPO	3
BP-189	240335	3773137	marble mylonite								obl calcite GSPO, locally micaceous (colorless, low birefr white mica, low-Fe chl?), finely-recrystallized calcite	1
BP-190	240333	3773139	quartzite mylonite	top-NE	BLG, SGR	108	18.6	18.6	4.3		~7% white mica, C' s.b., qtz basal slip interpreted to be dominant	1
BP-192	240319	3773174	micaceous-calcareous phyllite mylonite	(unoriented)	minor BLG							1
BP-193	240322	3773187	marble mylonite	top-NE	minor subgrain development						~5% rounded/subgr qtz grains, subtle calcite obl GSPO	1
BP-194	240316	3773195	quartzite mylonite	top-NE	BLG	125	7.8	7.8	2.1		qtz ribbons with BLG along margins, ~5-10% white mica, C' s.b., mica fish, late kinematic veins (qtz, barite, calcite, chl)	1
BP-195	240325	3773202	quartzite/meta-arkose mylonite	(unoriented)	BLG						subtle qtz obl GSPO, ~5% white mica	1
BP-199	240240	3773228	marble mylonite	top-NE	minor qtz subgrains & BLG, fracturing						obl calcite GSPO, ~5% biot+muscov, ~5% qtz detritus	1
BP-201	240256	3773253	marble mylonite	top-NE							subtle obl fol defined by white mica (~3%, minor chl), rounded/subr barite (synmylon?)	1
BP-202	240286	3773276	marble mylonite	top-NE							subtle obl GSPO, up to 5% mica (biot & white mica), zones of qtz silt	1
BP-204A	240362	3773332	marble mylonite	top-NE							synkin calcite & barite veins, ~5% biot concentrated in layers (minor chl), obl calcite GSPO	1
BP-13-1	240239	3773236	calcareous quartzite mylonite	unclear	SGR						isoclinal micro folds with fol // axial traces are common, small recrystallized grain size for SGR	1
BP-13-4	240275	3773286	calcareous quartzite mylonite	unclear	BLG						cataclastic overprint of calc qtzite, very fine qtz grain size	1
BP-C2	240263	3773211	aplite mylonite	top-NE	BLG	160	6.7	6.7	2.1	fracturing, sweeping extinction, grain boundary sliding?, minor subgrain development; grain size analysis on quartz veinlet that cuts foliation at high angle	~7% mica (mostly muscov, minor chl & biot), obl qtz GSPO, synkin barite+quartz veins	1
7C2	238410	3772110	aplite mylonite	top-NE	SGR, BLG	52	29.6	29.6	10.3	minor SGR; grain boundary sliding?	~10% mica (mostly muscv, minor chl, biot), obl qtz GSPO, disaggregated & chloritized garnet (1), postmylonitic calcite veins	2

BK-8	226896	3793235	granodiorite protomylonite	top-NE	GBM, SGR	60	106.1	106.1	62	SGR, BLG	feldspar BLG primarily restricted to shear bands, biot almost completely chloritized, subtle obl qtz GSPO	3
BK-14	228358	3785605	leucogranite protomylonite mylonite	top-NE	SGR, BLG	58	23.3	25.2	15.5	fracturing, BLG	incomplete qtz SGR, complete chloritization of mica, subtle C' s.b.	1
BK-18	258817	3780490	leucogranite ultramylonite	top-NE	SGR, GBM	65	53.1	51.2	19.4	SGR, BLG	subtle C' s.b. & obl qtz GSPO, minor chl of biot	3
BK-19	259105	3780808	leucogranite mylonite	top-NE	GBM, SGR	84	85.8	92.6	62.9	SGR+BLG, some fracturing of p.clasts	some very large qtz grains lacking SGR, other areas are dominated by SGR, most biot is chloritized, subtle obl qtz GSPO	3
BK-20	259698	3781619	leucogranite ultramylonite	unclear	GBM	66	192	199.3	126.8	SGR, static recrystalliz?	minor chloritization of biot	4
BK-22	260056	3781258	leucogranite mylonite/protomylon	unclear	GBM	80	94.4	93.8	42.7	SGR+BLG, myrmek.	~5% hbl, partial chloritization of biot, subtle obl qtz GSPO,	4
BK-24	258455	3779373	granitoid mylonite	top-NE	SGR, GBM	57	41.2	42.3	24.4	SGR	~15% mica (biot with ~50% chloritiz), C' s.b., sericitiz of feldspar common, grungy recrystallized feldspar commonly mixed with quartz	3
AL-25	263034	3790138	marble mylonite	unclear							~10% tremolite, finely-recrystallized calcite	1
AL-26	263029	3790148	marble mylonite	top-NE	--						very fine-grained recrystallized calcite with subtle obl GSPO; unstrained round detrital quartz grains	1
AL-30	263159	3790076	granitoid mylonite	top-NE	SGR+ BLG	82	10.9	12.6	10.4	fracturing+BLG	~15% fine-grained biot, ~35% rounded rigid feldspar p.clasts, qtz obl GSPO	1
EM-1	254120	3783198	marble mylonite	top-NE							small epi/zoisite porphyroclasts common, some rounded qtz porphyroclasts with minor SGR, subtle calcite obl GSPO	1
EM-3	254125	3783217	calcareous metarkose mylonite	unclear	SGR, some BLG	101	24.6	24.2	7.3		some calcite C' s.b.	1
EM-4	254100	3783213	quartzite mylonite	top-NE	BLG+SGR	175	14.1	14.1	4.6		obl qtz GSPO	1
EM-5	254036	3783237	siliceous marble mylonite	top-NE							epi, cpx, and unstrained qtz porphyroclasts, only a few qtz-rich domains: show BLG+SGR with subtle obl GSPO	1
EM-6	254032	3783241	marble mylonite	top-NE							tremolite p.clasts common, obl alignment of tremolite	1
EM-DZ	254031	3783237	quartzite mylonite	unoriented	BLG+SGR	108	13.6	13.7	3.3		obl qtz GSPO, postmylonitic normal faults associated with calcite mineralization	1
EM-J-225	256324	3784209	marble mylonite	unclear								1
EM-J-232	253979	3784028	leucogranite mylonite	unclear	GBM, SGR					SGR	some large qtz grains comprising entire layer lack SGR, pervasive feldspar SGR, some chloritization of biot	4
EM-188	256009	3782634	marble mylonite	top-NE							brittle-ductile S-C fabric	1
EMJ-2-17	257145	3784578	leucogranite mylonite	top-NE	GBM, SGR	76	79.2	74.1	42.5	SGR, myrmek	some large qtz grains lacking SGR, minor chloritization of biot, C' s.b.	4
EM-2-37	256492	3783151	leucogranite mylonite	unclear	SGR, GBM	120	42.3	43.3	27.2	SGR, BLG	incomplete qtz SGR over GBM, minor chloritization of biot	3
EMJ-146	256467	3783922	marble mylonite	top-NE							obl calcite GSPO, very fine recrystallized calcite, clast of quartzite mylonite with SGR, BLG	1
EMJ-2-21	257445	3784530	leucogranite mylonite	top-NE	GBM	104	113	116.5	61.8	SGR	sublt obl qtz GSPO, pervasive feldpsar rxstalliz	4
EMJ-2-27	257287	3784382	mylonitic milky quartz vein	top-NE	GBM	166	211.1	217.4	130.6		clear obl qtz GSPO	4
EMJ-2-248	254159	3783190	leucogranite ultramylonite	top-NE	GBM+SGR	88	100.4	102.4	52.5	SGR	garnet common (locally disaggregated), feldpsar pervasively	3
14-5-178	272345	3784306	ugly crystalline (?) mylonite	top-NE	SGR+BLG	60	11.5	11.7	6.2	BLG, fracturing	obl qtz GSPO, epi & chl veins abundant	1
14-5-180	271850	3783565	granitoid (?) mylonite	(unoriented)	SGR, BLG	55	39.7	40.8	14.1	BLG, fracturing	5-10% epi, synkin chl, sericitization of feldspar, incomplete qtz BLG localized along grains	1
14-5-218	239026	3772439	quartzite mylonite	top-NE	SGR, BLG	60	18.4	18.3	7.1		obl qtz GSPO, muscovite fish, C' s.b.	1
14-5-221	239133	3772522	marble mylonite	top-NE	BLG						pods of qtz with very fine BLG, calcite (~200-400 um avg), some C' s.b. in qtz-rich zones	1
14-5-232	239346	3772634	marble mylonite	top-NE	BLG						minor qtz-chl-rich pods with BLG, ~100 um calcite grain size	1
14-5-274	771361	3781994	marble mylonite	top-NE							ultra-fine grained recrystallized calcite, fol-// stylolitic seems around micas, discrete top-NE offset of some postmylonitic calcite veins, locally c-grained calcite (late veins?) are brecciated, brittle-ductile marble mylonite	1
14-5-277A	226855	3793117	marble mylonite	unclear							unstrained qtz silt common, abundant graphite (?), syn- and	1
14-5-277B	226855	3793117	marble mylonite	top-NE							grungy marble with abundant qtz silt, some minor qtz-rich layers	1
14-5-283	248754	3780310	siliceous marble mylonite	top-NE	SGR+BLG						rounded detrital qtz grains within pure marble mylonite areas (with ultra fine-grained calcite), tremolite p.clasts, delta-type qtz p.clasts	1
14-5-288	248906	3780342	leucogranite mylonite	top-NE	GBM, SGR	60	50.1	47.7	26	SGR, BLG	abundant C' s.b., local qtz obl GSPO, no chloritization of biot, incomplete qtz SGR overprint of GBM	4
14-5-289	248864	3779709	marble mylonite	top-NE							locally obl GSPO in ultra fine-grained calcite, some stylolitic fol-// mica seams, synkin calcite veins	1

14-4-294	249142	3778970	leucogranite mylonite	top-SW	GBM	74	96.8	98.5	48.1	SGR	long qtz single-layer grains lacking SGR common, pervasive feldspar SGR, minor chloritization of biot, subtle obl qtz GSPO	4
14-5-298	249435	3779494	leucogranite mylonite	top-NE	GBM	78	90.8	85.7	59.4	SGR, myrmek.	very minor chloritization of biot, synkin titanite, C' s.b.	4
14-5-301	249446	3780707	marble mylonite	unclear							relatively clean marble with finely recrystallized mylonite	1
14-5-315	237948	2771734	marble								relatively coarse-grained marble	
14-5-317	237935	3771711	calc-silicate								tremolite marble	
15-JS-74	264984	3779444	quartzofeldspathic mylonite	top-NE	SGR, minor BLG	58	38.6	38.8	12.3	BLG, SGR?	~10% chl, trace non-chloritized biot,~5% epi, qtz well-mixed with feldspar in many places (qtz grain size estimate somewhat unreliable in this sample due to lack of pure qtz layers), qtz obl GSPO, C' s.b., locally some fol-// cataclasis	2
16-3-BP1	240282	3773252	micaceous quartzite	top-NE	SGR+BLG	130	13.8	14.1	4.2		S-C-C' fabric, incomplete quartz recystallization, ~25% muscovite, minor feldspar appears to have undergone subgrain development	1

* UTM locations given in NAD27 Datum
**categories for deformation conditions
1: mid- to lower GS facies microstructures
2: pervasive upper GS microstructures, little to no evidence of amphibolite-facies deformation
3: lower amphibolite facies to upper GS (transitional or evidence for upper GS overprint on amphibolilte-facies deformation)
4: amphibolite-facies fabric. little to no evidence for GS overprint

Swansea samples

Sample	UTM Easting (m)*	UTM Northing (m)	Sample description	Sense of shear	Qtz recrystalliz.	median qtz diameter (μ)	Feldspar deformation	additional microstructures, comments	Def. conditions category**
5-169	230296	3775048	Granodiorite	top-NE	SGR	~30-50	fracturing, BLG rextalliz.	obl. qtz GSPO: 27° (11-40°), σ- & δ-clasts, C' s.b. (15-30°), catacl., myrmek.	2
5-203	229512	3776811	Granodiorite	top-NE	SGR	32 ± 3	fracturing, BLG rextalliz.,	obl. qtz GSPO: 31° (14-42°), σ-clasts, C' s.b. (16-30°), myrmek.	2
5-174	231406	3775139	Granodiorite	top-NE	SGR	~20-40	fracturing, BLG rextalliz.	obl. qtz GSPO: 19° (7-25°), qtz ribbons, σ-clasts, C' s.b. (15-33°), catacl.,	2
5-155	232846	3774467	Quartz diorite	top-NE	SGR, GBM		fracturing, BLG rextalliz.,	local obl. qtz GSPO (subtle), qtz ribbons, σ-clasts, C' s.b. (16-38°), syn-kinematic	2
8-224	226966	3780859	Granite	top-NE	SGR	56 ± 10	fracturing, BLG rextalliz.	obl. qtz GSPO: 28° (13-36°), σ- & δ-clasts, C' s.b. (20-35°), myrmek., fl. Perthite	2
8-193	230652	3777843	Granite	top-NE	SGR, GBM	63 ± 10	fracturing, BLG rextalliz.,	obl. qtz GSPO: 18° (12-33°), σ- & δ-clasts, C' s.b. (14-30°), myrmek., fl. Perthite	2
1-51	229440	3779858	Granodiorite	top-NE	SGR, GBM	55 ± 9	fracturing, BLG rextalliz.	obl. qtz GSPO: 22° (10-34°), σ-clasts, C' s.b. (14-30°), myrmek.	2
9-1	232708	3776734	Granodiorite	top-NE	SGR	~30-55	fracturing, BLG rextalliz.	obl. qtz GSPO: 18° (14-28°), σ- & δ-clasts, C' s.b. (13-35°), myrmek., fl. Perthite	2
2-41	232737	3784401	Granite	top-NE	SGR	26 ± 2	fracturing, BLG rextalliz.	obl. qtz GSPO: 15° (9-26°), σ- & δ-clasts, C' s.b. (15-30°), catacl., myrmek., fl.	2
6-170	235121	3783226	Granite	top-NE	SGR	46 ± 7	fracturing, BLG rextalliz.	obl. qtz GSPO: 31° (11-35°), σ-clasts, C' s.b. (18-33°), catacl., myrmek., fl.	2
2-144	239160	3779399	Granite	top-NE	BLG II	~15-25	fracturing, BLG rextalliz.	obl. qtz GSPO: 20° (12-30°), σ-clasts, qtz ribbons, C' s.b. (17-28°), catacl.,	1
2-98	239009	3782534	Granite	top-NE	SGR , BLG	~12-20	fracturing, BLG rextalliz.	obl. qtz GSPO: 23° (9-33°), σ-clasts, C' s.b. (14-30°), catacl., fl. Perthite	1
2-90	239257	3782306	Granite	top-NE	SGR , minor	16 ± 1	fracturing, BLG rextalliz.	obl. qtz GSPO: 14° (7-28°), qtz ribbons, σ-clasts, catacl., myrmek., fl. Perthite	1
1-70	239138	3783840	Granodiorite	top-NE	SGR	47 ± 7	BLG rexstalliz., fracturing,	obl. qtz GSPO: 15° (8-35°), σ- & δ-clasts, C' s.b. (15-25°), myrmek., fl. Perthite	2
4-234	241433	3782661	Granodiorite	top-NE	SGR, GBM	~35-60	SGR rextalliz., BLG	C' s.b. (20-35°), σ-clasts, C' s.b. (15-25°), myrmek., fl. Perthite	3
2-152	239447	3784681	Granodiorite	top-NE	SGR	~30-55	BLG rextalliz., fracturing,	obl. qtz GSPO: 30° (10-38°), σ-clasts, C' s.b. (15-30°), myrmek.	2
6-262	241376	3783574	Granite	top-NE	SGR, minor	~15-30	fracturing, BLG rextalliz.	obl. qtz GSPO: 18° (10-30°), σ-clasts, C' s.b. (15-30°), catacl., myrmek., fl.	1
8-138	238588	3787279	Granite	top-NE	SGR	64 ± 8	fracturing, BLG rextalliz.,	obl. qtz GSPO: 25° (13-33°), σ- & δ-clasts, C' s.b. (20-30°), myrmek., fl. Perthite	2
4-464	243154	3784009	Granodiorite	top-NE	SGR, GBM	~35-55	fracturing, SGR rextalliz.,	σ-clasts, C' s.b. (13-25°), myrmek., fl. Perthite	2
9-35	240625	3788669	Granite	top-NE	SGR	~40-70	fracturing, BLG rextalliz.,	obl. qtz GSPO: 17° (9-30°), σ-clasts, myrmek., fl. Perthite	2
8-6	246035	3786154	Granodiorite	top-NE	SGR	~35-60	fracturing, BLG rextalliz.,	σ- & δ-clasts, myrmek., fl. perthite	2
5-7	247228	3787589	Granite	top-NE	SGR, minor	25 ± 2	fracturing, BLG rextalliz.	obl. qtz GSPO: 25° (8-33°), qtz ribbons, σ-clasts, C' s.b. (17-33°), myrmek., fl.	1
5-9	246989	3789220	Granite	top-NE	SGR	40 ± 4	BLG rextalliz., fracturing	obl. qtz GSPO: 19° (11-26°), C' s.b. (20-29°), myrmek., fl. Perthite	2
5-1	250001	3787797	Granodiorite	top-NE	SGR	32 ± 4	BLG rextalliz., fracturing,	obl. qtz GSPO: 22° (12-33°), σ-clasts, C' s.b. (20-30°), myrmek., fl. Perthite	2
2-127	251049	3789401	Granodiorite	top-NE	SGR	~20-35	BLG rextalliz., fracturing,	obl. qtz GSPO: 24° (13-35°), σ-clasts, C' s.b. (14-24°), myrmek., fl. Perthite	2
1-121	260283	3790949.6	Granodiorite	top-NE	SGR, GBM	~25-45	BLG rexstalliz., fracturing,	obl. qtz GSPO: 23° (9-33°), qtz ribbons, σ- & δ-clasts, C' s.b. (19-28°), myrmek.	2
1-119	259993	3791818	Granite	top-NE	SGR	48 ± 9	BLG rextalliz., fracturing,	obl. qtz GSPO: 16° (10-22°), σ- & δ-clasts, C' s.b. (19-28°), myrmek., fl. Perthite	2
5-27	258671	3793904	Granodiorite	top-NE	SGR+GBM	53 ± 8	SGR rextalliz., fracturing,	obl. qtz GSPO: 23° (13-29°), qtz ribbons, σ-clasts, C' s.b. (19-28°), myrmek., fl.	3
3-263	260406	3792182	Granite	top-NE	SGR, GBM	31 ± 4	BLG rextalliz. & fracturing,	obl. qtz GSPO: 26° (12-32°), qtz ribbons, σ-clasts, C' s.b. (13-26°), myrmek., fl.	2
5-46	258093	3795051	Granite	top-NE	SGR, GBM	43 ± 5	BLG rextalliz., fracturing,	obl. qtz GSPO: 14° (8-25°), σ- & δ-clasts, C' s.b. (15-25°), myrmek., fl. Perthite	2
5-16	260524	3793858	Granite	top-NE	SGR, minor	~20-37	fracturing, BLG rextalliz.	obl. qtz GSPO: 30° (11-34°), qtz ribbons, σ-clasts, C' s.b. (20-35°), catacl., kink	1
12-144	239691	3768399		top-NE	BLG, SGR	7.0 ± 1.8	fracturing, BLG, local SGR	beautiful S-C fabric, sheared biot, no chl	1
BP-189B	240335	3773137	ultramylonite	top-NE	SGR, GBM	77 ± 32	chemical breakdown, BLG	obl fine-grained mica (biot, chl, white mica), subtle qtz obl GSPO	2
BP-206	240237	3773221	ultramylonite	unoriente	BLG		chemical breakdown, BLG,	post-kinematic calcite+barite veins, most biot is chloritzed, white mica after	1
8-221	226346	3783173		coaxial	SGR, GBM		minor BLG, local SGR	~10% c-grained epi, minor chloritization of biot, symmetric conjug s.b. at relatively high angle to fol	2

rows 1-63 from Singleton & Mosher (2012)

* UTM locations given in NAD27 Datum
**categories for deformation conditions
1: mid- to lower GS facies microstructures
2: pervasive upper GS microstructures, little to no evidence of amphibolite-facies deformation
3: lower amphibolite facies to upper GS (transitional or evidence for upper GS overprint on amphibolilte-facies deformation)
4: amphibolite-facies fabric. little to no evidence for GS overprint